Chinese Chemical Letters 37 (2026) 111387

Contents lists available at ScienceDirect

Chinese Chemical Letters

journal homepage: www.elsevier.com/locate/cclet

Recent advances in solid-state zinc-air and zinc-ion batteries

Ya Han[a,b,1], Kejun Jin[a,1], Tingyu Zhao[a,1], Yingjian Yu[a,*]

[a] College of Physics Science and Technology, Kunming University, Kunming 650214, China
[b] College of Chemistry and Chemical Engineering, Kunming University, Kunming 650214, China

ARTICLE INFO

Article history:
Received 11 March 2025
Revised 20 May 2025
Accepted 28 May 2025
Available online 10 June 2025

Keywords:
Solid-state
Zinc-air batteries
Zinc-ion batteries
Bifunctional catalysts
Electrolytes

ABSTRACT

Solid-state zinc-air batteries (SZABs) and solid-state zinc-ion batteries (SZIBs) exhibit significant potential for applications in flexible electronic devices, due to zinc's abundance, enhanced safety, high theoretical energy density, and eco-friendliness. Recently, various SZABs and SZIBs utilizing advanced solid-state electrolytes (SEs) and cathodes have been developed. However, the conductivity of the cathode, as well as the construction of active sites and ion transport pathways during charging and discharging, require further investigation. Additionally, the electrolyte plays a critical role in solid-state batteries, directly impacting the output performance of the battery, cycling stability, and operational lifespan. Thus, the development of high-quality electrolytes alongside efficient and stable electrodes is essential for the large-scale application of solid-state batteries. This review examines the working principles and assembly processes of SZABs and SZIBs and summarizes the superior properties of various cathodes and electrolytes, thereby offering new perspectives for advancing high-performance SZABs and SZIBs.

© 2026 Published by Elsevier B.V. on behalf of Chinese Chemical Society and Institute of Materia Medica, Chinese Academy of Medical Sciences.

1. Introduction

Batteries are indispensable technologies for energy storage and conversion, which are crucial for powering electronic devices [1,2]. In addition, the surging demand for flexible wearable electronics such as foldable smartphones, smart medical devices, smart clothing, and sensors is driving the demand for batteries that can meet the demands of everyday life [3,4]. These flexible wearable electronics require batteries with characteristics such as excellent energy density, long life, lightweight, flexibility and safety [5,6]. Additionally, these devices usually require batteries that can be powered for a long time and can maintain stable performance under extreme conditions such as bending and folding. Over the past few decades, a variety of battery types have been developed, including metal-ion cells, metal-air batteries, and fuel cells, with lithium-ion batteries (LIBs) emerging as the dominant choice [7]. However, existing LIBs and other traditional battery technologies have struggled to meet the needs of these emerging applications. Despite their superior performance, LIBs are approaching their theoretical capacity limit. Additionally, as the primary power source in modern applications, LIBs face challenges such as limited Li resources, high cost, and safety concerns [8–10]. In addition, the electrode material may suffer mechanical damage during repeated bending, affecting battery performance. All these problems limit their practical application in flexible wearable devices. Therefore, the development of compatible power supply devices that can provide high energy density, compact structure, marvelous flexibility and safety has become the focus of current research.

Among the next-generation batteries, solid-state zinc-air batteries (SZABs) and solid-state zinc-ion batteries (SZIBs) exhibit outstanding characteristics, including high abundance, low cost, a theoretical energy density of 1086 Wh/kg, a theoretical capacity of 820 mAh/g, environmental friendliness, ease of manufacturing, and enhanced safety [11–16]. SZABs use solid electrolytes to replace traditional liquid electrolytes, which enhances the flexibility of the cell, making it one of the ideal choices for flexible wearable devices. In addition, SZIBs uses zinc ions as carriers between the positive and negative electrodes, which has a long cycle life and is suitable for devices requiring frequent charging, and is expected to achieve large-scale commercial applications in the future. These batteries are poised for widespread used in modern life (such as sensors and smart devices) and medical applications (including pulse detection and pacemakers) (Fig. 1). The development of zinc-ion batteries (ZIBs) and zinc-air batteries (ZABs) can be categorized into four distinct stages: inception, rise, stagnation, and revival (Fig. 2). In 1878, French engineer L. Maiché introduced the first ZAB by enhancing the cathode of the Leclanché battery [17]. This innovation paved the way for a series of new ZABs, capable of meeting diverse application needs for nearly a century. However, in the 1990s, research on ZABs experienced a downturn due

* Corresponding author.
E-mail address: yuyingjiankmu@163.com (Y. Yu).
[1] These authors contributed equally to this work.

https://doi.org/10.1016/j.cclet.2025.111387
1001-8417/© 2026 Published by Elsevier B.V. on behalf of Chinese Chemical Society and Institute of Materia Medica, Chinese Academy of Medical Sciences.

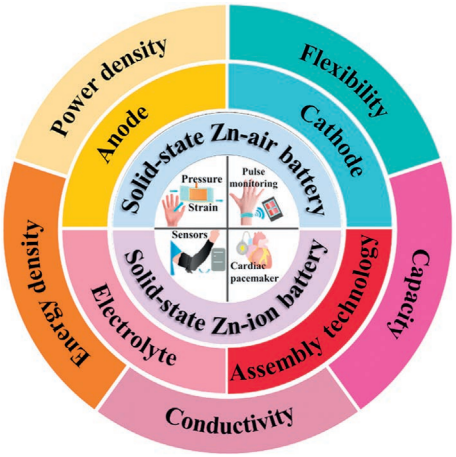


Fig. 1. Description of SZABs and SZIBs, including applications, main structure, and key parameters.

to the rapid advancements in LIB technology [18]. Despite its current dominance in the market, challenges such as limited capacity and safety concerns of LIBs have become increasingly evident. In response to the ever-increasing demand for energy storage, flexible solid-state Zn-ion batteries (FSZIBs) and flexible solid-state Zn-air batteries (FSZABs) were proposed in 2014 and 2017, respectively [19,20]. Rechargeable SZABs and SZIBs are garnering significant attention and are viewed as competitive and promising energy storage solutions. Recently, these two solid-state battery types are advancing toward higher practical energy densities and capacities, while maintaining performance across a full temperature range [21,22].

Numerous reviews have focused on SZABs and SZIBs. Lei *et al.* proposed biocompatible Zn-based batteries (ZBs) from the perspective of battery-induced injury and related safety issues, offering insights into recent developments in various wearable and implantable battery systems and suggesting potential directions for future research [23]. Li *et al.* offered a comprehensive overview of the engineering, design, and characterization of FSZABs, thereby summarizing advancements in their electrochemical performance and mechanical flexibility for wearable electronic devices [24]. Furthermore, researchers have explored design concepts and recent progress in both SZABs and SZIBs [25–31]. However, the continuous development of SZABs and SZIBs necessitates a real-time summary of findings, thereby accelerating advancements in these emerging energy storage technologies. Additionally, discussing SZABs and SZIBs together can facilitate a shared exploration of investigation strategies for solid-state ZBs (SZBs). This paper systematically reviews the latest research affecting the energy density, flexibility, and conductivity of SZABs and SZIBs, thereby examining aspects of the cathode, electrolyte, and assembly processes (Fig. 1). First, this review introduces the configuration and reaction mechanisms of SZABs, classifies recent catalysts and electrolytes, and summarizes the development status and challenges of these materials, particularly under extreme environments. Second, the structure and working principle of SZIBs are introduced, and the development status of SZIBs is summarized in detail from aspects across cathode, electrolyte, and interface. Finally, the primary challenges faced by SZABs and SZIBs are summarized and prospects for new designs are proposed.

2. Solid-state Zn-air batteries

2.1. Configurations and working mechanism

The configuration of SZABs and SZIBs was divided into planar and cable structures (Figs. 3a and b). Planar structure (sandwich and coplanar types) is widely utilized because of their simple manufacturing process. The cable structure exhibits compatibility with the textile industry, breathability, and superior flexibility. However, they are difficult to manufacture and tend to result in high-internal resistance [15]. As shown in Fig. 3c, a typical SZAB is a semi-open system configuration consisting of an air cathode with a Zn anode, a bifunctional catalyst, and a solid alkaline electrolyte, which offers advantages in both electrochemical and mechanical properties. This battery relies on the electrochemical reaction between Zn metal and O_2 as follow [32–34]:

$$\text{Zn anode: } Zn + 4OH^- \leftrightarrow [Zn(OH)_4]^{2-} + 2e^- \quad (1)$$

$$\text{Air cathode: } O_2 + 4e^- + 2H_2O \leftrightarrow 4OH^- \quad (2)$$

$$[Zn(OH)_4]^{2-} \leftrightarrow ZnO + 2OH^- + 2H_2O \quad (3)$$

$$\text{Overall: } 2Zn + O_2 \leftrightarrow 2ZnO \quad (4)$$

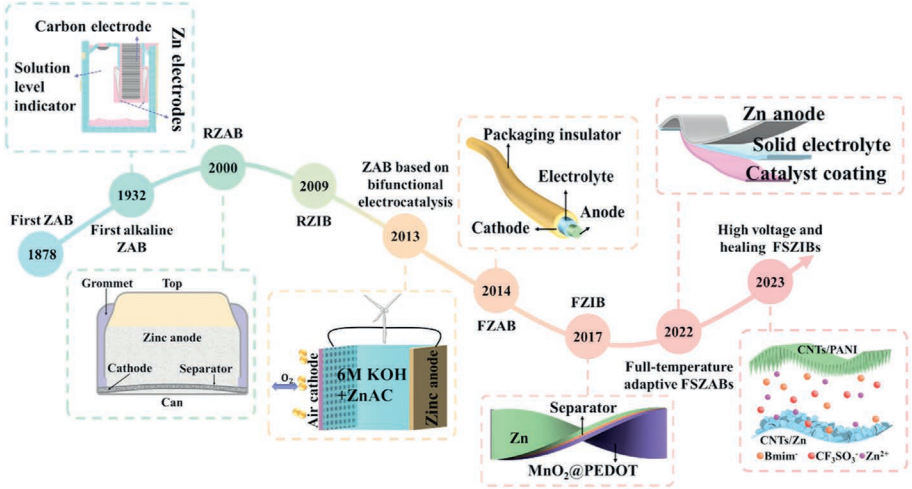


Fig. 2. Schematic illustration of the history of ZABs and ZIBs.

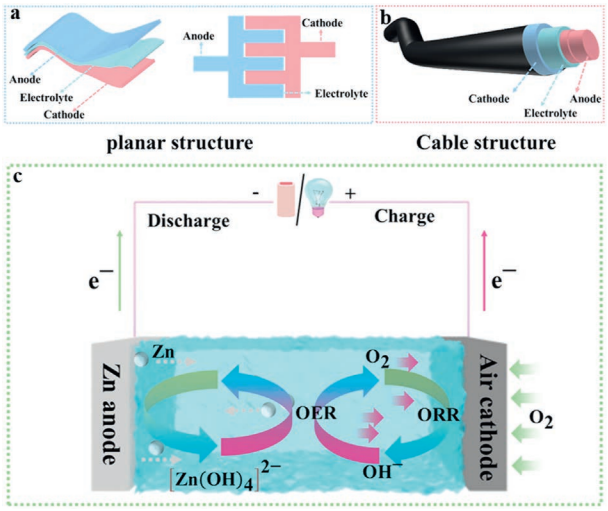


Fig. 3. (a, b) Structure illustrations of SZABs and SZIBs. (c) Schematic operation principle for SZABs.

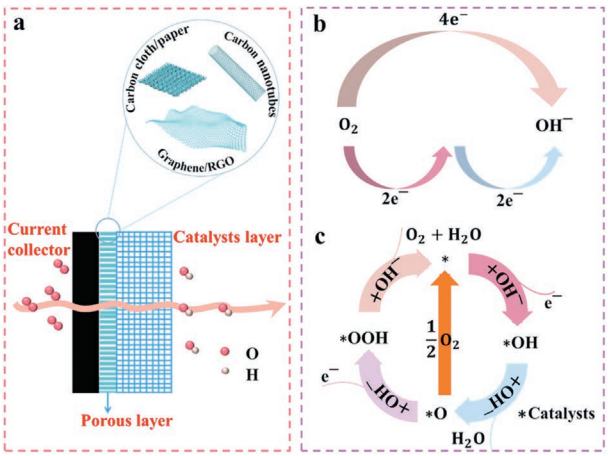


Fig. 4. (a) Diagram of cathode structure based on carbon materials. (b) ORR process and (c) OER process in ZABs.

2.2. Design of the air cathode

The air cathode is the most significant component in the SZABs. The oxygen reduction reaction (ORR) and oxygen evolution reaction (OER) enhanced ZABs with higher-energy density during discharging and charging. In 2013, Dai *et al.* prepared a bifunctional catalyst for ZABs. Since, there has been extensive research on cathode catalysts [35]. Structurally, the cathode of a SZAB consists of a current collector, a porous layer, and a catalyst layer (Fig. 4a). These three parts act the roles of charge transfer, O transfer, and reducing reaction energy barrier, respectively. Functionally, the ORR of the discharge process determined the specific capacity, discharge capacity, and power density of ZABs [36]. Two primary ORR pathways depend on the adsorption of O_2 using an electrocatalyst (Fig. 4b): One is the direct four-electron transfer to generate OH^-, the other is two-electron transfer, which exhibits a high-reaction potential, and the resulting HO_2^- is corrosive, thereby resulting in a reduced in the electrocatalytic activity of ZABs. Thus, it is crucial to prevent two-electron transfer to achieve more direct four-electron transfer [37]. The OER during charging decides the cycle capacity and charging efficiency of the battery [25]. Intermediates such as M-O and M-OH are essential for the OER, which is dependent on the electrocatalyst. Sequentially, M-OH and M-O are produced through the combination of OH^- and electrocatalyst (M). Subsequently, there are two different routes for the formation of O_2 (Fig. 4c). One is the direct production of O_2 from M-O, and the other is the reaction of OH- with M-O to form M-OOH, which then decomposes to O_2. For active OER electrocatalysts, the best M-O bond strength is critical to their electrocatalytic performance, while too strong or too poor M-O bonds can lead to weak catalytic activity [38,39]. The cathode consisting of qualified SZABs exhibits the following characteristics: (1) Outstanding conductivity for driving charge transfer; (2) Appropriate pore size to ensure superior O_2 diffusion; (3) Efficient bifunctional catalytic efficiency; (4) Appropriate hydrophobicity and hydrophilicity for the provision of a stable three-phase interface.

Given the above factors and overall flexibility, carbon-based materials such as graphene, carbon nanotubes (CNTs), carbon cloth (CC), and carbon paper have been extensively utilized as cathode materials for ZABs (Fig. 4a inset). This porous cathode exhibits a wide range of raw material sources, lightweight, hydrophobicity, and tunable surface affinity, thereby satisfying the requirements of FSZABs well [40–43]. A review of the past development of carbon-based catalysts for SZABs positive electrodes shows that these materials are divided into the following three major types based on metal atom types in the constituent structure: (1) Metal-free carbon-based electrocatalysts; (2) Single-atom transition metals, and their compounds for carbon-based electrocatalysts; (3) Multiatomic transition metals and their compounds for carbon-based electrocatalysts.

2.2.1. Metal-free carbon-based electrocatalysts

The electrocatalytic process occurred on the surface of the electrocatalyst, which was carefully and rationally designed and modulated. Despite precious metal catalysts based on Pt materials exhibiting advanced ORR properties, their poor economic viability and instability limit their wide application. Recently, carbon-based metal-free catalysts consisting primarily of nanostructured carbon polymers with different sizes have been widely utilized as cathode catalytic materials for SZABs due to their outstanding stability, large pore size, excellent specific surface area, fantastic degradability, and excellent electrical conductivity. Nevertheless, pure carbon materials lack enough active sites and therefore face the issue of poor catalytic efficiency. Hence, rational modification of carbon materials is necessary to enhance the ORR. Presently, the selection of carbon substrates for metal-free carbon-based catalysts primarily focuses on metal-organic framework (MOF), covalent organic framework (COF), and electrospun carbon nanofibers (ECNFs). Furthermore, upon combining fluorine (F), phosphorus (P), nitrogen (N), boron (B), and sulfur (S) with carbon-based materials to adjust the charge distribution of neighboring carbon atoms, heteroatom single-doped carbon catalyst and heteroatom co-doped carbon catalyst were obtained. Hu *et al.* prepared N/P co-doped metal-free carbon material (NPPC-950) through high-temperature calcination using zeolitic imidazolate framework-8 (ZIF-8) as a precursor and red P as a P source. The preparation process is shown in Fig. 5a [44]. Scanning electron microscope (SEM) image (Fig. 5b) indicated that NPPC-950 exhibited an irregular rod-like structure, cross-linked with each other, and the particle sizes are in the range of 200–300 nm. Transmission electron microscope (TEM) and high-resolution TEM (HR-TEM) images (Figs. 5c and d) showed that NPPC-950 exhibited a uniform woven amorphous carbon structure. To demonstrate the performance of wearable electronic devices, an FSZAB was assembled using NPPC-950 as the air cathode material, Zn, and polyvinyl alcohol (PVA) as the negative electrode material and electrolyte (Fig. 5e). It was observed that the open-circuit voltage (OCV) of the prepared FSZABs reached 1.46 V and its power density was 50.1 mW/cm^2 (Fig. 5f). The NPPC-950-based FSZAB demonstrated a stable voltage plateau in constant-current discharge tests at current densities from 2 mA/cm^2 to 15 mA/cm^2,

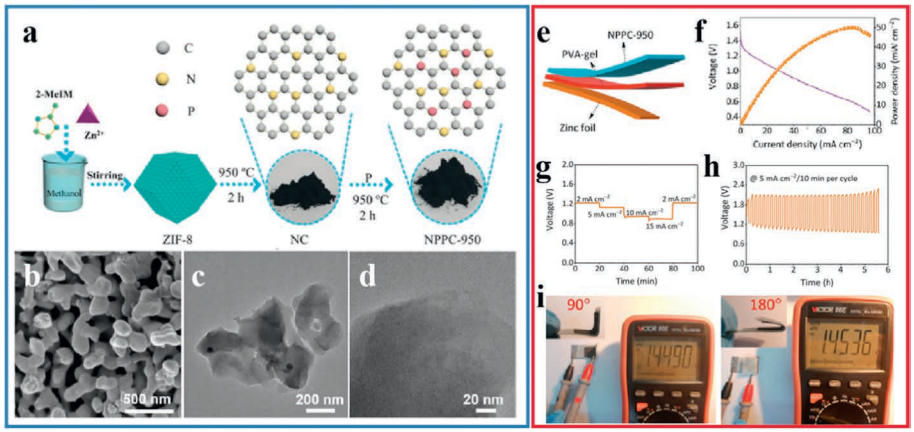


Fig. 5. (a) Schematic illustration of NPPC-950 synthesis. (b) SEM image, (c) TEM image, and (d) HR-TEM image of NPPC-950. (e) Configuration of the FSZAB. (f) Discharge polarization curves and power density diagrams of NPPC-950-based FSZAB. (g) Voltage platform of NPPC-950-based FSZAB at different discharge current densities. (h) Charge–discharge curves of NPPC-950-based FSZAB at 5 mA/cm^2. (i) OCV at different bending angles. Copied with permission [44]. Copyright 2022, Elsevier Inc.

Table 1
Properties of metal-free carbon-based electrocatalysts.

Catalyst	Electrolyte	Structure	OCV (V)	Peak power density (mW/cm^2)	Cycling (h/cycle)	Ref.
N,P-C-1000	PANa	Sandwich	1.423	85.5	>120 h at 10 mA/cm^2	[47]
F-ACET-500	PVA	Sandwich	1.10	52	>180 h at 2 mA/cm^2	[48]
B&N-Gr-900	PVA	Sandwich	1.6	34	200 cycles at 2 mA/cm^2	[49]
NOC–1000–1	Cellulose-GPEs	Sandwich	1.48	100.92	>30 h at 1 mA/cm^2	[50]
MN7–10/3	GPEs	Sandwich	1.4	109.3	–	[51]
FANC-12	PAA	Sandwich	–	174.1	>150 h at 5 mA/cm^2	[52]
FNCF	GPEs	Sandwich	1.49	160	>1200 h at 10 mA/cm^2	[53]

ACET: acetylene black; Gr: graphite; FANC: furfuryl alcohol-derived O, N-codoped nanoporous carbon; FNCF: freestanding nitrogen-doped carbon film; PAA: polyacrylic acid.

thereby indicating its excellent rate performance (Fig. 5g). The charge/discharge test in Fig. 5h indicated that it was stably and continuously cycled for over 5 h. Finally, the FSZAB was subjected to various degrees of bending tests (Fig. 5i), which indicated that the OCV of this solid-state battery remained stable under different bending conditions. In summary, the remarkable performance of FZABs is mainly due to the fact that doping P element in the metal-free carbon-based catalyst can improve the specific surface area of the material, regulate the electronic structure in the carbon matrix, and reduce the work function of the catalyst, thereby enhancing the ORR activity.

Given the strong ability of porphyrins to coordinate metal cations into complexes, porphyrin covalent organic framework (POF) was considered an ideal strategy for the preparation of bifocal oxygen electrocatalysis. For example, Zhang *et al.* prepared CNF@POF catalyst by coating POF on carbon nanotubes, and made full use of the activity of the cobalt-coordinated porphyrin active site to make CNF@POF catalyst show a high hydrophilic surface, which solved the problem of low affinity between small porphyrin molecules and conductive scaffolds [45]. In addition, FZABs assembled in CNF@POF had a high OCV of 1.39 V and a red light-emitting diode (LED) that continuously lighted up at varying degrees of bending. Additionally, compared with other carbon nanomaterials, ECNFs not only exhibited advantages of controllable morphology, high porosity, and simple preparation process but also exhibited excellent flexibility. Thus, it is widely utilized in electrocatalytic materials. To solve the problem of high cost and complex synthesis process of traditional three-atom doped catalysts, Shi *et al.* developed an efficient, low cost, and environmentally friendly ternary heterogeneous atom-doped carbon, F, B, and N tri-doped lignin-based carbon nanofibers (BNFLCFs), which served as bifunctional ORR/OER electrocatalysts [46]. Specific synergies between B, N and F heteroatoms could change the original electronic structure of adjacent carbon atoms, optimize the adsorption/desorption energy of oxygen, and generate more pores and surface areas to facilitate the exposure of additional active sites and promote the transfer of intermediates and reactants. In addition, B, N, F triple doping C could increase the nitrogen defect level of the carbon matrix and form abundant active sites. SZABs assembled with BNFLCFs catalyst and PVA electrolyte not only successfully lit the LED, but also did not significantly change the charge and discharge voltage during the repeated folding process. It also resulted in more pores and surface area, thereby facilitating the exposure of additional active sites and leading to satisfactory catalytic activity. Table 1 summarizes the property of recent metal-free carbon-based electrocatalytic SZABs in terms of voltage, power density, energy efficiency, and flexible applications [47–53]. It was observed that these materials primarily involved some nano- and small-molecule polymers, as well as surface defects of carbon materials, such as impurity defects, vacancy defects, and interstitial defects. They were designed to positively affect the bifunctional catalysis of SZABs.

In summary, the combination of F, P, N, B and S heteroatoms with carbon substrate materials such as MOF and ECNFs is the main method to solve the problem of high cost of precious metal materials such as Pt and improve the ORR performance of metal-free carbon-based catalysts. However, the effect of heteroatom covalent bonds in carbon matrix on catalyst properties still needs further study.

2.2.2. Single-atom transition metals and their compounds for carbon-based electrocatalysts

Currently, carbon-loaded transition metal catalysts are among the most studied multifunctional electrocatalysts due to their excellent tunable catalytic properties. Transition metal hybrid materials and their derivatives cover a wide range of electrocatalysts and are a focus area for air cathodes of SZABs. The intrinsic activity of electrocatalysts and the dispersion of the active sites are two key factors for enhancing the catalytic activity of electrocatalysts.

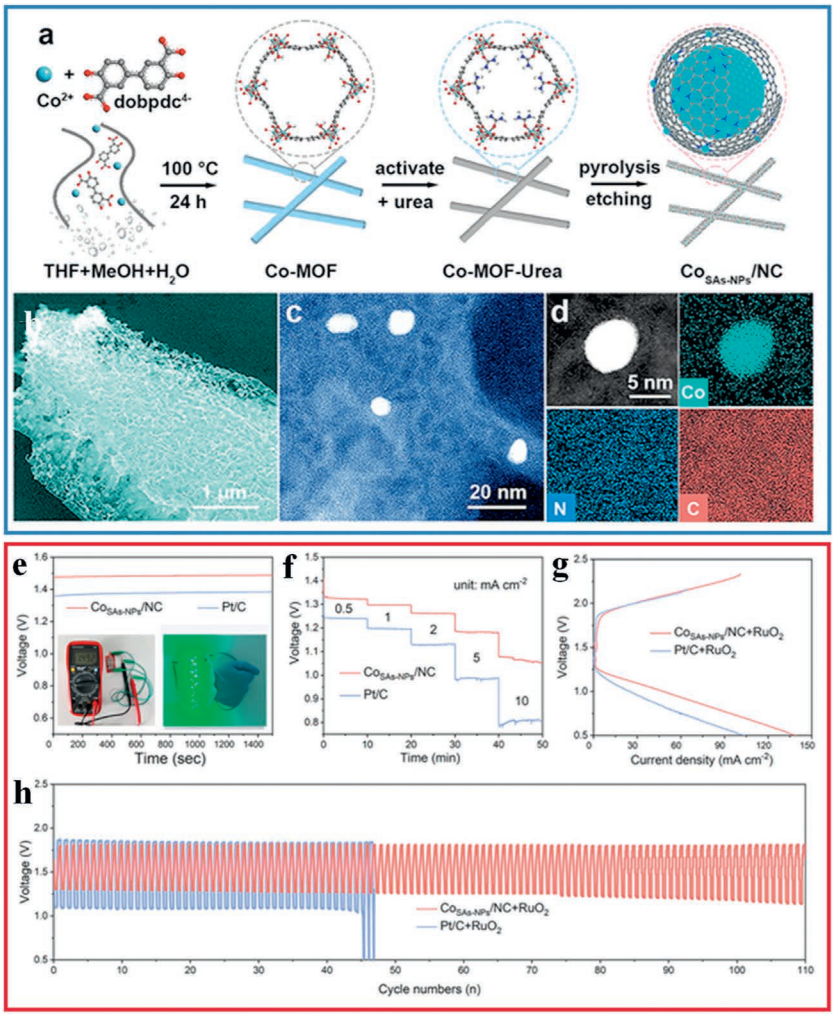


Fig. 6. (a) Schematic illustration of $Co_{SAs\text{-}NPs}$/NC synthesis. (b) SEM image, (c) high-angle annular dark-field scanning transmission electron microscopy (HAADF-STEM) image, (d) high-resolution HAADF-STEM-energy-dispersive X-ray spectroscopy (EDS-STEM) mappings of $Co_{SAs\text{-}NPs}$/NC. (e) Open-circuit plots of SZABs. (f) Discharge curves of SZABs at various current densities. (g) Charge–discharge polarization curves of SZABs. (h) Galvanostatic cycling stability of the SZABs at 1 mA/cm^2. Copied with permission [64]. Copyright 2024, Elsevier B.V.

Therefore, increasing the intrinsic activity of each active site and enhancing the number of active sites are two basic principles for designing superior performance electrocatalysts [54–62]. To obtain high intrinsic activity, electronic modulation and N doping of metal nanoparticles (NPs) are commonly used strategies. Active sites were morphologically modulated by the size, distribution, and loading of metal NPs. Furthermore, a combination of doped carbon with metal NPs enhanced M-X-C ((M: cobalt (Co), iron (Fe), tungsten (W); X: N, boron (B), phosphorus (P)) materials, thereby exhibiting excellent ORR and OER bifunctional electrocatalytic capabilities. In 2011, Zhang *et al.* presented a highly active single-atom catalyst ($Pt1/FeO_x$) with outstanding stability for CO oxidation, which initiated the study of single-atom catalysis [63]. The single-atom catalysts (SACs), with the benefitsof high activity, ultra-high atom utilization (~100%), and excellent stability, exhibited significant potential in OER, ORR, ZABs, and other fields. Additionally, doping single or mixed heteroatoms, such as N, sulfur (S), B, P, and fluorine (F), can modulate the electronic structure of carbon through polarizing neighboring C atoms with different electronegativities, introducing defective sites, increasing the conductivity, and enhancing the catalytic activity. Generally, metal-N_x groups are configured as active sites in metal-doped carbon electrocatalysts. Yang *et al.* designed and synthesized an interesting $Co_{SAs\text{-}NPs}$/NC catalyst based on the MOF synthesis route consisting of small Co-NPs encapsulated in several layers of graphite nanopores modified by Co-Sas (Fig. 6a) [64]. This material exhibited a three-dimensional (3D) porous carbon structure through SEM images (Fig. 6b). A 3D porous morphology with abundant pore structure was observed in aberration-corrected transmission electron microscopy (AC-STEM) images (Fig. 6c), thereby facilitating the mass transfer within the ORR process. Moreover, the presence of small-sized Co-NPs was observed in the carbon matrix. It was also observed that the elemental mapping of the C energy dispersion spectrum and N signals were evenly dispersed. Thus, Co signals clustered at the particle interface. The Co-N signals correlated with each other, indicating the coexistence of Co-SAs and Co-NPs in $Co_{SAs\text{-}NPs}$/NC (Fig. 6d). Tests on assembled SZABs indicated that the solid-state $Co_{SAs\text{-}NPs}$/NC@ZAB exhibited a stable and fantastic OCV of 1.492 V and a superior rate performance during trapezoidal discharging at various current densities of 0.5–10 mA/cm^2 (Figs. 6e and f). This offered a significant potential for practical applications. The charge/discharge potential difference of $Co_{SAs\text{-}NPs}$/NC+RuO_2@ZAB was lower compared with those of Pt/C+RuO_2@ZAB at 1 mA/cm^2 (Fig. 6g), which indicated that $Co_{SAs\text{-}NPs}$/NC exhibited stronger ORR activity. Given the flexibility test, the solid-state $Co_{SAs\text{-}NPs}$/NC+RuO_2@ZABs also demonstrated

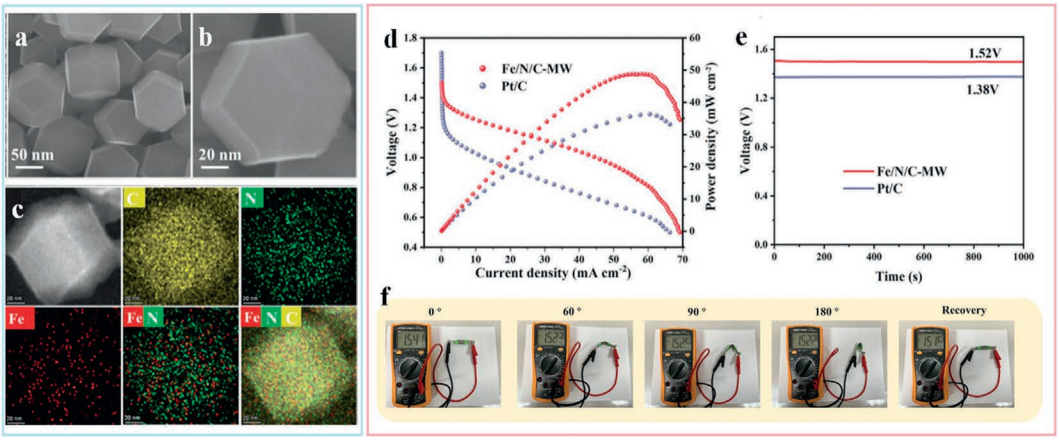


Fig. 7. (a, b) SEM images of Fe/N/C-MW samples. (c) HAADF-STEM images and corresponding energy spectral elemental mapping images of C, Fe, N, Fe & N, and Fe & N & C. (d) Polarization and power density curves of SZABs. (e) Open-circuit plots of SZABs. (f) Images of Fe/N/C-MW SZABs at different angles at OCV. Copied with permission [65]. Copyright 2023, Wiley-VCH GmbH.

Table 2
Properties of single atomic and doped electrocatalysts.

Catalyst	Electrolyte	Structure	OCV (V)	Peak power density (mW/cm^2)	Cycling (h/cycle)	Ref.
Ni/CNF-750	PVA	Sandwich	1.38	56.8	>30 cycles at 10 mA/cm^2	[66]
Fe_{SA}/Fe_{AC}@PPy/CC	PAM/EG	Sandwich	1.49 (25 °C) 1.41 (−40 °C)	98.8 (25 °C) 30.2 (−40 °C)	210 h at 2 mA/cm^2	[67]
Fe-SAC@N/CA-CD	PVA	Sandwich	1.44	124	>90 h at 5 mA/cm^2	[68]
Fe-N@CBs	PAM	Sandwich	1.5	151.3	>150 h at 2 mA/cm^2	[69]
Fe-NC@CNTs	PVA	Sandwich	1.45	130.8	90 h at 2 mA/cm^2	[70]
Co_{NPs}/NCF	PVA	Sandwich	1.4	115.9	–	[71]
D-Fe-N/C	PAM-CMC	Sandwich	1.42	122.6	520 h at 1 mA/cm^2	[72]
Fe-SAs/MPC	PVA	Sandwich	1.48	232	>100 h at 2 mA/cm^2	[73]
Fe-NS/C	PVA	Sandwich	1.533	126.9	500 h at 1 mA/cm^2	[74]

Fe_{SA}/Fe_{AC}@PPy/CC: Fe single atom sites and clusters coexisting on worm-like polypyrrole; EG: Ethylene glycol. CA: carbon aerogels; N, NPC: P-codoped carbon nanosheets; D-Fe-N/C: site density iron Fe-N/C; Fe-SAs/MPC: Fe single atoms anchored in microporous carbon.

a cycle-stable charging/discharging process that lasted more than 9 h under repeated flat (0°)/bent (90°)/flat (0°) states. Additionally, it exhibited stability over 110 cycles at 1 mA/cm^2 (Fig. 6h). Thus, Co-SACs are ideal for bifunctional oxygen electrocatalysis because of their excellent catalytic activity for both ORR and OER.

Apart from Co-SACs, other single-atom transition metal catalysts such as Fe-SACs and Ni-SACs have also been extensively studied. Yang *et al.* rapidly synthesized excellent-quality Fe/N/C SACs catalysts using microwave (MW) assistance [65]. This morphology exhibited significant and sharply defined edges (Fig. 7a) and an average particle size of ∼130 nm (Fig. 7b). The energy dispersive X-ray spectroscopy (EDX) map (Fig. 7c) indicated that N and Fe atoms in Fe/N/C-MW were uniformly distributed in the carbon skeleton. Upon combining the HR-TEM images and the elemental mapping images of Fe/N/C-MW, it was observed that Fe atoms were uniformly dispersed in the carbon matrix. Furthermore, SZABs were prepared using KOH-wetted PVA film as a solid electrolyte. The maximum power density of the Fe/N/C-MW-based SZAB was 49 mW/cm^2 (Fig. 7d). The OCV of Fe/N/ C-MW (1.52 V) was 0.14 V, which exceeded Pt/C (1.38 V) at a detection time of 1000 s (Fig. 7e). Additionally, the OCV values of SZAB with Fe/N/C-MW at various bending angles were tested using a multimeter. In Fig. 7f, the voltage values hardly changed regardless of the bending angle variation from 0° to 180°, thereby demonstrating extreme flexibility and wearability. Table 2 presents the performance of other recent SACs and doped electrocatalysts prepared for SZABs, detailing their voltage, power density, energy efficiency, and flexible applications [66–74]. These catalytic materials exhibited the finest metal particles (primarily Co, Fe, and Ni) distributed on the surface of the carrier to optimize the use of metal atoms.

Currently, the preparation of SACs remains a main challenge. Metal-based NPs, due to their high surface energy and small particle size, inevitably aggregate during preparation and long-term operation, thereby leading to the reduction of ORR active sites. Despite the property of such catalysts has been extensively modified, it is still far from satisfactory. Monatomic metal compounds (metal oxides, metal nitrides, and metal sulfides) are also potential candidates for replacing expensive Pt/C materials owing to their low price, ameliorative stability, and activity. Liu *et al.* introduced a nitrogen (N)-oxygen (O)-co-doped carbon spheres (NOCS) with uniformly abundant mesopores as a new carrier for entangled Co_3O_4 NPs to prepare Co_3O_4/NOCS composites (Fig. 8a) [75]. TEM images show that the Co_3O_4 NPs were well dispersed in the NOCS (Fig. 8b). Thus, the HR-TEM of Co_3O_4/NOCS revealed that the particle size was below 5 nm (Fig. 8c). The lattice stripe spacing of 0.467 nm corresponded to the (111) face of Co_3O_4 (Fig. 8d). The sandwich-type SZABs consisting of solid electrolyte, air electrode, and Zn foil were depicted in Fig. 8e. The power density reached 227 mW/cm^2 (Fig. 8f). It exhibited excellent multiplicative performance without significant potential loss at a resuming discharge of 10 mA/cm^2, thereby reflecting excellent ORR kinetics (Fig. 8g). Table 3 presents the relevant properties of single-atom metal compounds in recent years [76–84]. These materials involve hydroxides, oxides, sulfur compounds, and phosphides derived from transition metal elements such as Fe, Ni, and Co, which exhibit substantial combinatorial potentials to obtain OER and ORR properties. Because transition metal elements exhibit more than one va-

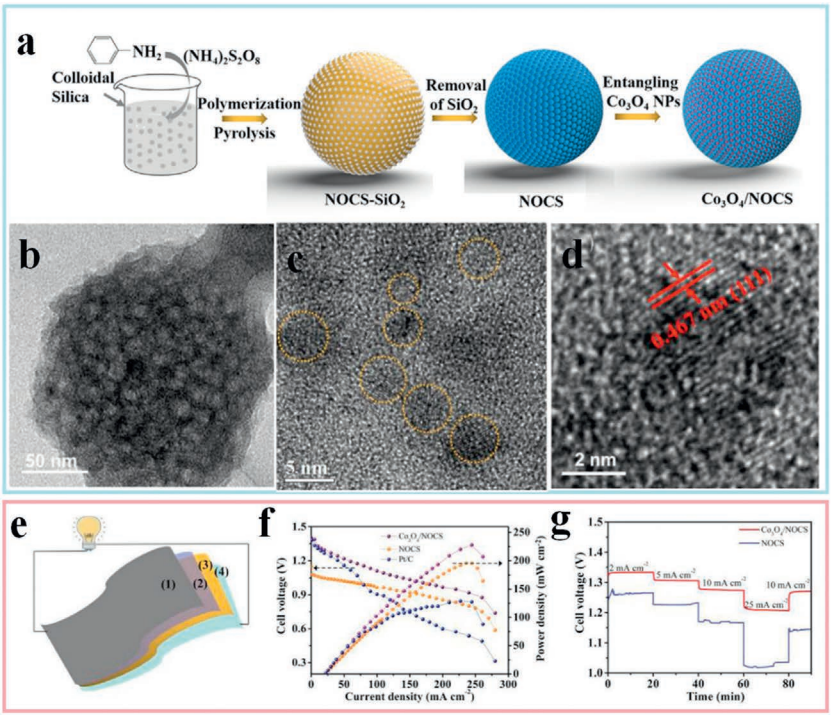


Fig. 8. (a) Preparation process of Co_3O_4/NOCS material. (b) TEM image and (c, d) HR-TEM images of Co_3O_4/NOCS. (e) Structure of FZAB: 1. Gas diffusion layer; 2. cathode; 3. solid electrolyte; 4. zinc-foil. (f) Polarization and power density curves of primary ZABs with Co_3O_4/NOCS, NOCS, and Pt/C as air electrodes. (g) Constant-current discharge curves of ZABs with Co_3O_4/NOCS and NOCS catalysts at different current densities. Copied with permission [75]. Copyright 2021, Elsevier Inc.

Table 3
Properties of monatomic metal compound carbon-based electrocatalysts.

Catalyst	Electrolyte	Structure	OCV (V)	Peak power density (mW/cm^2)	Cycling (h/cycle)	Ref.
IOSHs-NSC–Co_9S_8	PAM-*co*-PAA	Coplanar	1.408	60	105 cycles at 5 mA/cm^2	[76]
$Co_{5.47}$N@N-rGO-750	PAA	Sandwich	1.40	54.6	>40 h at 1 mA/cm^2	[77]
FeN_4@CNF-NH_3	PAA	Sandwich	1.49	33.7	>1.5 h at 1 mA/cm^2 under different bending degrees	[78]
A-MnO_2/NSPC	PVA-KOH	Sandwich	1.37	75	>140 cycles at 5 mA/cm^2	[79]
Co_3O_4/CoNGDY	PAM	Cable	1.39	167.6	>48 h at 25 mA/cm^2	[80]
VMoON@NC	PVA	Sandwich	–	–	20 h at 10 mA/cm^2	[81]
CoO@NBC	PAAM	Sandwich	1.39	59.8	>400 cycles at 1 mA/cm^2	[82]
V−Co_3O_4	PVA	Cable	1.39	396	4100 h at 5 mA/cm^2	[83]
Fe_3C@NPW	PAA	Sandwich	1.39	78	>50 h at 2 mA/cm^2	[84]

IOSHs-NSC–Co_9S_8: inverse-opal-structured hybrids of N, S-codoped-carbon-confined monodisperse Co_9S_8 nanoparticles; NGDY: N-doped graphdiyne; NC: nitrogen-doped carbon; CC: carbon cloth; VMoON: vanadium molybdenum oxynitride cores; NBC: nitrogen-boron co-doped carbon nanotube; PAAM: polyacrylamide.

lence electron, their compounds of different compositions exhibit different activities and structures. Different methods are needed to regulate their morphology and select suitable combinations.

Despite the advantages of low cost, abundant reserves, and strong redox properties, transition metal oxides (TMOs) face challenges of poor conductivity and limited active sites. Recently, studies have shown TMOs from aspects of interface engineering and structural design. It was observed that the construction of heterogeneous interfaces is a useful strategy to accelerate the adsorption of reaction intermediates, increasing the active site, regulating the electron distribution, and enhancing the reactivity of oxygen [85,86]. Transition metal sulfides (TMSs) with outstanding intrinsic conductivity, excellent electrocatalytic stability, and abundant reaction sites are considered ideal choices for heterostructure hybridization with TMOs. The introduction of TMSs into TMOs to form a two-compound catalyst generated a large number of O vacancies, serving as highly active sites, enhancing the hydrophilicity of the catalyst, and improving the O reaction kinetics [87]. Wang *et al*. constructed an effective mesoporous CoS/CoO heterojunction nanorods (CoS/CoO PNRs) bifunctional oxygen electrocatalyst88 (Fig. 9a) [88]. The prepared CoS/CoO PNRs exhibited diversiform advantages, such as mesoporous rod-like structure, rich heterogeneous interfaces, enhanced O vacancies, and biphasic synergy (Figs. 9b–g). The assembled CoS/CoO PNRs SZAB exhibited a OCV of 1.35 V (Fig. 9h) and a peak power density of ~58.8 mW/cm^2 (Fig. 9i). In practice, two cells in a series successfully illuminated the LEDs. When discharged at different current densities, the CoS/CoO PNR-based ZAB exhibited excellent multiplicative performance without obvious voltage decrease as the current density returned to its initial value (Fig. 9j). Finally, under the 1 mA/cm^2 constant-current discharge/charge test, the ZAB based on CoS/CoO PNRs remained steady for 16.7 h (Fig. 9k). Table 4 summarizes the relevant properties of carbon-based electrocatalysts combined with single-atom TMOs and single-atom TMSs in recent years [89–92]. The introduction of TMSs into TMO formed an excellent heterostructure, thus regulating the electron distribution, expediting the adsorption of reaction intermediates, and increasing the active site. Additionally, it also produced a large number of

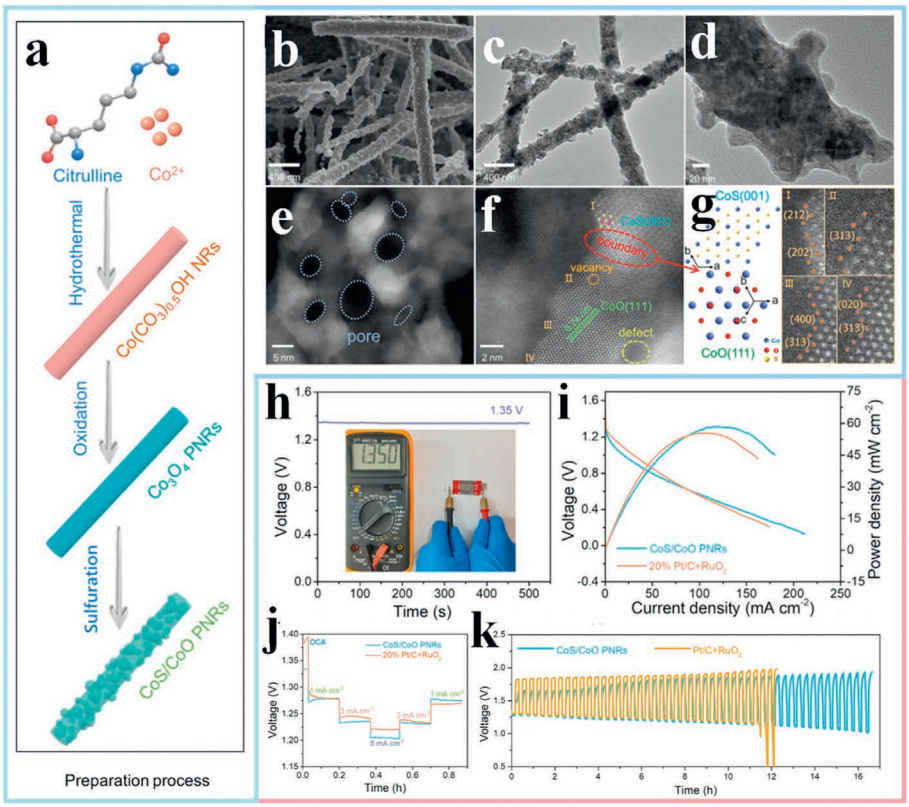


Fig. 9. (a) Schematic illustration of CoS/CoO PNRs synthesis. (b) SEM images and (c–e) TEM images of CoS/CoO PNRs. (e, f) HAADF-STEM images of CoS/CoO PNRs. (g) Atomic structure superposition diagrams and high refractive index crystalline images of CoS (001) and CoO (111). (h) OCV of ZAB driven by CoS/CoO PNRs. (i) Discharge polarization curves and corresponding power density maps of ZAB. (j) Discharge curves at different current densities. (k) Constant-current charge/discharge cycling curves at 1 mA/cm^2. Copied with permission [88]. Copyright 2022, Elsevier B.V.

Table 4
Properties of carbon-based electrocatalysts with different compounds formed by identical transition metal atoms.

Catalyst	Electrolyte	Structure	OCV (V)	Peak power density (mW/cm^2)	Cycling (h/cycle)	Ref.
CoS/CoO@NGNs	PVA	Sandwich	1.3	39.3	>100 h at 10 mA/cm^2	[89]
Co_2P/CoN-in-NCNTs	PVA	Coplanar	1.376	58.8	>8 h at 1 mA/cm^2 under different bending degrees	[90]
FeP/Fe_2O_3@NPCA	PVA	Sandwich/cable	1.42	40.8	>4 h at 5 mA/cm^2	[91]
FeSA-FeNC@NSC	PVA	Sandwich	1.4	55.86	>2 h at 5 mA/cm^2	[92]

NGN: N-doped graphene; NCNTs: nitrogen-doped carbon nanotubes.

O vacancies, which served as high active sites, thereby enhancing the hydrophilicity of the catalyst and improving the O reaction kinetics. In comparison with the single-atom metal compounds previously described, different compounds formed from the same transition metal atoms exhibited a significant density of states (DOS) enhancement near the Fermi level due to the interaction of the two-electron layers, thereby enhancing the OER and ORR performance of the catalyst.

In summary, Fe, Co, Ni and other single-atom transition metals, TMOs and TMSs are widely used in SACs to enhance the catalytic performance of ZABs due to their low cost and abundant reserves. Unfortunately, the isolated single atomic sites in SACs increase the surface energy, resulting in the aggregation of metal atoms during the preparation process, which attenuates the catalytic activity.

2.2.3. Multiatomic transition metals and their compounds for carbon-based electrocatalysis

Recently, mixed metal atomic catalysts have emerged as promising alternatives to monoatomic transition metals and their derivatives for carbon catalysis, which often exhibit moderate ORR performance. The introduction of foreign metal cations enhances the catalytic sites, thereby creating new active sites [93–117]. Furthermore, the coordination effect between neighboring metal atoms alters the electron configuration, decreasing the reaction energy barriers, and enhancing and improving the overall catalytic performance [118]. It was observed that the introduction of another metal active center in the presence of FeN_x affects the OER/ORR activity. For instance, during the ORR process, the 3C-2e bonds (one electron coming from O and another mutually contributed by the bimetal, Fe−Mn) between the adsorbed O_2 molecules and the Fe–Mn binary metal sites facilitated the adsorption and desorption of O at the Fe and Mn ends, respectively [108]. The traditional concept of "synergy" was formulated between them, which modulated the local coordination environment of the active sites and enhanced the catalytic process. Intentional introduction of bimetallic or mixed metal sites enhanced the chemical and electronic properties of bifunctional catalysts, which exhibited more attractive properties and higher catalytic performance compared with monometallic catalysts due to unique electronic effects and additional synergies. Additionally, it was observed that Fe–Co bimetals facilitated O binding at low activation energies. Thus, it

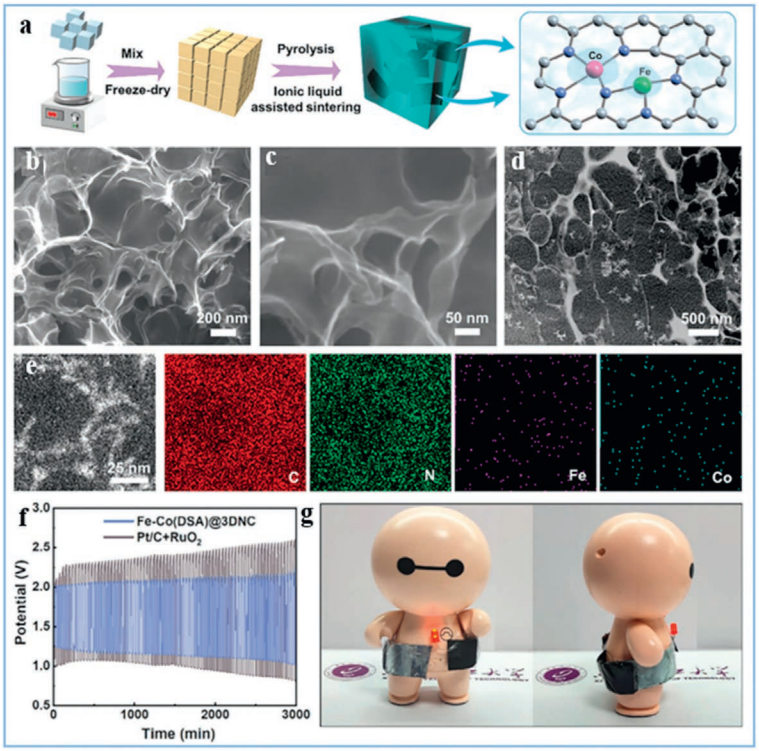


Fig. 10. (a) Schematic illustration of the fabrication process for Fe–Co(DSA)@3DNC. (b, c) SEM images, (d) TEM images, (e) STEM images along with elemental mapping of the Fe–Co(DSA)@3DNC. (f) Long-term cycle performance of SZABs. (g) A doll equipped with a flexible battery successfully powers an LED lamp. Copied with permission [119]. Copyright 2024, Wiley-VCH GmbH.

facilitated the initial onset of ORR. The interaction between these bimetals (Co and Fe) facilitated the formation of Fe-O-O–Co bonds, which are one of the key intermediates of ORR. Subsequently, Fe dominated the ORR activity and the long-term stability of the ORR was attributable to the presence of Co. Li *et al*. utilized NaCl as a template to dissolve the metal source, ammonium citrate, and melamine in deionized water. They effectively synthesized bimetallic Fe/Co 3D NC catalyst Fe–Co (DSA)@3DNC after freeze-drying and high-temperature treatment (Fig. 10a) [119]. Furthermore, SEM and TEM images showed that the Fe–Co (DSA)@3DNC catalyst consisted of an ultra-thin carbon network with a porous structure, which facilitated the transfer of gases and electrons in the reaction (Figs. 10b-d). The STEM image and the corresponding element map revealed the uniform distribution of Fe and Co, thereby indicating a monatomic structure (Fig. 10e). Furthermore, Fe–Co (DSA)@3DNC, Zn, and GPEs were assembled into SZABs as air cathodes, anodes, and electrolytes, respectively, with a cycling performance of over 3000 min and a charge–discharge potential gap much lower than Pt/C+ RuO_2-based SZABs (Fig. 10f). Additionally, the use of SZABs wrapped around the doll facilitated the LED operation for over 10 h, thereby indicating that the prepared SZABs exhibited extremely high safety for wearable devices (Fig. 10g). The reason for the excellent performance of Fe–CO (DSA)@3DNC assembled SZABs was that the asymmetric configuration of Fe and Co sites formed strong charge polarization between them due to electron transfer, which enhanced the delocalization of D-band electrons, thereby significantly accelerating the electron conduction. Additionally, the presence of Co inhibited O adsorption intermediates in the OER/ORR reaction, thereby ultimately reducing the reaction energy barrier. Table 5 presents the relevant properties of the carbon-based materials with multiple different metal atomic sites [120–128]. These materials are primarily designed as alloy catalysts containing two or more transition metal atoms. Catalysts with complex structures can harness the potential advantages of multiple material configurations, thereby enhancing bifunctional electrocatalytic performance. Additionally, alloys doped with carbon that are incorporated into the ORR active sites represent a promising strategy for the development of bifunctional OER/ORR electrocatalysts.

Recently, researchers have found that mixed metal compounds (oxides, sulfides) containing Co, Fe, or Ni are ideal choices for the electrocatalysts of OER and ORR under alkaline conditions [129,130]. Given that NiFe oxide (Fe_2NiO_4) exhibited the advantages of abundant valence, high corrosion resistance, and structural flexibility, NiFe sulfide ($FeNiS_2$) exhibited a moderate natural adsorption capacity for reaction intermediates. Li *et al*. combined Fe_2NiO_4 and $FeNiS_2$ to prepare a Fe_2NiO_4/$FeNiS_2$ hollow structure microtubule catalyst (Fe_2NiO_4/$FeNiS_2$ MTs), thereby accelerating the kinetics of OER and ORR [131]. Subsequently, Fe_2NiO_4/$FeNiS_2$ MTs exhibited a hollow structure with a huge specific surface area, exposing many accessible active sites for electrochemical reactions, accelerating the diffusion and penetration of electrolyte and reactant molecules, thereby releasing bubbles (Fig. 11a). Furthermore, Fe_2NiO_4/$FeNiS_2$ microtubules were composed of a large number of nanosheets (NSs) (two, three, and four layers) (Figs. 11b and c). The splitting between Fe_2NiO_4 and $FeNiS_2$ MTs phases enhanced Fe_2NiO_4/$FeNiS_2$ MTs material with a rich heterogeneous interface at these domain boundaries, thus offering excellent electrocatalytic activity for ORR and OER (shown by the yellow curve in Fig. 11d). Two different types of crystal face spacing (0.296 nm and 0.251 nm) were observed in HR-TEM images of a single nanosheet, corresponding to the (100) crystal face of $FeNiS_2$ and (113) crystal face of Fe_2NiO_4, respectively, thereby indicating the presence of Fe_2NiO_4 and $FeNiS_2$ phases in Fe_2NiO_4/$FeNiS_2$ MTs (Fig. 11e). The strong coupling between Fe_2NiO_4 and $FeNiS_2$ and the dual advantages of morphological structure made Fe_2NiO_4/$FeNiS_2$ MTs exhibit superior electrocatalytic activity (Fig. 11f). It was observed from the ORR polarization curve obtained through linear sweep

Table 5
Properties of multiple different metal atomic sites and doped electrocatalysts.

Catalyst	Electrolyte	Structure	OCV (V)	Peak power density (mW/cm^2)	Cycling (h/cycle)	Ref.
Fe-N/FeCo@NGA	PAA	Sandwich	1.54	147.6	140 h at 10 mA/cm^2	[120]
FeCoNi FCNFs	PVA	Sandwich	1.46	70	>28 h at 10 mA/cm^2	[121]
$FeNi_{SAs}$/NC	GPEs	Sandwich	1.49	151.06	130 h at 10 mA/cm^2	[122]
Co_3Fe_7/NC-50	PVA	Sandwich	1.47	–	>30 h at 1 mA/cm^2	[123]
Co,S-MnSe/N-rGO	PVA	Sandwich	1.4	140.2	5400 cycles at 10 mA/cm^2	[124]
FeCo-CP/FeSA-CN	PVA	Sandwich	1.4	164	>120 h at 2 mA/cm^2	[125]
CoFe/Fe_3C-T_2	PVA	Sandwich	1.431	95	>6 h at 5 mA/cm^2 (bending angle)	[126]
CoCrFe@WGNF	PAM	Sandwich	1.3	140.8 (25 °C) 63.3 (−40 °C)	>90 h at 2 mA/cm^2 (−40 °C)	[127]
CoFeCu-TAC	PAM	Sandwich	1.494 1.603 (−40 °C)	184	210 cycles at 2 mA/cm^2 (−40 °C)	[128]

NGA: nitrogen-doped graphene aeroge; FCNT: flexible carbon nanofibers; N-rGO: nitrogen-doped reduced graphene oxide; CP: carbon polyhedrons. T_2: specific pyrolysis temperature employed during the synthesis process is 800 °C; WGNF: wrinkled graphene nanoscroll-fibers; TAC: triatomic catalyst.

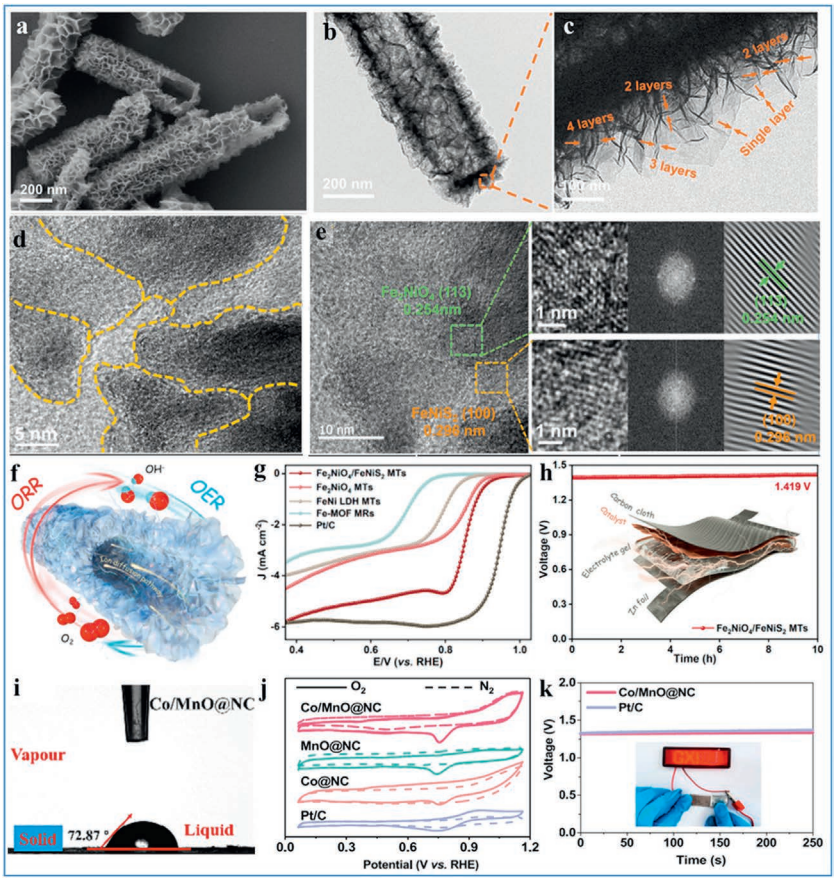


Fig. 11. (a) Field emission scanning electron microscope (FE-SEM), (b, c) TEM, (d, e) HR-TEM images of the $Fe_2NiO_4/FeNiS_2$ MTs. (f) Schematic illustration for the structural advantages of $Fe_2NiO_4/FeNiS_2$ MTs in electrocatalysis of the ORR and OER. (g) LSV curves of $Fe_2NiO_4/FeNiS_2$. (h) OCV of SZAB based on the $Fe_2NiO_4/FeNiS_2$ MTs (inset: schematic illustration for the assembly of SZAB device). Copied with permission [131]. Copyright 2024, Elsevier (i) Contact angle measurements of Co/MnO@NC. (j) CV curves in N_2 or O_2-saturated 0.1 mol/L KOH solution. (k) OCVs of Co/MnO@NC and Pt/C-based FSZABs (inset: Co/MnO@NC-based FSZAB-lit LED board). Copied with permission [132]. Copyright 2024, Elsevier.

voltammetry (LSV) that $Fe_2NiO_4/FeNiS_2$ MTs exhibited outstanding ORR catalytic performance with positive initial voltage and ideal catalytic current density (Fig. 11g). Thus, SZAB was assembled using $Fe_2NiO_4/FeNiS_2$ MTs as the air cathode material with an OCV value of 1.419 V and a maximum power density of 81.74 mW/cm^2 (Fig. 11h). Additionally, under different bending conditions, the voltage gap of SZAB was almost unchanged, which indicated exceptional cyclic performance. Wang *et al.* synthesized a vacation-rich Co/MnO@NC catalyst by fixing cobalt/manganese oxide Co/MnO prepared by pyrolysis and hydrothermal method on a nitrogen-doped carbon (NC) support [132]. The contact angle of 72.87° for Co/MnO@NC catalyst was much lower than that of Co@NC (116.93°) and MnO@NC (132.68°), suggesting that MnO and Co coupling produced a more hydrophilic surface, enabling liquids containing dissolved oxygen to enhance wettability and thus promote ORR at the interface (Fig. 11i). In addition, compared with Pt/C, MnO@NC and Co@NC, Co/MnO@NC had the highest cathode peak position, indicating excellent ORR activity (Fig. 11j). The OCV of Co/MnO@NC catalyst assembled SZAB was higher than that of Pt/C-based SZABs due to the synergistic effect between defective MnO and Co, which promoted rapid electron transfer and improved adsorption of oxygen reactants (Fig. 11k).

Table 6
Properties of metallic compounds with multiple metal sites compound carbon-based electrocatalysts.

Catalyst	Electrolyte	Structure	OCV (V)	Peak power density (mW/cm^2)	Cycling (h/cycle)	Ref.
Co/MnO@NC	PVA	Sandwich	1.36	63.3	–	[132]
FeN_4/G/FeCo	PANa-PEO	Sandwich/cable	1.4	197.2	495 cycles at 3 mA/cm^2	[138]
$Ni_{0.6}Fe_{2.4}O_4$@NC	PVA-KOH	Sandwich	1.36	66.1	>43 h at 5 mA/cm^2	[139]
$NiCo_2O_4$	PVA	Sandwich	1.28	20	>7 h at 1 mA/cm^2	[140]
MnO/Co@NC	PAAK-M	Sandwich	1.51	63	>44 h at 2 mA/cm^2	[141]
$FeNiCoO_4$	PVA	Sandwich	1.43	21.8	>100 cycles at 2 mA/cm^2	[142]

G: graphene; PEO: polyoxyethylene.

Additionally, this monatomic composition of the alloy type and differences in the internal lattice strain of the metal alloys lead to differences in their structural ordering and redox potentials. Thus, the coupling of metal alloys and metal oxides further enhanced the catalytic activity due to the formation of Schottky barriers between them, thereby favoring charge separation [133–136]. However, establishing effective mass transfer channels remains a serious challenge. Duan *et al*. obtained an efficient bifunctional oxygen catalyst (CoNi-CoO–NiO@NC-800) through one-step pyrolysis [137], which endowed SZABs with high OCV (1.366 V) and maximum power density (223 mW/cm^2). The reason for the superior performance of the SZABs prepared using CoNi-CoO–NiO@NC-800 was that the layered porous structure and specific surface area of the catalyst facilitated the transfer of electrons and reactants. Furthermore, CoO and NiO catalyzed OER reactions, while CoNi-N_x, pyridine N, and CoNi alloy catalyzed ORR reactions. Subsequently, the defect carbon content of the catalyst exceeded that of graphite, which increased the catalytic active site. Table 6 presents the relevant properties of various metal compound catalysts with multiple metal sites in recent years [132,138–142]. Despite combining the advantages of multiple transition metal compounds, these materials were more complex to debug and combine, and the most critical technologies were: (1) How to optimize the inherent low conductivity of the compound and poor nanoparticle dispersion; and (2) whether the synergistic effect of the multiple compounds introduced enhanced the charge transport rate and ultimately the performance of the catalysts.

Additionally, metal-free carbon-based catalysts, single-atom transition metal, and its compound catalysts, as well as multi-atom and its compound catalysts addressed the shortcomings of precious metal catalysts with high cost, weak stability, and single function, thereby exhibiting significant potential in SZABs. The prior art of metal-free carbon-based catalysts depends significantly on ZIFs, resulting in complex steps, uncontrollable morphology, and aggregation of metal nanoparticles. This not only limited the N concentration and density of the active site in doped carbon but also damaged the flexibility of the catalysts. A novel fiber catalyst can be designed and a secondary N source can be introduced to enhance its self-supporting flexibility, thereby increasing the density of the metal active site. Furthermore, ACs have garnered attention in SZABs due to their precise atomic coordination, maximum atomic utilization, and adjustable electron configuration. The most effective ways to improve the catalytic activity of SACs were to introduce defects into the carbon matrix, enhance its specific surface area, and employ specific heteroatoms as well as guest groups. Unfortunately, the need to precisely control the synthesis process leads to expensive, time-consuming, and complex issues. The introduction of two or more metal atoms in SACs to achieve atomic synergy enhanced the adsorption–desorption of substances at the active site. Oxides of Co, Ni, and Fe have become the most common OER catalysts. Mixed oxides of Mn and Fe have also been extensively studied, and special mixed oxide catalysts such as (Mn, $Fe)_3O_4$ were rarely utilized in SZABs. In the future, non-precious metal catalysts with stability and high efficiency can be developed to enhance the performance of SZABs. Additionally, given that atomic layer deposition can deposit the catalyst layer in the pores deep in the particles of the gas diffusion layer, the design of atomic layer deposition of trimetallic oxides remains an ideal choice.

In summary, the combination of Fe, Co, Ni and other transition metals and their compounds to form bimetal or mixed metal sites can further improve the catalytic activity, durability and stability of catalysts. However, the catalytic mechanism of these catalysts is still unclear and it is difficult to accurately control the atomic and electronic structures of these catalysts.

2.3. Electrolyte

As a crucial part of the battery, electrolytes not only conduct hydroxide ions and prevent Zn oxide ions from migrating to the air electrode but also determine the interface chemistry and ion transport between the negative and positive electrode. This was the main factor limiting the performance enhancement of ZABs [143,144]. Traditional liquid electrolytes (LEs) are the most commonly utilized electrolytes owing to their excellent-ionic conductivity (IC) and stable electrochemical performance [145]. However, the side reactions such as corrosion and hydrogen evolution reaction (HER) during the water decomposition process in LEs, result in dendrite challenges and passivation of the Zn anode surface, which ultimately leads to low battery efficiency [146]. Additionally, LEs contain a substantial amount of organic matter, which poses leakage risk, spontaneous combustion, and explosion [147]. Given the mass application of Zn cells, the safety of LEs has garnered attention, and the transition from LEs to SEs aided the realization of flexible applications of SZABs. Notably, SEs exhibited excellent safety performance, high-IC, excellent chemical compatibility with other components, and exceptional mechanical strength [148]. Additionally, SEs inhibited the formation and growth of Zn dendrites, which replaced LEs and enhanced the mechanical robustness, safety, and stability of ZABs, as well as broadened the application range of ZABs [149]. Additionally, SE itself is light, which can effectively decrease the weight of the cell and realize the high-performance development of the cell [150,151]. Therefore, SEs exhibit several advantages over LEs and are suitable for large-scale application in SZABs. This section primarily discusses the classification and application of solid electrolytes in SZABs from the electrolyte direction, thereby offering a new perspective for enhancing the performance stability of SZABs.

2.3.1. Solid-states electrolyte types

The SEs commonly utilized in SZABs were divided into two types: polymer electrolytes (PEs) and ion exchange membranes (IEMs) [150,151]. According to their composition, PEs for SZABs are generally divided into three broad categories: Solid-state polymer electrolytes (SPEs), gel polymer electrolytes (GPEs), and hybrid polymer electrolytes (HPEs) [146,152]. Thus, IEMs are usually referred to as anion exchange membranes (AEMs) (Fig. 12) [153]. Additionally, some researchers have divided electrolytes into alka-

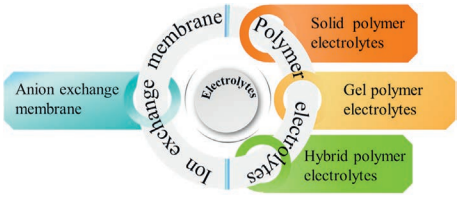


Fig. 12. SZABs electrolyte classification.

line electrolytes and neutral electrolytes (NEs) according to their potential hydrogen (pH) value [154,155].

Polyoxyethylene (PEO) became the first polymer to be used because of its advantages such as outstanding flexibility, excellent stability, and low-cost. Nevertheless, its low water absorption, poor electrode interface performance, and a sharp decline in conductivity under high salt concentration limit its application, thereby necessitating the need for new polymers [156]. Polyacrylamide (PAM), polyacrylic acid (PAA), PVA, and sodium polyacrylate (PANa), which contain many hydrophilic groups on their side chains absorb substantial amounts of water. This has garnered significant attention in recent years and it can be used as a substitute for PEO [146,157,158]. Fig. 13 shows several common polymer substrates, all of which exhibit unique properties, advantages, and disadvantages. Furthermore, SPEs exhibit high flexibility, thereby addressing the issue of poor electrode interface stability. Meanwhile, Zn salt dissolved directly through the polymer chain retaining a small amount of organic solvent. However, its poor interface compatibility with the electrode and low IC limit its wide application [159,160]. Typically, HPEs are copolymerized or cross-linked by several polymers, exhibiting electrochemical stability and high-IC, thereby achieving rapid ion transmission in the charge–discharge process. Similarly, the HPEs enhanced the energy density, cycle life, and battery safety, thereby broadening its application prospects in SZABs [161]. Typically, GPEs swell significantly when exposed to water dissolved with Zn salts, existing as an intermediate product between solid and liquid states. They are condensed materials synthesized through the polymerization of polymeric monomers [162,163]. Upon combining the high-IC of LEs with the safety of SEs, these electrolytes offer several advantages, including high-IC, low-interface impedance, high-thermal stability, and mechanical flexibility. Thus, they are considered promising candidates for SZABs [164,165]. Despite SPEs are similar to GPEs when serving as PEs, there are some differences between them. In GPEs, a 3D network is typically formed through the cross-linking of polymer molecules, thereby offering a large amount of space for electrolyte absorption. The weight ratio of the received electrolyte exceeded that of the polymer 3D network. In SPEs, the electrolyte was absorbed into the polymer solid film, and the electrolyte-to-polymer material ratio was low [143].

It was observed that AEM was prepared through the impregnation of alkaline functional groups in the polymer framework, which served as a safe and environmentally friendly OH^- conductor. The inherent OH^- was transferred by cations, which significantly reduced corrosion. However, its IC was low, and its water retention was enhanced [166]. Presently, AEMs have been extensively used in alkaline fuel cells and redox batteries, thereby exhibiting excellent application prospects, such as commercial A201 membranes [167].

2.3.2. Characteristics of solid-state electrolyte for zinc-air batteries

Notably, SEs exhibit strong interface contact with electrodes, excellent environmental stability, high-IC, high-water retention and absorption capacity, and excellent mechanical strength are critical factors determining the property of SZABs [168]. The tight contact between the electrolyte and the catalyst layer ensures the smooth redox reaction of the air electrode in SZABs [169]. Furthermore, there are abundant concave–convex parts on the Zn electrode surface, exhibiting excellent contact between the interface of the electrolyte and the Zn electrode, thereby inhibiting dendrite growth and HER [170]. However, SZABs are faced with large deformation conditions, inevitably leading to electrolyte displacement, leading to the electrolyte falling off the electrode surface, and eventually resulting in the deterioration of cell performance. In summary, an increase in the viscosity of the electrolyte or enhancing the chemical action in the electrolyte can improve the contact between the electrode surface and the electrolyte, which exhibits a crucial impact on the power output and cycle life of SZABs. For instance, Hui *et al.* developed an LDH-array@PVA electrolyte with excellent water retention and high-IC. They introduced a two-dimensional (2D) filler-layered double hydroxide (LDH) rich in hydroxyl groups into the PVA, which was then infiltrated into the MXene/Zn electrode to achieve electrode-electrolyte integration [171]. The integrated interface structure effectively prevented poor contact at the electrolyte-electrode interface, which can occur due to the volume contraction induced by water depletion during the cycling of the SPEs. This structure demonstrated excellent compatibility and stability, thus reducing interface impedance and suppressing the growth of Zn dendrites. Furthermore, utilized in SZABs, it exhibited a cycle life of ~50 h and an excellent power density of ~92.3 mW/cm^2, thereby significantly exceeding the peak power density of pure PVA-based ZAB (44.8 mW/cm^2). Additionally, it exhibited excellent stability at different bending angles. However, some studies have shown that during the discharge process, an insulating Zn oxide passivation

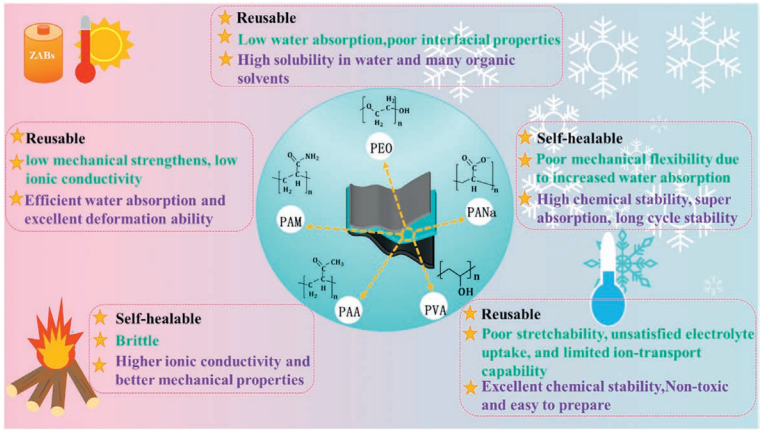


Fig. 13. Common solid electrolyte polymer matrix systems (properties (black), advantages (purple), and disadvantages (green)).

film forms between the Zn electrode and the SEs interface, thereby eventually leading to battery capacity decline and electrode failure. Therefore, enhancing the wettability of SEs to obtain exceptional solid–solid interface contact is a promising strategy for increasing the discharge capacity of SZABs. Zuo *et al*. selected the amphiphilic F127 (polyoxyethylene-polyoxyethylene propylene-polyoxyethylene (PEO100-PPO65-PEO100) triblock copolymer) surfactant as the SPE. This electrolyte was immersed into porous Zn through the inner hole. Furthermore, the porous Zn electrode and the electrolyte were in close contact, which enhanced the specific area capacity of SZABs (133 mAh/cm^2), inhibiting the battery breakdown due to the Zn oxide passivation layer, thereby exhibiting excellent anti-passivation performance [172].

Batteries are very sensitive to environmental conditions, particularly temperature. Given the special semi-open structure of ZABs, the solid electrolyte was inevitably affected by temperature [173]. At low temperatures, the electrolyte can freeze, lose elasticity, and deteriorate IC, thereby leading to a reduction in the overall performance of the battery [174,175]. However, at high temperatures, the dehydration process of the electrolyte was accelerated, resulting in its structural deformation, leading to spatial separation from the electrode, and reducing the ability to inhibit Zn dendrite [176]. Furthermore, high temperature exacerbated the HER, thereby decreasing the anode Faraday effect. Therefore, the development of SEs with excellent temperature resistance is significant to enhance the performance of SZABs operating at extreme temperatures. Recently, to enhance the performance of SZABs in extreme environments, a lot of research has concentrated on the composition of materials and the structural design of electrolytes [177]. Furthermore, GPEs consist of a polymer matrix combined with ionic liquids (ILs), which typically contain conductive salts, bases, or acids. These components were dispersed in aqueous solutions or organic solvents such as ethylene glycol (EG) and dimethyl sulfoxide (DMSO) [178]. For instance, Niu *et al*. synthesized C20E1G5 organic GPEs with high-IC ranging from 23.94 mA/cm to 68.68 mA/cm at −40∼60 °C, using cellulose NPs (20 mL) as the basic backbone, epichlorohydrin (ECH, 1 mL) as the cross-linking agent, and EG (5 mL) as the antifreeze agent [179]. Gu *et al*. developed organic GPEs (O-P(AA-*co*-AM)) with an interconnected porous structure which can be operated at a wide range of temperatures from −50 °C to 60 °C, by incorporating DMSO as an additive into P(AA-*co*-AM) hydrogels made from a dual network of PAM and PAA [180]. The IC of GPEs at 60, 0, −30 and −50 °C was 291, 74.3, 46.6 and 40.91 mS/cm, respectively, and the OCV of SZABs assembled with O-P(AA-*co*-AM) at 60 °C was 240 mW/cm^2. S=O and O–H in DMSO could form strong hydrogen bonds with H_2O molecules, thus enhancing the stability of GPEs at wide temperatures and easing the formation of Zn dendrites. Moreover, considering that organic solvents inevitably reduce the IC of electrolytes, various low-cost additives such as cellulose and low-concentration salts have been introduced into electrolytes in recent years, thereby enhancing their wide-temperature operation range. Lei *et al*. prepared a gel electrolyte (defined as AGC-T) by introducing $Zn(CF_3SO_3)_2$ into bionic fats (A-PAA/G-CyBA, defined as AGC) with G-CyBA supramolecular and A-PAA networks [181]. Furthermore, SEM revealed that AGC exhibited a supramolecular network with a layered porous structure, with an aperture of ∼5–10 μm (Fig. 14a). Subsequently, due to this layered porous structure, the AGC electrolyte absorbs massive of water molecules and electrolytes. It was observed through Fourier transform infrared (FT-IR) that the vibration peaks of C=O and COO- of A-PAA were located at 1706 cm^{-1} and 1575 cm^{-1}, respectively, which indicated the successful preparation of AGC electrolyte (Fig. 14b). The weak peak of the B signal in AGC (17.72, 1.5 ppm) was more pronounced in 11B nuclear

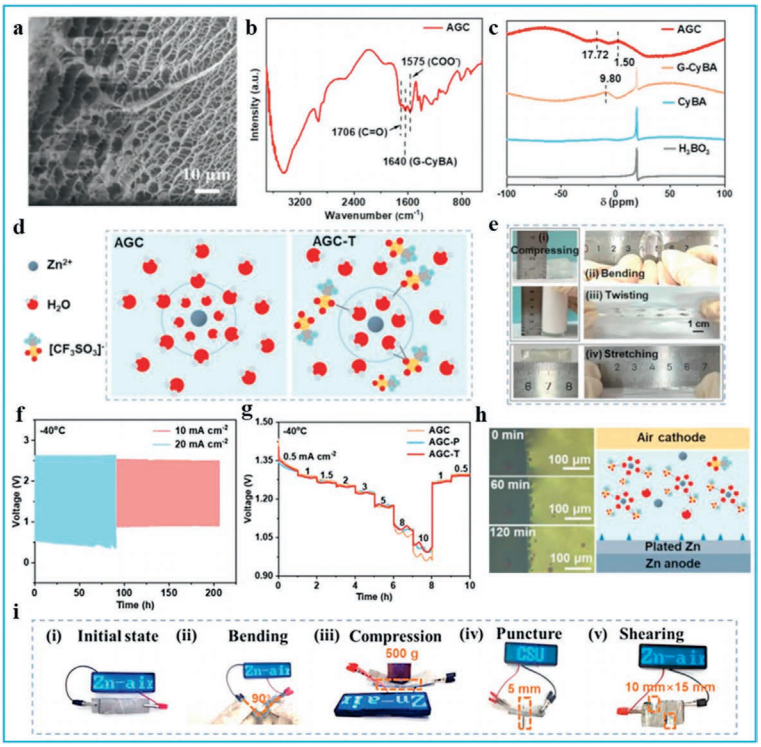


Fig. 14. (a) SEM image and (b) FT-IR spectra of the AGC gel of biomimetic fat. (c) ^{11}B NMR spectra of H_3BO_3, free CyBA, G-CyBA gel, and the AGC gel of biomimetic fat. (d) The schematic illustrations of Zn^{2+} solvation structure in AGC and AGC-T. The blue circles correspond to the solvation sheath structure of Zn^{2+}. (e) Schematic illustration of compressing, bending, twisting, and stretching at −40 °C. (f) The charge–discharge cycling curves at 10 mA/cm^2 and 20 mA/cm^2 of ZABs with AGC-T. (g) Rate performance of the ZABs with AGC-T, AGC-P, and AGC hydrogel electrolytes at −40 °C. (h) *In-situ* optical visualization observations of the Zn|electrolyte interface at 8 mA/cm^2 and schematic illustrations of Zn dendrite growth in AGC-T gel electrolytes. (i) Images of safety tests of AGC-T. Copied with permission [181]. Copyright 2023, Wiley-VCH Gmbh.

magnetic resonance spectroscopy (NMR) spectra (Fig. 14c), which indicated that G-CyBA borate complex (**1c**) was formed by cis-diol of guanosine and CyBA's borate group under alkaline conditions. The introduction of $Zn(CF_3SO_3)_2$ into AGC was conducive to the formation of more hydrogen bonds with water molecules and the reconstruction of the solvated sheath structure of Zn^{2+} (Fig. 14d), which inhibited dendrites. In the differential scanning calorimetry (DSC) curve of AGC-T, the solid–liquid transition temperature was < -80 °C, and at -40 °C, the AGC-T electrolyte remained highly flexible and elasticity under different deformations such as compression, bending, twisting, and stretching (Fig. 14e). At -40 °C, the cycle of the AGC-assembled SZABs reached 200 h (10 mA/cm^2), and when the potential was restored at a low current density, it indicated excellent reversibility and rate performance (Figs. 14f and g). Additionally, the SZABs assembled with AGC-T exhibited a smooth Zn surface after the cycling process at -40 °C, and the LED panel operated normally under various mechanical states (Figs. 14h and i). Recently, Bai *et al*. were inspired by the fact that biological cell membranes exhibit a hydrophilic head and a hydrophobic tail. They successfully prepared PANa-SDBS GPEs with a large number of pores by adding sodium dodecyl benzene sulfonate (SDBS) to PANa. Subsequently, PANa-SDBS GPEs exhibited a large number of pore structures that are conducive for electrolyte capture, thus enhancing the stability of the Zn-electrolyte interface at extreme temperatures [182]. Additionally, the hydrogen bond, cation-p interaction, and hydrophobic carbon chain interaction on the surface of PANa-SDBS GPEs decomposed ZnO deposited on the Zn surface, thus inhibiting the growth rate of the passivated layer. Thus, SZABs assembled with PANa-SDBS GPEs exhibited stability at -60 °C (4 mA/cm^2) for 173 h. Given the formation of a substantial number of hydrogen bonds between EG and H_2O, the saturated vapor pressure of water was reduced, thereby reducing its freezing point, and H_2O evaporation at high temperatures. The coin SZABs assembled using the prepared organic GPEs exhibited stable cycling for 200 h at 2 mA/cm^2 over a wide-temperature range of $-40\sim60$ °C. Given the poor-water retention, low IC, and irreversible dendrite growth of traditional PAV-SEs, its application in a wide-temperature environment was limited. Cellulose nanofibers (CNF) not only utilized a strengthening agent to improve the water retention and IC of SEs but also exhibited exceptional hydrogen bonding and entanglement effects, which significantly enhanced the mechanical properties of these electrolytes. Chen *et al*. produced a high-performance CNF@PVA-SPEs using CNF as a PVA reinforcing agent, and the SZABs assembled with it exhibited excellent stability and stable operation at -40 and 50 °C for 115 and 34 h (0.5 mA/cm^2) [183].

Given the composition of the material, the design of the electrolyte structure is also critical to the performance of SZABs. The construction of dual-network (DN) gels can enhance polarity, which effectively inhibits ice crystal formations. Zuo *et al*. mixed PAM with sodium alginate (SA) to produce DN hydrogel, which exhibited outstanding mechanical strength, low-temperature freeze resistance, exceptional water absorption, and high-IC (275 mS/cm) [184]. It was used for FZABs with excellent charge–discharge efficiency of >80%, a peak power of 87 mW/cm^2, fantastic reversibility, and low-temperature adaptability of -20 °C.

The conductivity of hydroxyl (OH^-) ions is a vital index to measure the performance of electrolytes [4]. Electrolytes with high hydroxide conductivity can accelerate the electrochemical reaction, thereby increasing the peak power density of SZABs. The network or porous structure inside the PEs can store or absorb conductive ions, and these conductive ions migrate in channels provided by the electrolyte, thus enabling the conduction and storage of electric charges. Subsequently, optimizing the internal structure of electrolytes is crucial for electrolyte conductivity. Recently, the introduction of various additives, the construction of DN gel electrolytes, AEMs, and the introduction of CNF reinforcing agents are crucial strategies to enhance the IC of electrolytes [185]. Recently, Liu and his team developed a novel DN structure of GPEs (PAM/SA/KI) composed of PAM, potassium iodide (KI), and SA for SZABs [112]. The IC of PAM/SA/KI hydrogel was 82 mS/cm, which exceeded that of PAM/SA (64 mS/cm) and PAM (13 mS/cm). The increase in electrolyte ion conductivity was due to the polymer network structure, H_2O molecules, and KOH, which facilitated the transport of OH^- through forming hydrogen bonds and porous structures between SA, PAM, and H_2O. Furthermore, PAM/SA/KI exhibited more microporous structures through SEM, and the existence of potassium and iodine ions was conducive to facilitating ion transport, thereby enhancing electrolyte absorption capacity. The SZAB assembled using PAM/SA/kI exhibited excellent renewability, long-cycle life of 110 h, a high-power density of 132 mW/cm^2, a good OCV of 1.43 V, and excellent stability under different extreme conditions. Considering that the loss of volatile solvent leads to the decrease of electrolyte capacity, Rase *et al*. combined PVA with a high hydroxide ion conducting polymer to prepare a 3-OH@PVA AEMs with an IC of 2.96×10^{-3} S/cm^2. The peak power density of SZABs assembled with 3-OH@PVA (158 mW/cm^2) was much higher than that of PVA (79 mW/cm^2) based ZABs due to the increase of the IC of 3-OH@PVA and the enhanced contact between electrode and electrolyte interface [186].

Additives such as cellulose, SiO_2, and LDHs reduced the crystallinity of the polymer matrix, addressing issues of poor IC and poor-H_2O absorption and water retention of the single polymer electrolyte. Lin *et al*. successfully synthesized LDH/CC/PVA SPEs by growing NiCo LDH nanowire arrays on the constituent carbon fibers of carbon cloth (referred to as LDH/CC), with PVA serving as an additive. This approach leveraged the advantages of LDHs, including reasonable hydroxy–ion conductivity, high hydrophilicity, and satisfactory alkaline resistance [187]. As the precursor concentration rose, the LDH array density, as well as the width and length of the nanowires also increased. Specifically, when the precursor concentration increased fourfold, the resulting LDH nanowire arrays exhibited widths and lengths of ~130 nm and 1 μm, respectively (Figs. 15a–c). The change in the LDH nanowire array structure led to the difference in the effective contact area between the LDH nanowire array and PVA gel, which ultimately affected the electrochemical performance of SZABs. After mixing PVA with LDH/CC, the diffraction peak intensity of PVA decreased significantly, thereby indicating that the amorphous domain of PVA increased (Fig. 15d). The presence of LDH disrupted the hydrogen bond interaction between PVA chains, resulting in the expansion of the amorphous domain. This expansion facilitated ion transport and ultimately enhanced the IC of SPEs. The IC of LDH/CC/PVA SPEs was determined and calculated through AC impedance spectroscopy. It was found that LDH significantly enhanced the IC of the electrolyte; the IC of 1.7 LDH/CC/PVA was 63.8 mS/cm, which exceeded that of pure PVA (18.1 mS/cm) (Fig. 15e). Thermogravimetric (TG) graphs of the four samples indicated that the addition of LDHs reduced the degradation temperature of PVA from 220 °C to 20 °C, thereby improving the thermal stability of the electrolyte (Fig. 15f). Furthermore, SZAB based on 1.7LDH/CC/ZAB exhibited the highest peak power density of 102.9 mW/cm^2 and demonstrated stability exceeding ~350 cycles at a current density of 5 mA/cm^2 (Figs. 15g and h). Recently, Zhong *et al*. introduced lignin as a skeleton repair agent and $ZnCl_2$ as a salt additive into PAM to prepare a porous M-DPAM-3 GPEs, and the SZABs assembled with M-DPAM-3 had an OCV of 1.4 V [188]. Theoretical calculations showed that S=O, -OH, and C=O in DMSO, AM, and lignin showed strong HB acceptability and availability, which could achieve reliable polymerization (Fig. 15i). In addition, the IC of M-DPAM-3 was 440.91 mS/cm, which was much higher than the 293.85 mS/cm of PAM (Fig. 15j). In conclusion,

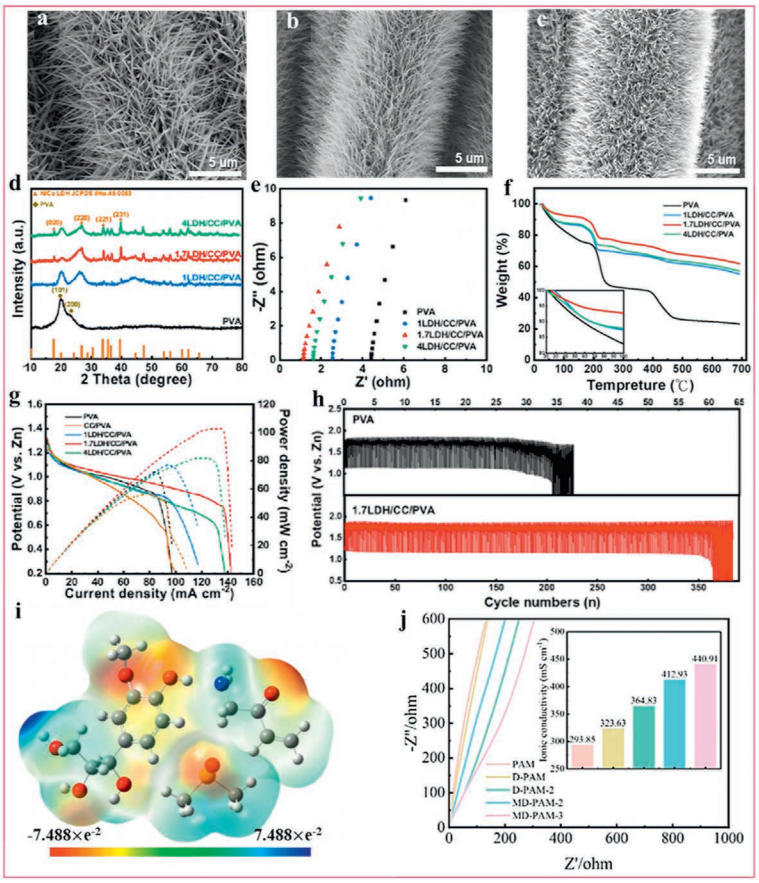


Fig. 15. SEM images at decreasing magnifications for (a) 1LDH/CC, (b) 1.7 LDH/CC, and (c) 4LDH/CC. (d) XRD pattern, (e) Nyquist plots, and (f) TG curves of PVA, 1LDH/CC/PVA, 1.7LDH/CC/PVA, and 4LDH/CC/PVA. (g) Power density curves of PVA, CCPVA, 1LDH/CC/PVA, 1.7LDH/CC/PVA, and 4LDH/CC/PVA-based FZAB. (h) Discharge–charge cycling stability tests of 1.7LDH/CC/PVA and PVA-based FZAB with a duration of 10 min per cycle at 5 mA/cm^2. Copied with permission [187]. Copyright 2024, Elsevier B.V. (i) Surface electrostatic potential of M-DPAM-3. (j) AC impedance plots and IC of electrolytes. Copied with permission [188]. Copyright 2025, Elsevier B.V.

the formation of solvated sheath structure between $ZnCl_2$ and free water molecules effectively inhibits the activity of water, thus slowing dendrite growth and zinc corrosion. In addition, lignin forms hydrogen bonds with the polymer matrix in the hydrogel network, which can improve the stability and IC of the network.

Given the low density, thermal stability, high-elastic modulus, and high-chemical resistance of polyacrylonitrile (PAN), it facilitated the manufacture of basic AEMs. Additionally, efficient ion transport channels were easily formed. Singh *et al.* synthesized two types of AEM: a comb-shaped polymer membrane (M1-nC, where $nC=(CH_2)_{n-1}CH_3$; $n=4$, 12, and 16) with poly (vinyl chloride-*co*-acrylonitrile) [P(VBC-*co*-AN)] as polymer backbone and a cross-linked polyimidazole M3 also using P(VBC-*co*-AN) [189]. Furthermore, when the M3 membrane was utilized as the SEs of SZABs, it exhibited an excellent OCV of 1.36 V under various deformation and achieved a peak power density of 165 mW/cm^2, thereby offering excellent cycle stability of 30 h. This highlighted the high stability and application potential of the M3 membrane in SZABs. In the M3 membrane, the introduction of multi-cation sites from the polymer imidazole. The cross-linking of the polymer main chain creates interlinked ion channels through hydrophobic/hydrophilic phase separation, facilitating OH^- transfer and resulting in enhanced hydroxide ion conductivity, which further enhances the IC of the electrolyte. The low IC and poor-water absorption of traditional AEMs result in a rapid drop in the performance of SZABs. Xu *et al.* constructed FCNT/ PAM-PVImBO AEMs with ultra-high-IC of 245 mS/cm through *in-situ* polymerization of a single OH^--conductive ionomer (PVImBO) in a hybrid matrix of functional carbon nanotubes (FCNTs) and PAM hydrophilic polymer (FCNT/PAM) [190]. The highly polar amide groups in PAM and PVImBO exhibited a high affinity for water molecules, thus enhancing the water absorption of the electrolyte. Furthermore, the synergistic effect of the two enhanced water retention and IC of AEMs resulting in a long-cycle life of over 350 h and an outstanding-power density of 152 mW/cm^2 for the assembled SZABs.

Given the special semi-open configuration of ZABs, the SEs progressively lose water during discharge, leading to severe volume shrinkage, decreasing mechanical properties, and decreasing IC [156]. Therefore, the H_2O retention capacity of the electrolyte determined the service life of the battery, and a feasible optimization treatment method was employed to improve the water retention capacity of the electrolyte, thereby ensuring a longer period of validity [191]. The construction of DN electrolytes and the addition of electrolyte additives limited the water loss of PE and extended the service life of ZABs. Recently, Lv *et al.* mixed PEO, PANa, *N*,*N*-dimethyl bisacrylamide, and persulfuric acid to synthesize PEO-PANa DN HPEs with excellent absorption and retention [192]. Given the presence of initiators and crosslinkers, the prepared DN structure electrolyte formed a larger water storage space, resulting in a higher adsorption capacity of PEO-PANa electrolyte to water and alkali solution compared with that of PANa. Furthermore, when PEO-PANa and PANa were exposed to air for 336 h, it was found that the PEO-PANa electrolyte retained its initial mass of 71.5 %. This excellent water retention capability of PEO-PANa enabled the assembled FSZABs to cycle for over 200 h. Despite DN GPEs enhanced electrolyte retention and extended the life of SZ-

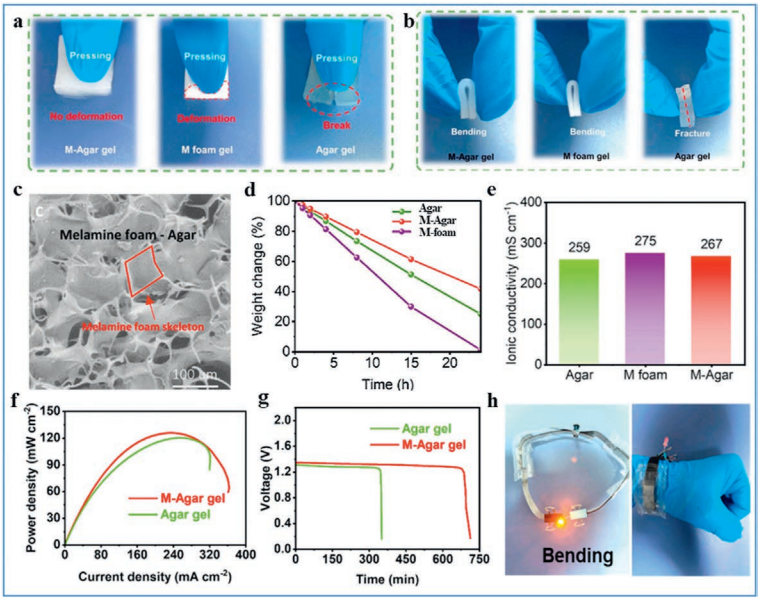


Fig. 16. (a) Destructive tests of various gels under pressure. (b) Flexibility tests of different gels. (c) SEM images of M-agar gel after freeze-drying. (d) Water retention of different electrolytes. (e) Ionic conductivities of SEs. (f) Power density curves and (g) constant discharge current curves of FZAB based on M-agar electrolyte and agar electrolyte at a 2 mA/cm^2 current density. (h) Practical application tests of FZAB under bending extrusion conditions, along with a demonstration of wearable applications of flexible batteries. Copied with permission [195]. Copyright 2022, Elsevier B.V.

ABs, GPEs relied on high concentrations of KOH, and the corrosion phenomenon inhibited its application. Thus, CNFs leveraged the advantages of excellent structural stability, abundant availability, and adjustable surface chemistry, as well as charge density but also exhibited strong hydrophilicity, thereby facilitating water absorption of SEs. Therefore, Dou *et al.* synthesized ICNF/WCNF SPEs with an excellent-water retention capacity of 15 g/g. They modified(poly(methacrylate ethyl trimethyl ammonium chloride)) (PDMC) and PAM based on water-retentive cellulose nanofibers (WCNF) and OH^--conductive cellulose nanofibers (ICNF) [193]. The assembled SZABs exhibited outstanding electrochemical property with a peak power density of 126 mW/cm^2 and a cycle life of over 310 h. Recent studies have indicated that the introduction of various additives into the polymer matrix was considered effective, thereby enhancing the water retention performance of SEs [193]. Zhang *et al.* introduced sodium sulfobutyl ether-β-cyclodextrin (Ss) additive into the interpenetrating network of poly zinc acrylate and PAM to prepare a novel PAM-PAZn-Ss solid electrolyte with excellent water retention [185]. Subsequently, Ss in the electrolyte reduced the crystallinity of the polymer fragment, serving as a penetrant, and improving the absorption of KOH solution. Thus, ZABs assembled with this electrolyte exhibited a good power density of 61.08 mW/cm^2. Its cyclic stability (47 h) at the current density of 3mA/cm^2 was over twice that of ZAB (27 h) of PAM.

The mechanical properties of SEs are crucial to the application of FSZABs [194]. Despite traditional PE possessing specific mechanical properties, their flexibility and over-mechanical properties are not ideal. The mechanical strength of PEs was enhanced by introducing additives or optimizing the internal structure of the electrolyte [185]. Zuo *et al.* introduced melamine foam skeleton into agar gel to prepare melamine-agar GPEs (M-Agar GPE) with significantly enhanced water retention, mechanical strength, flexibility, and IC [195]. In comparison with agar gel, the mechanical strength of M-Agar gel was increased by over 365.3 %, primarily because melamine foam (M foam) exhibited a 3D network structure, which offered targeted support for agar gel under external force and enhanced mechanical performance (Fig. 16a). Moreover, the M foam gel and M-Agar gel remained stable after 100 times bending, further revealing that the addition of M foam to agar gel significantly enhanced the mechanical strength and flexibility of agar gel (Fig. 16b). After freeze-drying, SEM images of M-Agar gel revealed that the agar gel exhibited a rich porous structure, thereby forming a sheet structure after dehydration. This indicated that agar gel exhibited excellent water-rich properties (Fig. 16c). Additionally, after exposing M foam, agar gel, and M-Agar gel to room temperature for 24 h, it was found that M-Agar gel retained 42 % of its initial weight. In comparison with agar gel and M foam, the water retention rate was significantly improved (Fig. 16d). The improvement in water retention rate was primarily attributable to the formation of abundant hydrogen bonds between H_2O molecules in agar gel and hydrophilic groups such as hydroxyl amine groups in agar molecules. Thus, this reduced the evaporation of water molecules. The M-Agar electrolyte exhibited a good-IC of 267 mS/cm, and the discharge area capacity of the M-Agar-based cell was 105.7 % higher compared with the agar-based battery (Fig. 16e). The SZAB assembled with the M-Agar electrolyte achieved a power density of 126 mW/cm^2 and an excellent-area capacity of 24 mAh/cm^2, thereby demonstrating stable operation under various deformation conditions (Figs. 16f–h).

Under alkaline electrolyte conditions, Zn corrosion, passivation, dendrite formation, and carbonate formation due to HER significantly reduced the stability of the battery [196]. To address these issues and facilitate large-scale applications, research on neutral, near-neutral, and weakly acidic electrolytes has become a new focus area [167,197]. Furthermore, NEs exhibited little or no tendency to react with environmental CO_2 to form carbonate substances, thereby virtually eliminating the carbonate problem. Additionally, NEs are mild and environmentally friendly, which aids in avoiding or mitigating several side reactions associated with alkaline SZABs, thereby extending battery life [198]. Tang *et al.* proposed a NE composed of a DN cross-linked PAA-Fe^{3+}-chitosan (PAA-Fe^{3+}-CS) polymer host infiltrated with NH_4Cl and $ZnCl_2$ hybrid aqueous electrolyte [199]. The absorbed near-NE exhibited high-IC. However, it was less corrosive to the electrocatalyst and Zn anode, assuring a more stable Zn-OH–O_2 chemical reaction compared with the strong alkaline electrolyte, hence exhibiting a

Table 7
Summary of some recently reported SE applications in SZABs.

	Electrolyte	Conductivity (mS/cm) (°C)	Temperature (°C)	OCV	Power density (mW/cm^2) (°C)	Ref.
SPEs	LDH-Array@PVA	55.3	r.t.	1.37	92.3	[171]
	F127-KOH	29	−20 to 20	1.32	–	[172]
	CNF@PVA	–	−60 to 50	1.46	16 (−60) 22 (−60)	[183]
	ICNF/WCNF	175	r.t.	–	126	[193]
GPEs	C20E1G5	23.94 to 68.68	−40 to 60	1.37 (−40) 1.45 (60)	443.68 (−40) 732.77 (60)	[179]
	PAM/PAA/DMSO	15.9 (−50) 74.3 (−30) 291 (60)	−50 to 60	1.52 (30)	240 (60)	[180]
	AGC-T	7.93 (−40)	−40	1.37 (−20)	21.04	[181]
	PANa-SDBS	397 (25) 231 (−40) 181 (−60)	−60	1.46 (−40)	110.7 (−40)	[182]
	PAM-SA	275	−20	1.45	87	[184]
	3_OH@PVA	2.96 (30)	r.t.	1.4	158	[186]
	LDH/CC/PVA	63.8	r.t.	0.68	102.9	[187]
	M-Agar	267	r.t.	1.46	126	[195]
	PAM-CMC-EG	94 (25) 74 (−20)	−20 to 60	1.45 (25) 1.43 (−20)	271.9 (60) 148.1 (−20)	[201]
	CA/PVA/TiO_2	1.36	r.t.	1.55	8.2	[202]
	g-C_3-N_4-PVA	27	r.t.	1.48	19	[203]
	ChCl/EG-PVA	171.3 (25) 63.8 (−40) 248.9 (50)	−40 to 50	1.35	109.3 (25) 38.2 (−40) 63.2 (50)	[204]
	PAM-PAZn-Ss	249	r.t.	–	61.08	[185]
HPEs	PEO-PANa	326	r.t.	1.37	176.4	[192]
	PCG	13	r.t.	1.39	128	[205]
	PVC-*co*-AN (M3)	54.5	r.t.	–	–	[189]
AEMs	FCNT/PAM- PVImBO	152	r.t.	2.92	152	[190]
NEs	PAA-Fe^{3+}-CS/NH_4Cl	109.8	r.t.	1.45	55.4	[199]

Note: The meanings of some abbreviated words in the table are as follows: LDH: layered double hydroxides; 3_OH: IISERP-POF13_3OH; PCG: Polyvinyl alcohol/chitosan-guar; ChCl/EG-PVA: choline chloride/ethylene glycol polyvinyl alcohol.

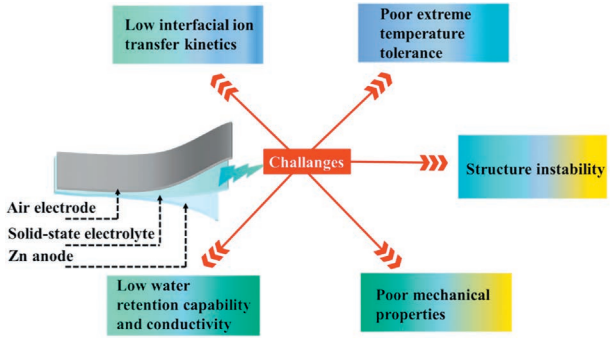


Fig. 17. Challenges of conventional solid-state electrolyte.

cycle life of ~120 h for the assembled SZABs. Additionally, other NEs such as chlorine-based NEs and $Zn(OTf)_2$ electrolyte solutes have been utilized in SZABs in recent years [168]. Several studies have shown that SZABs under neutral/near-neutral conditions exhibited higher stability compared with SZABs under alkaline conditions. However, its cycle life remained shorter compared with that of neutral/near-neutral ZAB with LEs, and its development is still in its infancy [200]. Therefore, more research is needed to determine the most appropriate electrolyte composition.

Finally, traditional SEs face challenges such as low interfacial ion transfer kinetics, poor extreme temperature resistance, structural instability, complex preparation processes, poor-mechanical properties, low IC, and high cost (Fig. 17). Table 7 presents a summary of some recently reported applications of SEs in SZABs [171–205]. In Table 7, SPEs, GPEs, HPs, AEMs, and NEs have been utilized in SZAB to enhance its peak power density, OCV, and cycle stability. While neutral or near-NEs have been shown to prevent carbonization, and corrosion, and extend battery life, such electrolytes suffer from slow ORR reaction kinetics and low concentration of H^+ reactants, resulting in higher overpotential, thereby inhibiting anode reaction. Thus, GPEs are the most widely reported type among SEs. Traditional GPEs exhibit low IC and poor-water retention, which can be alleviated by introducing various additives and constructing DN gel electrolyte. Presently, most research on SZABs has focused on the development of long-life, low cost, and remarkable-performance GPEs, while ignoring the temperature adaptability of electrolytes and the passivation resistance of Zn electrodes. Despite DMSO and other organic solvents enhancing the temperature resistance of SZABs, they possess specific toxicity, and their long-term may pose health risks. Therefore, it is necessary to explore alternative methods to enhance the temperature resistance of SZABs. In comparison with GPEs, SPE electrolytes have been less reported in studies of SZABs at extreme temperatures. However, it also exhibits excellent performance. Therefore, in the future, we should actively pursue the development of SPEs suitable for SZABs at extreme temperatures. Additionally, AEMs can be combined with GPEs to develop SEs with high-IC, excellent water retention, and low freezing point, thereby enhancing the performance of SZABs in various environments.

3. Solid-state zinc-ion batteries

The expanding consumer preference for wearable and portable electronic products has stimulated the research interest in solid-state rechargeable batteries with excellent electrochemical performance and low cost [206–208]. Among these, SZIBs, as a promising new energy storage system, exhibit a series of significant advantages such as high safety, zero electrolyte leakage, excellent flexibility, and low cost [209,210]. Despite the extensive work on ZIBs,

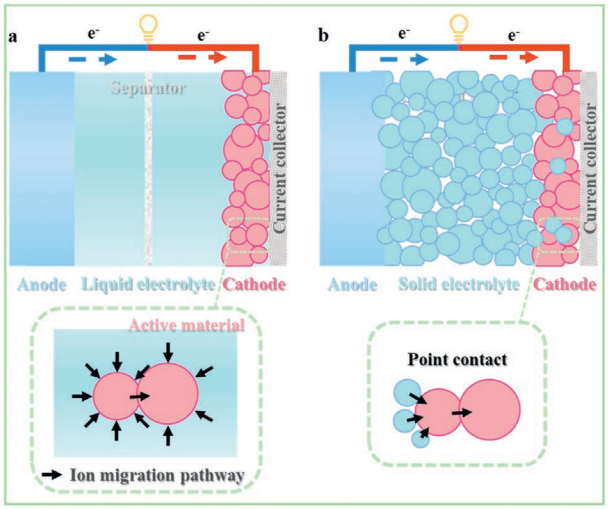


Fig. 18. Schematic illustration of the battery: (a) Aqueous ZIBs and (b) SZIBs. The electrode-electrolyte interface layer is highlighted for attention.

the progress of SZIB is still limited due to the lack of SEs with high Zn-ion conductivity. Therefore, it is essential to explore the physical and chemical properties of the appropriate SE and the Zn-ion migration mechanism inside the SE, thereby offering insights into the realization of actual SZIBs. This section summarizes the current SEs of SZIBs into three classifications: SPE, GPE, and eutectic solid electrolyte (ESE). It also discusses the mechanisms at the interface between SEs and electrodes.

3.1. Configurations and working mechanisms

Generally, traditional aqueous ZIBs are composed of four parts: anode, separator, electrolyte, and cathode material. In SZIBs, the SE serves as both an electrolyte and a separator (Fig. 18), and it is used to conduct Zn ions smoothly between the negative and positive electrodes. The SE is a key component in SZIBs, which replaces the LE in traditional liquid batteries. Furthermore, SEs exhibit excellent IC and chemical stability, which effectively transport Zn ions during charging and discharging, thereby preventing safety issues such as short circuits and leakage inside the battery [211–213]. Common SE materials include SPEs, GPEs, and ESEs.

The working principle of SZIBs is equivalent to that of aqueous ZIBs. When SZIB is discharged, the Zn metal on the surface of the anode releases electrons to produce Zn ions. Simultaneously, the cathode acquires electrons from the external circuit. When SZIB is charged, Zn ions are released into the electrolyte through the cathode. Subsequently, Zn ions close to the anode combine with electrons, which are deposited on the surface of the anode. The role of the SE is to enable the smooth conduction of Zn ions between the positive and negative electrodes [214–216]. Unlike the immersion contact between the electrode and the electrolyte in aqueous ZIBs, the contact between the electrode and the electrolyte in SZIBs is point contact. Point contact can lead to cracks and porosity at the interface, thereby restricting the transport of Zn ions at the interface. It also indicates that the contact area is relatively small, which increases the interface resistance, thereby reducing the charge and discharge efficiency and power density of the battery. At the point of contact, a chemical reaction between the SE and the electrode material is likely to occur, thereby resulting in an interfacial reaction layer. These reactive layers hinder the transport of Zn ions and reduce battery performance. Therefore, in the development of SZIBs, there are issues such as high interface resistance, limited Zn-ion transmission, and poor interface stability [217,218]. The construction of an efficient electrode/electrolyte interface structure in SZIBs, the enhancement of interface stability, and the cycling improvement present a significant challenge for the development of SZIBs. There is a need to explore the physicochemical properties of suitable SEs and the internal Zn-ion migration mechanisms, thereby offering insights into the realization of actual SZIBs. Next, we introduce SZIBs from two respects: the classification of SEs and the study of the electrode-electrolyte interface mechanism.

In summary, SZIBs adopt SE to integrate electrolyte and diaphragm functions. Although they have high IC and safety, their electrode/electrolyte interface point contact mode leads to the core problems such as small contact area, high interfacial resistance, impeded Zn^{2+} transport, and formation of side-reaction layer. Current research needs to break through the challenges of efficient interface structure design, interface stability enhancement and optimization of cycling performance, and the key lies in the in-depth understanding of the chemical and physical properties of SEs and Zn^{2+} migration mechanism, to promote the practical implementation of SZIBs.

3.2. Solid electrolytes

As a new battery technology, the choice of electrolyte in SZIB plays a crucial role in determining overall battery performance. This section explores the SEs utilized in SZIBs, focusing on SPEs, GPEs, and ESEs. This discussion aims to establish a comprehensive comprehension of the applications and characteristics of these three electrolytes in SZIBs.

3.2.1. Solid polymer electrolytes

SPEs is an electrolyte material consisting of one or more polymer matrices, salts, and other substances dissolved in it [219–221]. It exhibits the advantages of no liquid leakage, high safety, excellent mechanical properties, and processability. Ion transport in SPE relies primarily on the random motion of the polymer chains and the diffusion of ions in the polymer matrix [222–224]. In SZIB, SPE effectively isolates the negative and positive electrodes, preventing issues such as short circuits and leakage, thereby enhancing the overall safety of the battery [225,226]. Recently, researchers have developed a variety of strategies. These include *in-situ* preparation of SEs to reduce interfacial resistance, modification of SPE matrices to enhance interfacial heat conduction, and introduction of plasticizers, IL, as well as inorganic fillers to improve the performance of SPEs [227–230].

In SPE application, the *in-situ* method is often employed, which imparts a compatible electrolyte/electrode interface, significantly reducing the interface impedance, thereby resulting in high-IC [231–234]. Zhao *et al.* utilized poly EG methyl ether acrylate (PEGMEA) as a precursor monomer to construct *in-situ* polymerization of Zn^{2+} SPEs (PPM-SPEs) [235]. Furthermore, PPM-SPEs were characterized by overhanging ethylene oxide units on long side chains, which effectively facilitated the formation of disordered cross-linking and amorphous structures. The *in-situ* process imparts a compatible electrolyte/electrode interface, which results in high IC (2.87×10^{-5} S/cm) and low-interface resistance. The application of PPM-SPEs in solid-state Zn/Zn-symmetrical cells and Zn/Mo_6S_8 whole cells exhibited inhibiting dendrite growth and long-cycle stability.

The interfacial heat conduction of SPE affected the mechanical stability of the electrode-electrolyte interface under high temperatures and rapid charging conditions [236]. For normal polymer matrices, poor heat dissipation often leads to overpotential heat accumulation and local temperature overheating, thereby resulting in critical side reactions, dendrite growth, and irregular Zn deposition [237,238]. Given the Zn^{2+} transport kinetics, structural stability, and deposition uniformity, SPE suitability for SZIBs with a

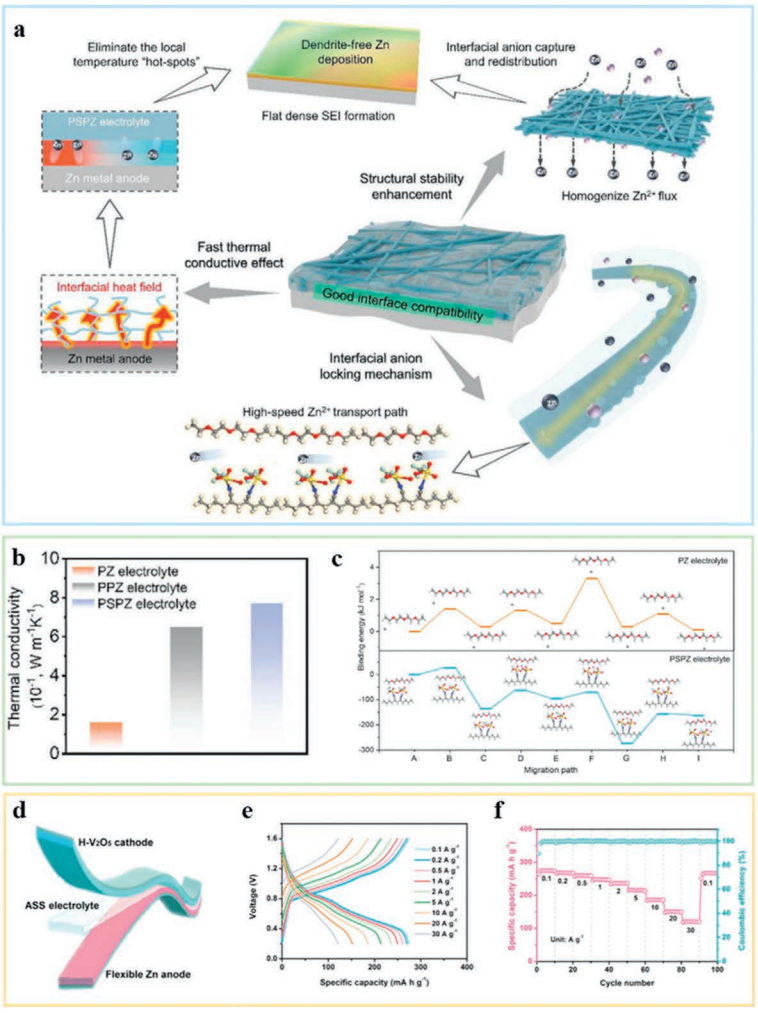


Fig. 19. (a) Schematic illustration of a multidimensional kinetics-enhanced Zn^{2+} polymer electrolyte design to enable wide-temperature SZIB performance. (b) Thermal conductivity of PZ, PPZ, PSPZ electrolyte. (c) The zinc atom's migration path and corresponding energy barrier in the PZ and PSPZ electrolyte system. Copied with permission [239]. Copyright 2023, Wiley-VCH GmbH. (d) Schematic diagram, (e) GCD profiles, (f) rate performance of the flexible Zn//H-V_2O_5 battery. Copied with permission [254]. Copyright 2023, ELSEVIER B.V. and Science Press.

wide-temperature range is crucial to ensure excellent interfacial compatibility (Fig. 19a) [239]. PEO is a crystalline, thermoplastic, water-soluble polymer, which exhibits a linear and regular spiral structure, making it an ideal candidate for the construction of SPEs [240,241]. In SZIBs, PEO formed a SE film with high-IC. However, the mechanical strength of PEO-based electrolyte membranes is relatively low, thereby exposing them to deformation or rupture under external forces. This can lead to battery short-circuiting and performance degradation, thereby reducing the cycle life and safety of the battery. Additionally, the interfacial compatibility between PEO-based SPE membranes and electrode materials was poor, thereby resulting in increased interfacial impedance. This can influence the charging and discharging performance of the SZIB, reducing its energy density and cycle stability. To enhance the performance of PEO-based SPEs, researchers have conducted a large number of modification studies. Li *et al.* designed a dense PAN/SiO_2 nanofiber membrane, which served as a multifunctional medium. It was the first time that a PAN/SiO_2/PEO/$Zn(OTf)_2$ (PSPZ) PE was proposed, which significantly enhanced multiple kinetics to unlock a wide-temperature fast charge SZIB [239]. Comparing it with the thermal diffusion coefficients of PEO/$Zn(OTf)_2$ (denoted as PZ) and PANPEO/$Zn(OTf)_2$ (denoted as PPZ) (Fig. 19b), it can be demonstrated that PSPZ had better thermal conductivity. The energy barrier of zinc atoms was significantly lower than that in the PZ system, which means that it had faster transport kinetics (Fig. 19c). Given the all-round synergistic modification of this structural bridging, a high-IC of 4.46×10^{-4} S/cm and a high Zn^{2+} migration number of 0.71 were obtained at r.t. At −25∼80 °C, PSPZ SPE still achieved stable galvanizing/stripping reaction. A pouch solid-state Zn-VO_2 cell with a wide-temperature, durable, and high rate PSPZ-based PE was constructed, and the LED indicator was successfully illuminated at high temperatures.

The introduction of plasticizers was counted an effective measure to enhance the electrochemical efficiency of SPE by promoting a greater ratio of non-crystalline regions in the polymer, thereby increasing the IC [242,243]. The succinonitrile (SN) is an organic nonionic plastic material whose high polarity is due to the strong polar group (-CN), which dissolves various salts to form *An spe*. Furthermore, SN can be used as an additive to significantly enhance the IC of SPE [244,245]. Zhang *et al.* used poly ethylene carbonate (PEC) as the polymer matrix and SN as the plasticizer. Simultaneously, to guarantee that the SPE exhibits adequate mechanical strength and avoids short-circuiting, a supporting glass fiber was added to enhance the mechanical properties of the SPE, thereby enabling effective separation of the positive and negative electrodes [246]. They prepared PEs directly *in-situ* between the electrodes, thereby enhancing the interfacial contact between the electrolyte and the electrodes. The results indicated that the

in-situ method obviously reduced the interfacial impedance compared with the traditional cell assembly process, which was one-tenth that of the *ex-situ* SPE. The IC of SPE with the addition of the optimal component (30 % SN) was 5.183×10^{-5} S/cm and the ion transport number was 0.61 at r.t. The Zn/PEC@GF-30 %SN/Zn-symmetric battery was assembled and its ratio performance was tested at r.t. Particularly, the stable and ultra-long cycling performance of 1950 h was achieved at 0.1 mA/cm^2, thereby indicating that the electrolyte inhibited hydrogen evolution generated using Zn dendrites and Zn foil. The specific discharge capacity of the integrated SZIB with manganese dioxide (MnO_2) as the cathode was 123.8 mAh/g at 0.1 A/g at r.t. However, its cycling performance was poor, indicating a poor cement/solid contact at the cathode-SPE interface, inhibiting the ion transport, and thereby requiring enhancement.

Additionally, ILs are composed entirely of cations and anions, which are currently counted one of the hopeful candidates for liquid solvents in batteries. Its wide electrochemical stability window and high-IC offer advantages, including non-flammability, low volatility, and high thermal as well as chemical stability [247–249]. The introduction of ILs is also a viable way to enhance the performance of SPEs. The design of SPEs with ILs exhibits significant advantages, as ILs added to the polymer framework served as plasticizers for polymers, thereby enhancing the flexibility and conductivity of the chain [250,251]. Therefore, SPEs prepared with ILs exhibited flexible amorphous properties, thereby facilitating high cation and minimal anion migrations. Puttaswamy *et al*. developed a flexible and highly Zn^{2+} conductive PVA-PEG interpenetrating polymer network (PVA-inter-PEG), which contained 1-ethyl-3-methylimidazolium trifluoromethanesulfonate (EMIM OTf)-based IL *A. spe* for SZIB [252]. The proposed PVA-inter-$PEG_{30\%}/IL_{70\%}$ SPE exhibited a high IC (2.264 mS/cm), a low glass transition temperature ($T_g = -10.2$ °C), high zinc oxidation stability (~2.8 V), and exceptional thermal stability (>200 °C). Furthermore, PVA-inter-$PEG_{30\%}/IL_{70\%}$ SPE exhibited stable interfacial contact with the Zn anode, which was cycled at 0.2 mA/cm^2 for 3000 h, thereby achieving dendrite-free Zn stripping/plating. The solid-state $Zn/V_{10}O_{24}$ nH_2O cells prepared using PVA-inter-$PEG_{30\%}/IL_{70\%}$ SPE exhibited a discharge capacity of ~325 mAh/g at 0.1 A/g with excellent performance rate and cycling stability. Additionally, PVA-inter-$PEG_{30\%}/IL_{70\%}$ SPE is utilized in the manufacturing of flexible bag battery prototypes, which exhibit excellent safety performance and serve as a reliable and promising energy storage device for wearable applications. Ma *et al*. developed the first 1-ethyl-3-methylimidazole tetrafluoroborate (EMIM-BF_4) IL, developing a 28.6 μm thick thin film SPE, and using PEO/poly(vinylidene fluoride-hexafluoropropylene) (PVDF-HFP) as the matrix for the construction of SZIBs [253]. Subsequently, SZIBs exhibited superlative cycling performance, with 30,000 cycles at 2 A/g at r.t. The SZIB exhibited a wide-temperature window (−20~−70 °C) and was capable of 100 cycles at bending deformations of ~150° Given this electrolyte, Qiu *et al*. developed a SZIB with modulated V_2O_5 (h-V_2O_5) serving as the cathode [254], which was composed of a flexible Zn NS anode, SPE, and flexible h-V_2O_5 cathode (Fig. 19d). When using SPE, the h-V_2O_5 NW cathode sustained the advantageous Zn^{2+} intercalation/deintercalation features, owing to its GCD curves (Fig. 19e). At 30.0 A/g, this flexible Zn//h-V_2O_5 cell maintained a satisfactory capacity of 121.9 mAh/g (Fig. 19f). The flexible Zn//h-V_2O_5 cell exhibited superior cycle stability with 84 % retention and a capacity of ~164.2 mAh/g at 10.0 A/g for 5000 cycles. Significantly, the assembled flexible SZIB operated over a wide-temperature range (−20~70 °C).

Inorganic fillers play a pivotal role in enhancing the conductivity of SPE. The introduction of inorganic fillers not only reduced the crystallinity of SPE, ensuring easy Zn-ion migrations but also forming an additional Zn-ion transport path, thereby offering a fast channel for Zn-ion migration. Additionally, there is an interaction between the functional groups on the surface of the inorganic filler and the cations or anions in the Zn salts, which facilitates the dissociation of Zn salts, thereby increasing the number of free Zn^{2+}. The increase of free Zn ions enhanced the ion concentration and ionic conductivity in SPE [255]. As an emerging 2D material, MXene exhibits excellent electrical conductivity and chemical stability. The functional groups on its surface can interact with ions in the Zn salt, thereby facilitating Zn salt dissociation and Zn-ion migrations. Similarly, the homogeneous dispersion of MXene NSs in SPE developed continuous ion transport channels, thereby enhancing conductivity [256,257]. Chen *et al*. achieved the first SPE based on polyvinylidene fluoride-*co*-hexafluoropropylene filled with methyl polyacrylate grafted MXenes (labeled PVHF/MXene-*g*-PMA) through chemical grafting [258]. The interaction between the highly grafted PMA and PVHF substrates resulted in uniform dispersion of MXenes. The ionic conductivity of the resulting SPE was three orders of magnitude higher compared with the PVHF matrix, which reached 2.69×10^{-4} S/cm at r.t. Dendritic galvanizing/stripping with high reversibility exceeded 1000 h at r.t. and 200 h at high temperature. The SZIB demonstrated exceptional cycle performance at r.t., cycling 10,000 times at 2 C, and operating normally in a temperature range of −35~100 °C. Thus, SZIBs exhibited a shelf life of more than 90 days after cryo/high-temperature storage. Feng *et al*. prepared pH/MXene SPE by mixing representative $Ti_3C_2T_x$ MXene with PVDF-HFP and applied it to SZIB [259]. The IC and ion transfer number of the designed SPE reached 4.52×10^{-4} S/cm and 0.435, owing to the formation of the MXene-polymer hydrogen bond network, respectively. Moreover, the plating/stripping times were 2500 h at 0.1 mA/cm^2 and 1500 h at 0.5 mA/cm^2. Given these practical applications, it was observed that the use of pH/MXene SPE significantly enhanced the cycle stability and rate performance of the assembled solid-state Zn/VO_2 cells. Additionally, according to the advanced solvent-free MXene plasticized SPE, SZIBs offered excellent durability, high safety, and long cycle life, thereby significantly eliminating several adverse effects of SZIBs.

In conclusion, recent studies have optimized the performance of SPEs through *in-situ* preparation, introduction of plasticizers, ILs, and inorganic fillers to effectively reduce interfacial impedance and enhance IC. However, how to balance the synergistic effect of each component, ensure the long-term interfacial stability, and achieve large-scale preparation are still challenges, and further exploration of the optimization of the material system and interfacial regulation mechanism is needed to promote practical applications.

3.2.2. Gel polymer electrolytes

A GPE is a 3D network structure formed by hydrophilic polymers in water through physical entanglement, electrostatic interactions, or chemical cross-linking [260]. It combines the stability of a SE with the ionic conductivity of a LE, thereby exhibiting high ion mobility and excellent mechanical flexibility. The hydrophilic polymer groups in the GPE can bind to water molecules to form a stable hydration layer, which further facilitates ion transport. In SZIBs, GPE can effectually inhibit the growth of Zn dendrites and hydrogen evolution reactions, thereby improving the stability of Zn anodes. However, GPE still faces some challenges in practical applications, including narrow electrochemical stability window, low mechanical strength, and poor interface stability with electrode materials [261]. To address these challenges, researchers have continuously optimized the formulation and preparation of GPE to improve its overall performance. For instance, the mechanical strength of GPE was enhanced by introducing crosslinkers and reinforcing agents. The electrochemical stabilization window and interfacial stability of polymer chains were enhanced by optimizing their structure and functional groups [262–264]. This section

introduces the application of GPEs in SZIBs from the perspective of SE matrices.

PVA is widely utilized due to its economic, non-toxic, and self-healing properties, which are attributable to its numerous hydroxyl groups. PVA-based GPE is formed using PVA as the matrix and incorporating a specific amount of additives (such as lithium salts, siloxanes, silicon dioxide, and more) to create GPE [265]. This electrolyte incorporates the excellent mechanical properties of PVA with additive conductivities, thereby offering broad application potential in electrochemical devices [266]. The IC of PVA-based GPE depends primarily on the interaction between the added additives and the PVA matrix. Furthermore, upon optimizing the type and proportion of additives, the ion mobility rate and ionic conductivity of PVA-based GPE can be significantly enhanced. Li *et al.* prepared polyzwitterionic hydrogel electrolyte (ZIS–PVA) using PVA and polyzwitterionic salts (poly-ZIS), which originated from the robust electrostatic interaction between polyzwitterionic ions and counter ions, thereby regulating the transport of anions and cations [267]. Subsequently, by adjusting the polyzwitterion ion contents in the hydrogel network, the conductivity and mechanical properties of the hydrogel were optimized. The intrinsic anion/cation transport channel manipulation resulted in a uniform plating/stripping behavior of the Zn metal anode. These synergistic effects provided excellent electrochemical performance for Zn/ZIS–PVA/polyaniline (PANI) cells, which reached a capacity of 102.5 mAh/g and a retention rate of ~87.5 % after 600 cycles at 5 A/g. Liu *et al.* reported the preparation of PVA-$Zn(CF_3SO_3)_2$–3 % TiO_2 (PZ3T) GPE using PVA as the matrix and $Ti_3C_2T_x$−MXene as the additive [268]. Furthermore, PZ3T exhibited excellent mechanical properties, high-IC (1.243×10^{-5} S/cm), and satisfactory self-healing ability, which effectively inhibited the growth of Zn dendrites, thereby achieving highly stable Zn plating/stripping of over 3000 h at 0.5 mA/cm^2. The full Zn/PVA-$Zn(CF_3SO_3)_2$–3 % TiO_2/V_2O_5 battery exhibits a high capacity of ~216 mAh/g after 115 cycles and excellent cycling performance. Xiao *et al.* used graphene oxide (GO) embedded PVA to prepare hydrogel electrolytes (GPHEs), which exhibited exceptional Young's modulus of 530 kPa, high-IC of 21 mS/cm, high tensile properties of ~230 % strain breakdown, and the self-healing ability of gel electrolytes [269]. This electrolyte was used in zinc/manganese dioxide fiber batteries to maintain 98.0 % capacity over 1000 cycles. However, the electrolyte utilized a hydrogel of water molecules nested in polymer chains, and water inevitably freezes at sub-zero levels, thereby adversely affecting its practical application in specific cold environments. To solve this challenge, Wang *et al.* utilized a GPE composed of EG and GO in zinc/manganese dioxide fiber batteries [270]. The SZIB exhibited a high stripping/galvanizing efficiency at very low temperatures, a high-energy density of 0.1752 mWh/cm, and a high-power density of 1.25 mW/cm were obtained. Additionally, capacity retention was as high as 91 % after 2000 continuous bending cycles. The discharge capacity exceeded 22 % even at low temperatures of −20 °C.

Furthermore, PAM is a polymer compound, which exhibits excellent physical and chemical properties, thereby resulting in exceptional water absorption and retention [271,272]. The PAM-based GPE was formed with a specific ion-conducting capacity by adding appropriate electrolyte salts and other additives. This electrolyte is capable of transporting ions in a solid state, providing the required ion channels for electrochemical devices such as batteries. Subsequently, PAM-based GPE has been widely utilized in flexible ZIBs due to their excellent interface compatibility. However, they exhibit disadvantages such as low mechanical strength and low ionic conductivity. Next, recent advances in enhancing PAM-based GPE performance in SZIBs are discussed, including methods such as improving PAM stability and dispersion using LDH, thereby leveraging the synergistic effect between cellulose and PAM to create superior performance composites.

Furthermore, PAM is prone to degradation during use, leading to a decrease in its performance. The addition of LDHs decreases the degradation rate of PAM to a considerable extent. The LDH adsorption effects can reduce the contact between PAM and degradable substances. Thus, the catalytic property of LDHs facilitated the stabilization reaction of the PAM molecular structure, thereby decreasing its degradation process. Kimilita *et al.* constructed SZIBs using LDH hybrid (PAM-LDH) electrolytes [273]. Experimental data indicated that the addition of LDH to PAM enhanced ionic conductivity while maintaining its mechanical properties. The PAM-LDH electrolyte, which is bound to NH_4F-treated MnO_2, exhibited a high capacity of 354.3 mAh/g at 0.1 A/g. It also exhibited an energy density of 484.3 Wh/kg (based on cathode weight) at a peak power density of 136 W/kg.

Cellulose and PAM exhibit synergistic effects under specific conditions. For example, cellulose-based polymer electrolytes with excellent strength and IC have been prepared by introducing zinc salts for cellulose chain expansion. The synergistic effect further enhanced the overall performance of the composite material, resulting in strength, toughness, and water resistance, thereby expanding its application range and enhancing its effectiveness. Zhang *et al.* developed a dual network solid-state polymer electrolyte (CPZ) based on oxidized bacterial cellulose (TBC) and polyacrylamide (PAM) [274]. The strong hydrogen bonding network of cellulose was disrupted by the coordination of zinc ions with cellulose hydroxyl groups, which enlarged the chain spacing and facilitated the Zn^{2+} transport, while the mechanical properties were enhanced by using the dual-network structure (cellulose + PAM). By introducing $ZnCl_2$ and $Zn(BF_4)_2$ to regulate the bound water content and inhibit the free water activity, hydrogen precipitation reaction and anodic corrosion were reduced. By optimizing the ratio of $ZnCl_2$ and $Zn(BF_4)_2$, the CPZ-2 electrolyte exhibited higher IC (38.26 mS/cm), mechanical properties (tensile stress of 592 kPa, tensile strain of 381 %), and electrochemical window (2.58 V) than the other ratios. In symmetric cell testing, CPZ-2 achieved 980 h of stable cycling at 0.5 mA/cm^2. In full-cell testing, it was able to deliver a specific capacity of 363.1 mAh/g at 0.1 A/g and maintained a capacity of 73.2 mAh/g after 100 cycles, with long-term stability to be enhanced. This study successfully developed a high-performance cellulose-based SE through an innovative chain extension effect and dual-network design, which provides a new idea for the practicalization of zinc-metal batteries. However, its scale-up production, high current performance and long-term stability still need to be further optimized, and the environmental friendliness needs to be comprehensively evaluated.

The presence of cellulose enhanced PAM dispersion in water and other solvents. The reticular or fibrous morphology of the cellulose may provide more attachment points and dispersion space, thereby facilitating the uniform dispersion of PAM molecules in solution. Li *et al.* developed a lignin-containing cellulose nanofiber (LCNF)-PAM hydrogel electrolyte with a unique DN structure and excellent water retention for high-energy SZIBs [275]. Given these advantages, the restricted mobility of water molecules in LCNF-PAM hydrogel (LPH) was limited, and the suppressed water-induced side reactions were restrained, which resulted in a significantly wider voltage window. Assembled with an LPH electrolyte, Zn/Zn-symmetrical cells maintained a long-cycle life of 4000 h at 0.5 mA/cm^2@1 mAh/cm^2. After 4000 cycles at 5 A/g using LPH electrolyte, the capacity of the entire Zn/MgVO cell reached 149.2 mAh/g, and the capacity retention rate was 91.9 %. Additionally, when the voltage window expanded within the range of 0.2–1.9 V, the full battery with LPH exhibited a power density of 341.7 W/kg and a high-energy density of 255.4 Wh/kg with a cycle life exceeding 5000 cycles. The design of this LPH electrolyte offers a novel approach for the further development of SZIB, stabilizing the Zn anode, and achieving high-energy density.

Polar groups on the PAM molecular chain were adsorbed on the cellulose surface, thereby forming a bridging structure between fibers through physical or chemical action. This adsorption and bridging effect linked the fibers more closely, enhancing the overall strength and stability of the fiber material. Meanwhile, the flocculation effect of PAM facilitated the cohesion and settlement between the fibers and enhanced the treatment effect of fiber materials. These mechanisms collectively make cellulose a key additive for enhancing the performance of PAM. Tu *et al.* developed a functionalized, nano-engineered Zn^{2+}-coordinated carboxylate cellulose SE for SZIBs, which is denoted as Zn-CCNF@XG [276]. Except for the different oxidation steps, the preparation process was similar to that of Zn^{2+} coordinated cellulose nanofibril electrolytes (denoted as Zn-CNF@XG). The SZIB exhibited a high-IC of 1.17×10^{-4} S/cm at r.t., a wide electrochemical stability window of ~2.88 V, a high Zn^{2+} transfer number of 0.78, and an excellent mechanical resistance of 60 MPa. The introduction of −COOH significantly reduced the dissociation energy of Zn ions, which coordinated with oxygen-containing functional groups, and −COOH as well as −OH combined, thereby forming a rapid conduction channel of Zn ions. This was attributable to the superior and satisfactory conductivity of Zn ions. The LSV and the overpotentials of the two materials were calculated as 2.88 V and 2.07 V, respectively (Fig. 20a). These values meet the requirements for the stable and safe operation of SZIBs, which highlighted that cellulose-based SEs enhanced electrochemical efficiency through functionalization and nanoengineering strategies. The Zn/Cu asymmetric battery based on Zn-CCNF@XG exhibited a lower oxidation voltage of 0.15 V, compared with 0.20 V for the battery based on CNF@XG (Fig. 20b). Dissociation energies of Zn^{2+} de-coordinating showed that -COOH can significantly reduce the dissociation energies (Figs. 20c-e), indicating that the ionic jump of Zn^{2+} in Zn-CCNF@XG was more direct than that in Zn-CNF@XG, which was the reason why Zn-CCNF@XG has higher IC and lower activation energy. Therefore, Zn anodes containing Zn-CCNF@XG exhibited a more favorable oxidation voltage, which enhanced the performance. After 1000 cycles, the Coulombic efficiency (CE) retention rate was 99.51 % in Zn/Cu asymmetric cells, while the overpotential in the Zn/Zn symmetric cell increased ~40 mV after 1800 cycles (3600 h). The results indicated that the Zn-CCNF@XG-based SZIB exhibited stable cycle life and excellent rate performance, with a capacity retention rate of 83.46 % after 3000 cycles at 1 A/g.

In summary, GPE can enhance the mechanical strength, IC and interfacial stability of SZIB and inhibit the growth of zinc dendrites by optimizing the matrix materials (*e.g.*, PVA, PAM) and introducing additives such as cross-linking agents, LDH and cellulose. However, GPE still faces challenges such as narrow electrochemical window, insufficient mechanical properties, material degradation in long-term cycling, and interfacial side reactions, and further exploration of additive synergistic mechanism and scale-up preparation process is needed to achieve a balance between high stability and practical performance.

3.2.3. Eutectic solid electrolytes

Despite significant efforts to improve the performance of SEs in the directions of SPEs and GPEs, further enhancement of IC remains challenging due to the inherent C–C covalent bond characteristics in the carbon chains. To achieve both high-IC and excellent interface compatibility, it is essential to consider fundamental innovations and breakthroughs in the field of SEs, thereby exploring novel ion transport mechanisms [277]. Given this understanding, researchers have introduced the concept of eutectic electrolytes. In comparison to traditional LEs, eutectic electrolytes are mixtures composed of at least two components, each with a higher melting point individually than when combined. As analogs of ILs, eutectic electrolytes exhibit numerous notable characteristics, including low vapor pressure, excellent thermal stability, a wide electrochemical potential window, and high tunability. Eutectic electrolytes can be categorized into liquid eutectic electrolytes, non-aqueous eutectic electrolytes and ESEs according to the composition and state of the components. Notably, ESEs possess other significant advantages compared with traditional electrolytes, such as simplified preparation processes, cost-effectiveness, and non-toxic eutectic systems. The physicochemical properties of ESEs, including melting point, viscosity, surface tension, and ionic conductivity, correlated with the intermolecular interactions within them. Furthermore, ESEs can only form successfully when the intermolecular forces between the different components in the mixture exceed the original intramolecular forces within each component. Hong *et al.* proposed a solid-state ion conductor known as "hydrogen-bonded ionic eutectic" (HIC) [278]. Zinc perchlorate hexahydrate ($Zn(ClO_4)_2 \cdot 6H_2O$) and imidazole (IMI) served as raw materials, with a molar ratio of 1:x ($x = 1, 2, 3, 4$). Thus, HIC was prepared through mixing at r.t., denoted as Zn-IMI_{1-x}. After mixing, the mixture first appeared as a transparent solution, which underwent nucleation and crystallization, thereby forming a white solid. The HICs ($ZnIMI_{1-x}$, $x = 1, 2, 3$) exhibited high-IC of 16.6–11.3 mS/cm at r.t. (Fig. 20f). At a low temperature of −40 °C, Zn-IMI_{1-3} maintained a high-IC of 2.78 mS/cm (Fig. 20g). In HICs, two mechanisms coexist to achieve high-IC: (1) Anion vacancies on their crystal surfaces facilitate the dissociation of metal salts to produce a large number of free cations; (2) Their flexible hydrogen-bonded framework facilitates ion transport. Additionally, the crystalline water from the hydrated metal salt coordinated directionally with divalent metal cations, thereby weakening the charge density of the ions, lubricating the metal ions, and achieving unprecedented ionic conductivity at both room and low temperatures. Furthermore, when HIC served as an electrolyte and a COF with triquinoxalinylene and benzoquinone units (TQBQ-COF) served as the cathode, a Zn/TQBQ-COF full battery was prepared (Fig. 20h). The cyclic voltammetry (CV) curves revealed the high reversibility of the TQBQ-COF redox reaction (Fig. 20i). At 25 °C and 5.0 A/g, the full battery delivered an initial capacity of 186.8 mAh/g and retained a capacity of 87.1 mAh/g after 8000 cycles. At a low temperature of −20 °C, after 1500 cycles, its capacity reached 106.0 mAh/g, with a retention rate of ~70.9 % (Fig. 20j). The successful application of HIC in full batteries demonstrates its outstanding electrochemical performance.

ESEs can be categorized into two types, one is the addition of inorganic materials to conventional eutectic electrolytes to form ESEs. Meng *et al.* prepared a solid Zn-coordinated electrolyte (ZCE) with high Zn-ion conductivity at r.t., utilizing MXene as a nucleation additive, and solidifying a deep eutectic solvent [279]. They stacked and assembled a V_2O_5 cathode, ZCE, and Zn anode using a cold-pressing method to form an open-structured SZIB. The 2D MXene effectively facilitated Zn-ion migration along the parallel direction of MXene, thereby enhancing the IC of the ESE and achieving efficient Zn-ion transport. Furthermore, the abundant Lewis acid centers on MXene exhibited strong interactions with OTF^- anions, which established more interfacial ion conduction pathways, thereby increasing the ionic conductivity of ZCEs to 6.69×10^{-4} S/cm. The ZCE was electrochemically compatible with the Zn anode, which underwent over 2500 reversible Zn plating/stripping reactions. The solid-state Zn/V_2O_5 battery achieved a specific capacity of 144 mAh/g with a CE of 99 %, thereby validating the practical applicability of ZCEs. The second is the confinement of the eutectic electrolyte space to nano-channels such as MOFs, or the combination of eutectic electrolytes with highly polar polymer matrices thereby forming ESEs. Mao *et al.* synthesized DEE@PCN-222 by confining the eutectic electrolyte in the nano-channels of a metal-organic skeleton (PCN-222) [280], which formed a stable internal zinc ion transport channel (Figs. 21a-c). In DEE, solvated Zn^{2+} was surrounded by SN and TFSI. This strong binding would

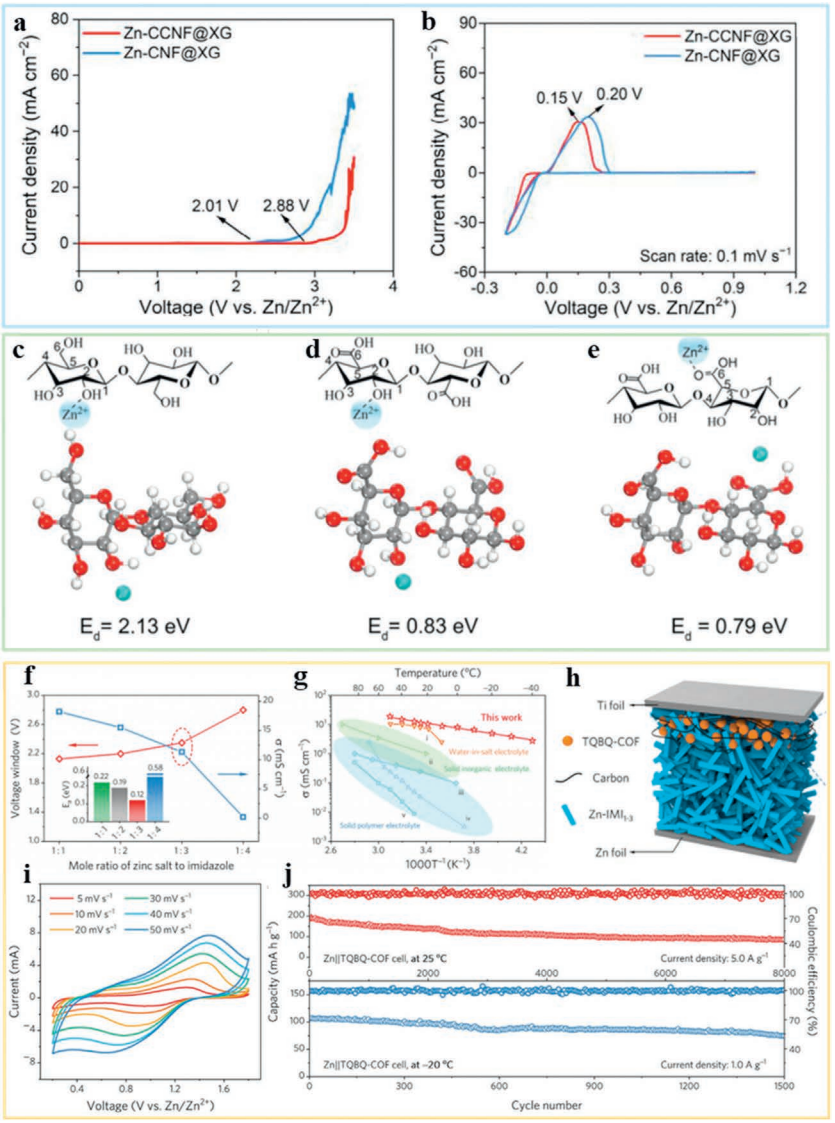


Fig. 20. (a) Electrochemical stability windows of Zn-CNF@XG and Zn-CCNF@XG. (b) CV curves of Zn plating–stripping of Zn-CNF@XG and Zn-CCNF@XG-based coin battery at a scan rate of 0.1 mV/s. Dissociation energies of Zn^{2+} de-coordinating with (c) −OH located on C_2 of CNF, (d) −OH located on C_2 of CCNF and (e) −COOH of CCNF. Copied with permission [276]. Copyright 2024, Wiley-VCH GmbH. (f) Voltage window and conductivity of the HICs (the mole ratio of Zn perchlorate hydrated and imidazole are 1:1, 1:2, 1:3, and 1:4, respectively). (g) IC of Zn-IMI_{1-3} compared with other representative electrolytes at different temperatures. (h) Schematic illustration of the solid-state ZIBs with the HIC (Zn-IMI_{1-3}) electrolyte. (i) CV curves of TQBQ-COF in different scan rates from 5 mV/s to 50 mV/s. (j) Cycling performance and corresponding CE at a current density of 5.0 and 1.0 A/g at various temperatures. Copied with permission [278]. Copyright 2024, Wiley-VCH GmbH.

impede the movement of Zn^{2+} through the electrolyte and lead to slow ionic conductance. In contrast, the migration of Zn^{2+} in PCN-222 pores was significantly accelerated due to electrostatic interactions between Zn^{2+} and oxygen-containing functional groups in PCN-222, which could act as migration sites. However, due to the distance between the sites, Zn^{2+} still needed to overcome a certain energy barrier during the migration process. After encapsulating the DEE in the pores of PCN-222, the number of Zn^{2+} migration sites increased and the distance between neighboring sites was shortened, which contributed to the formation of convenient Zn^{2+} transport channels inside the DEE@PCN-222. In contrast, the DEE composed of TFSI and SN was confined to the pores of PCN-222 due to its large size. The ion-transport network of DEE@PCN-222 achieved efficient Zn^{2+} conductivity. The IC at room temperature was 3.13×10^{-4} S/cm, the activation energy was 0.12 eV, and the Zn^{2+} migration number was 0.74. Reversible Zn coating/peeling was obtained for 2476 h due to the enhanced electrochemical compatibility to the Zn anode and reduced interfacial resistance. To demonstrate the utility of the developed DEE@PCN-222, full cells were assembled to systematically study the electrochemical performance (Fig. 21d). Performance tests were evaluated at different current rates (Fig. 21e). The cell of DEE@PCN-222 showed better rate performance among the three cells, providing a higher specific capacity of 140 mAh/g even at high current densities. The use of eutectic gels as electrodes and electrolyte substances for flexible stretchable battery applications has also been realized, which simultaneously achieves full battery autonomous self-healing capability. Li *et al.* used UV *in-situ* polymerization to immobilize a high concentration of $ZnCl_2$ low eutectic solvent in a PAM matrix [281], and prepared a self-healing and stretchable ESE membrane (DA-ETG), which had a maximal fracture strength of 0.6 MPa and IC of 6.4×10^{-4} S/cm. DA-ETG increased the electrode-electrolyte interfacial area contact in the SZIB assembly, reduced the ion transport distance between the electrodes and the electrolyte, minimized the internal resistance of the battery, and enhanced the long-term cycling stability of the battery. Using DA-ETG, this zinc ion battery

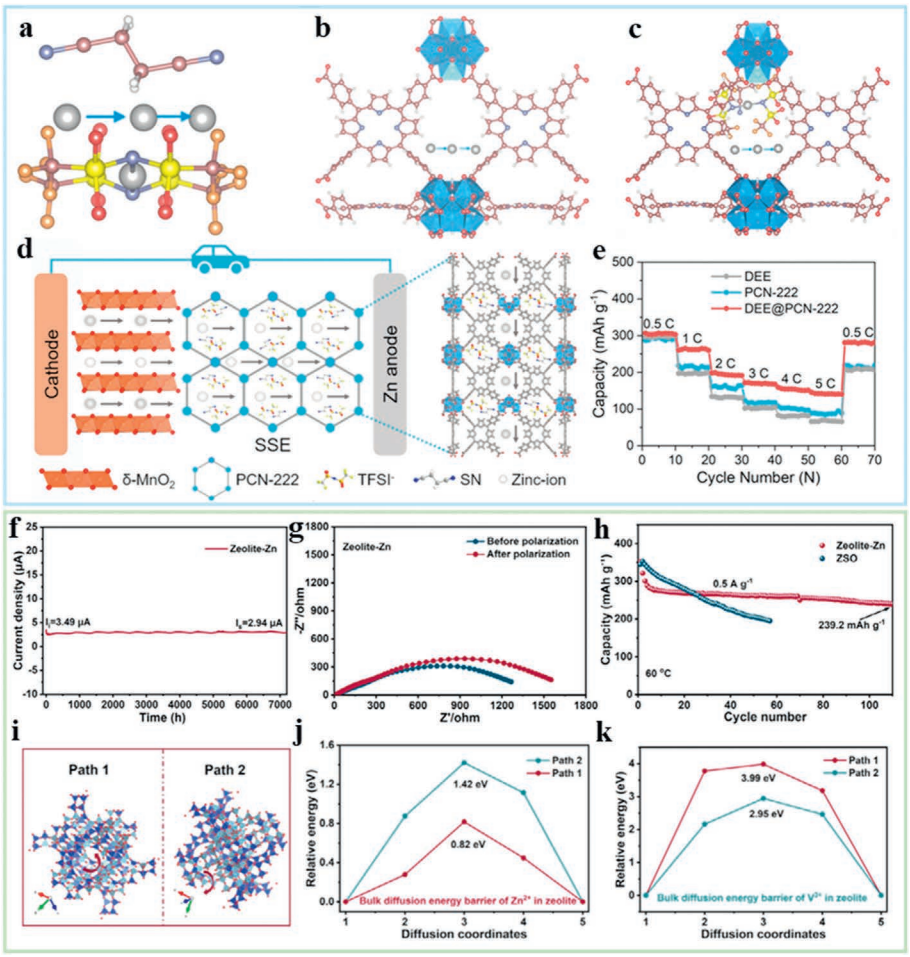


Fig. 21. First-principles calculations of the optimum Zn^{2+} migration pathway in (a) DEE, (b) PCN-222, and (c) DEE@PCN-222. (d) Schematic diagram of the designed battery using DEE@PCN-222. (e) Rate performances of Zn||MnO_2 full batteries. Copied with permission [280]. Copyright 2024, Wiley-VCH GmbH. (f) Current-time curves of Zn||Zeolite-Zn||Zn cells. (g) Intrinsic impedance of Zeolite-Zn electrolyte tested by stainless-steel sheet symmetric cells. (h) Performance comparison at high temperature of 60 °C of Zn//$NH_4V_4O_{10}$ cells in Zeolite-Zn and ZSO electrolytes. (i) Bulk diffusion paths of zinc/vanadium ions in the crystalline structure of zeolite and the calculated bulk diffusion energy barriers for (j) Zn^{2+} and (k) V^{3+} ions. Copied with permission [282]. Copyright 2025, Wiley-VCH GmbH.

achieved a high capacity of 580 mAh/g at 0.1 A/g and maintained a capacity of 234 mAh/g even at 5 A/g. The excellent cycling stability was demonstrated by the ability to maintain 85 % capacity after 2000 cycles at 2 A/g, with a cycling efficiency of nearly 98 %. In addition, the DA-ETG electrolyte based ZIB operates when subjected to twisting or folding, maintaining 86 % capacity retention after 300 cycles at 2 A/g and an ambient temperature of −20 °C. The DA-ETG electrolyte based ZIB represents a zinc-ion energy storage device with excellent flexibility and low temperature resilience. The innovative approach used to fabricate the eutectic gel electrolyte provides a viable strategy to address issues such as Zn dendrite growth and enhanced cycling performance of zinc ion energy storage devices.

In summary, ESE breaks through the C–C bond ion transport limitation of traditional SPE/GPE through multi-component synergistic action, and exhibits the advantages of high IC, wide electrochemical window and environmental friendliness. Despite some significant progress has been made in ESEs, it remains open for further research. Future research on ESEs should focus on exploring suitable materials, elucidating their coordination geometry and formation mechanisms, optimizing their physicochemical properties, and enhancing the activity and stability of the redox reactions.

Solid-state inorganic electrolytes (SIE) are usually formed from inorganic polycrystals, where the bulk crystals are significantly different from the grain boundaries in terms of structure and composition. Ion transport in SIE relies mainly on the hopping of mobile ions between vacant or interstitial atoms in the bulk crystals. However, grain boundaries typically have poor physical interfacial contacts, which leads to considerable ion transport resistance and uncontrollable dendrite growth through SIE cracks. Zeolite, as a low-cost porous material with regular pore size and shape, has an aluminum-oxygen tetrahedral structure, which provides the vacancies required for ionic conduction and thus facilitates smooth ion transport. Benefiting from the robust structure of silica-oxygen tetrahedra, the zeolite solid electrolyte has high thermal and chemical stability with high IC. Li *et al.* prepared a low-cost zeolite-zinc electrolyte and used it in the study of aqueous ZIBs [282]. This zeolite-zinc electrolyte had good electrochemical stability, low migration barrier for zinc ions and inhibition of vanadium dissolution, and the electrochemical window of Zeolite-Zn was widened and hydrogen precipitation was effectively suppressed compared with 2 mol/L $ZnSO_4$ (ZSO). The zinc ion mobility number of 0.866 was calculated from current-time curves (Fig. 21f) and Nyquist plots before and after the initial activation process. This contributes to the fast zinc ion transport behavior in the Zeolite-Zn electrolyte. The IC calculated from the impedance of the stainless steel symmetric cell assembled from Zeolite-Zn (Fig. 21g) was calculated to be 2.54×10^{-3} S/cm^2, which satisfies the basic requirements of a solid electrolyte. The Zn||Zeolite-Zn||Zn cell exhibited reversible plating/stripping

Table 8
Summary of some recently reported SE applications in SZIBs.

	Electrolyte	Conductivity (mS/cm)	Zn^{2+} migration number	Temperature (°C)	Cycle (h) (symmetric Zn cells) (mA/cm^2/mAh/cm^2)	Ref.
SPEs	PPM-SPEs	2.87×10^{-2}	0.142	r.t to 60	400 (0.05/0.025)	[235]
	PSPZ	0.446	0.71	−20 to 80	4800 (0.1/0.1)	[239]
	PEC@GF-30%SN	5.183×10^{-2}	0.61	−40 to 60	1950 (0.1/0.1)	[246]
	PVA-inter-$PEG_{30\%}$/$IL_{70\%}$	2.264	–	r.t.	3000 (0.2/0.2)	[252]
	ILZE	16.9	–	−20 to 70	1500 (2/0.5)	[253]
	PVHF/MXene-g-PMA	0.269	0.16	−25 to 85	1200 (0.1/0.1)	[258]
	pH/MXene	0.452	0.435	r.t.	2500 (0.1/0.1)	[259]
GPEs	PZ3T	1.243×10^{-2}	–	r.t.	3000 (0.5/0.5)	[268]
	GPHEs	21	–	r.t.	500	[269]
	PVA/EG/GO	10.25	–	−20 to 25	150 (0.1/-)	[270]
	PAM-LDH	19.2	–	r.t.	–	[273]
	CPZ-2	–	–	25 to 45	980 (0.5/-)	[274]
	LPH	21.57	0.79	r.t.	4000 (0.5/1)	[275]
	CCNF@XG	11.7	0.78	r.t.	3600 (0.5/0.5)	[276]
ESEs	HICs	11.2	0.61	−20 to 25	1000 (0.5/0.5)	[278]
	ZCE	0.669	0.73	−10 to 60	2500 (0.01/-)	[279]
	DEE@PCN-222	0.313	0.74	r.t.	2476 (1/1)	[280]
	DA-ETG	0.64	0.77	−20 to 25	1500	[281]
SIEs	Zeolite-Zn	2.54	0.866	r.t.	1100 (0.2/0.05)	[282]

behavior at 0.2 mA/cm^2@0.05 mAh/cm^2 for 1100 h. The Zn||Zeolite-Zn||$NH_4V_4O_{10}$ cell had 84.9% capacity retention after 1010 cycles at 0.5 A/g. Even at a high temperature of 60 °C, a residual capacity of 239.2 mAh/g was maintained after 110 cycles (Fig. 21h). A theoretical basis for the application of zeolite-based solid electrolytes in ZIB was provided by theoretical calculations of two different diffusion paths of zinc ions and V^{3+} along the diffusion energy barrier in Figs. 21i-k. The diffusion barriers of zinc ions in path 1 and path 2 were 0.82 and 1.42 eV, respectively, while the diffusion barriers of V^{3+} were 3.95 and 2.95 eV, respectively. The smaller diffusion energy barrier of Zn^{2+} ions in zeolite favors the conduction of Zn^{2+} ions, whereas the larger diffusion energy barrier of V^{3+} ions in zeolite can impede their shuttling during the charging process. The electron insulator and zinc ion conductor properties of zeolite molecular sieves satisfy the basic requirements for use as SEs for ZIBs, favoring zinc migration and blocking electron transfer. This study provided a new idea for the application of zeolite-based SEs in zinc-based batteries and a new way to realize the industrialization of zinc secondary batteries. Table 8 presents a summary of some recently reported applications of SEs in SZIBs. In Table 8, SPEs, GPEs, ESEs, and SIEs have been utilized in SZIBs to enhance its conductivity, Zn^{2+} migration number, and cycle stability.

3.3. Electrode-electrolyte interface

In SZIBs, the electrode-electrolyte interface is a critical part of battery performance. It refers to the contact area formed between the Zn anode or cathode and the electrolyte within the battery. This interface serves as a transitional zone between the electronic conductor (electrode) and the ionic conductor (electrolyte), thereby playing a crucial role in enabling electrode reactions and ion transport. Furthermore, during charging and discharging, a series of chemical reactions occur at the interface between the electrode and the electrolyte. These reactions may include the intercalation and removal of Zn ions, the decomposition and reconstitution of electrolytes, as well as the formation and evolution of interfacial layers [283]. These reactions exhibit a major influence on the battery performance, including cycle life, capacity, and safety. There is a stability issue at the electrode-electrolyte interface in SZIBs. SEs transformed the solid–liquid interface into a solid-solid interface by replacing the LE and separator. The reduction of active water molecules offered excellent chemical and thermal stability to these interfaces [284]. The growth of Zn dendrites on the anode surface and the dissolution of the material at the cathode interface were effectually controlled. Thus, SEs exhibited superior corrosion resistance, which provides greater safety. However, the SZIBs is prone to contact failure due to the mismatch between the stress and strain of the electrode as well as the electrolyte during charging and discharging [285]. The inherent low IC of SEs complicated the diffusion of Zn ions in the cathode, particularly when high-area loading and high-energy density were pursued. Therefore, it is crucial to improve the solid–solid interface structure, charge transfer, and the efficiency of ion transport [286,287]. To enhance the interface between electrolyte and electrode in SZIBs and improve battery performance, researchers have adopted a variety of interface modification and optimization strategies. In this section, these strategies include selection and optimization of electrode and electrolyte materials, as well as the construction and control of interface layers.

3.3.1. Selection and optimization of electrolyte and electrode materials

Optimizing the interface between the electrolyte and electrode can be done by electrolyte modification. For example, electrolyte material modification such as doping and coating thereby improving the battery performance. For instance, Ma *et al.* used an *in-situ* polymerization of amorphous solid poly(1,3-dioxane) electrolyte to inhibit Zn dendrites, thereby effectually stabilizing the anode electrolyte interface (AEI) and enhancing cycling performance [288]. Additionally, Zhang *et al.* optimized the solvation structure of zinc ions, improved the interface properties of anode electrolyte, and achieved uniform zinc deposition by selecting appropriate salt pairs and organic co-solvents [289]. Modification of electrode materials such as coating and doping can improve their conductivity, structural stability, and compatibility with electrolytes [290,291]. Additionally, the design of electrode materials with special structures such as porous structures and nanostructures, can also increase the contact area between the electrode and the electrolyte, thereby enhancing the ion transport efficiency.

For example, Wang *et al.* constructed a flexible self-supported rGO|CNT@SHQP|rGO film with a sandwich-like hierarchical structure as the cathode of SZIB [292], which was reduced with hydroiodic acid (HI) by vacuum filtration to form a dense conductive network. The core-shell structural design of sulfur heterocyclic quinone polymer (SHQP) and CNT was achieved by interfacial

polymerization strategy, which can appropriately endow the CNT@SHQP composites with more accessible reactive sites (C=O groups) and reactive interfaces for the storage of Zn^{2+}, and at the same time, the electron transfer ability was enhanced due to the introduction of highly conductive CNTs. During the interfacial polymerization process, the interfacial π-π interaction drove the directed self-assembly of SHQP molecules on the CNT surface to form a uniform nanocovering layer, which effectively exposed the C=O active sites, accelerated the electron transfer, shortened the diffusion path of Zn^{2+} ions, and buffered the volume change while enhancing the structural stability of the SHQP nanolayers. The EIS characterization revealed that the CNT@SHQP nanolayers with enhanced electrical conductivity exhibit significant benefits in facilitating Zn^{2+} ion diffusion while simultaneously improving bulk conductivity. Compared with pristine CNT and SHQP, the Zn^{2+} storage capacity of CNT@SHQP nanowires demonstrates significant improvement, indicating a synergistic interaction between SHQP and CNT that enhances ion adsorption and charge transfer efficiency. The constructed flexible self-supported rGO|CNT@SHQP|rGO films with sandwich-like hierarchical structure enabled the electrode to achieve a high capacity of 206.9 mAh/g at 0.1 A/g, which was a 5.6-fold enhancement compared to pure SHQP, and the 88.7 % capacity retention after 2000 cycles, 97 mAh/g capacity at 0.4 A/g under bending conditions, and 76.2 % long-term cycling stability. The performance enhancement by a single component is limited, so the electrolyte-electrolyte interface layer can be improved by synergistic optimization of the electrolyte and electrode materials. Liu *et al*. used an epoxy resin-based binder to optimize the structural electrode and a high-performance SE to prepare carbon fiber zinc-ion structural battery composites, achieving high mechanical strength and energy density [293]. The carbon fiber structural electrodes were reinforced with epoxy resin-based adhesive (SE-EI) (Fig. 22a), thereby enhancing the interfacial adhesion between the active material and the carbon fiber current collectors (SE-R). The SPE assembled from E51 epoxy resin and PEO-based ionic gel (Fig. 22b) then had a high IC of 0.49 mS/cm and a tensile strength of 18.1 MPa. With the optimized structured electrodes and SE, the fabricated coupled zinc-ion structured battery had a high energy density of 7.8 Wh/kg, and a power density of 1.6 W/kg. Tests at different tensile stresses (Fig. 22c) and extreme environments (Fig. 22d) confirmed the electrochemical durability and structural stability of the device. This study establishes a systematic framework for the design and fabrication of carbon fiber structural energy storage composites that inherently combine safety, high energy density, and superior mechanical strength.

In summary, by optimizing the modification of SE and electrode materials (*e.g.*, doping, coating, and porous structure design), the interfacial resistance can be effectively reduced, the ion transport efficiency can be enhanced, and the Zn dendrite growth and interfacial corrosion can be suppressed. However, SZIBs still face challenges such as solid-solid interfacial contact failure, insufficient SE intrinsic IC, and limited Zn^{2+} diffusion under high area loading. Breaking through the contradiction between high energy density demand and ion transport kinetics, as well as constructing stable and efficient solid-solid interfacial structures, remain key challenges to enhance the performance and practicalization of SZIBs.

3.3.2. Construction and control of the interface layer

The construction and control of the interfacial layer usually occurs at the anode surface to form AEI, whose main function is to overcome the poor IC caused by the dependence of zinc ion transport on the random transport of polymer chains, and thus to enhance the cycling stability and efficiency. The zinc anode interface design effectively isolates the zinc anode from direct contact with the LE and reduces the accumulation and deposition of zinc ions at the anode tip, thus effectively inhibiting HER, corrosion, and zinc dendrite generation [294–296]. In SZIB, Qiu *et al*. utilized the crystal surface orientation control to construct a stable AEI [297]. SSE-TMP was prepared by adding phosphorus-containing organic additive trimethyl phosphate (TMP) to change the coordination environment of Zn^{2+} in SPE, which successfully induced the uniform deposition of Zn^{2+}. Compared with the pure polymer solid state electrolyte (SSE-0) and polymer electrolytes prepared with the addition of ethylene carbonate (SSE-EC) and propylene carbonate (SSE-PC), the lower surface-height difference in SSE-TMP contributed to the rapid transport of Zn^{2+} at the electrolyte-electrode interface. The SSE-TMP efficiently regulated the coordination environment around Zn^{2+} and reduced the solvent electron cloud density of the sheath. SSE-TMP has a higher IC (5.10×10^{-4} S/cm, 25 °C) and a wider electrochemical stability window (2.55 V) than SSE-0, SSE-EC, and SSE-PC. The symmetric Zn/Zn battery assembled using SSE-TMP demonstrates exceptional operational stability, exceeding 6000 h at 0.1 mA/cm^2, which can be attributed to the synergistic effect of its intrinsic layered structure and superior interfacial compatibility with electrodes. Furthermore, extensive *in situ* characterization combined with MD simulations, COMSOL simulations and DFT calculations demonstrated that the incorporation of TMP induced a homogeneous deposition of Zn^{2+} along the Zn (002) crystal surface from the point of view of the intrinsic structure of the SPE. This work was informative for the commercial application of SPEs by tuning the Zn^{2+} solvent sheath structure and optimizing the microkinetic reaction behavior at the electrolyte-electrode interface through the addition of TMP to SPEs.

The cathode electrolyte interface (CEI) is located between the cathode and the electrolyte, and plays the roles of inhibiting the dissolution of the electrode materials, reducing the side reactions, and stabilizing the crystal structure. Currently, the common construction method is to enhance the ion transport between the cathode and electrolyte interface through the construction of cathode materials while buffering the volume change of the cathode to ensure the stability of the cathode. Du *et al*. proposed an integrated "interface-free" electrolyte/cathode architecture to mitigate strain defects originating from ion transfer processes at the electrolyte/electrode interface [298]. They employed a 3D vertically porous aerogel (VTi) through a simplified ice-templating method, employing self-assembled V_2O_5 and Ti_3C_2 composites as the structural building blocks. Subsequently, the SA solution was infused into the porous structure to form a complementary SA electrolyte layer, thereby generating the complete CEI (VTiS) with enhanced interfacial stability. Figs. 22e-h illustrated the SEM and EDS element mapping of a ligand synthesis for an interfacial integrated cathode, respectively. The outstanding metal-like conductivity and polymer network of Ti_3C_2 MXene jointly limited the structural collapse of V_2O_5. The *in-situ* polymerization of porous cathode SA increases the cathode/electrolyte interfacial contact area while forming an abundant hydrogen-bonded network on its surface, thereby mitigating stress-strain defects induced by charge/discharge cycling. Given its vertical cross-interface structure, the charge transfer distance was shortened, and it exhibited exceptionally low charge transfer resistance (R_{ct}) (18.3 Ω) (Fig. 22i). This *in-situ* generation of CEI effectively regulated Zn-ion transports, allowing the assembled battery to stably cycle 100 times at 0.1 mA/cm^2 (Fig. 22j). Given these superiorities, the integrated cathode/electrolyte structure offered superior rate and cycling performance at r.t. Although the long diffusion time of Zn^{2+} from the CEI to the active material due to the composition of the *in situ* CEI results in a long activation cycle. This novel crosslinking strategy utilizing SA introduces groundbreaking innovations in the assembly process and interface design of SZIB, marking a paradigm shift in structural-electrochemical co-design methodologies.

In summary, by constructing a stable interfacial layer and regulating its components, structure and thickness, the interfacial

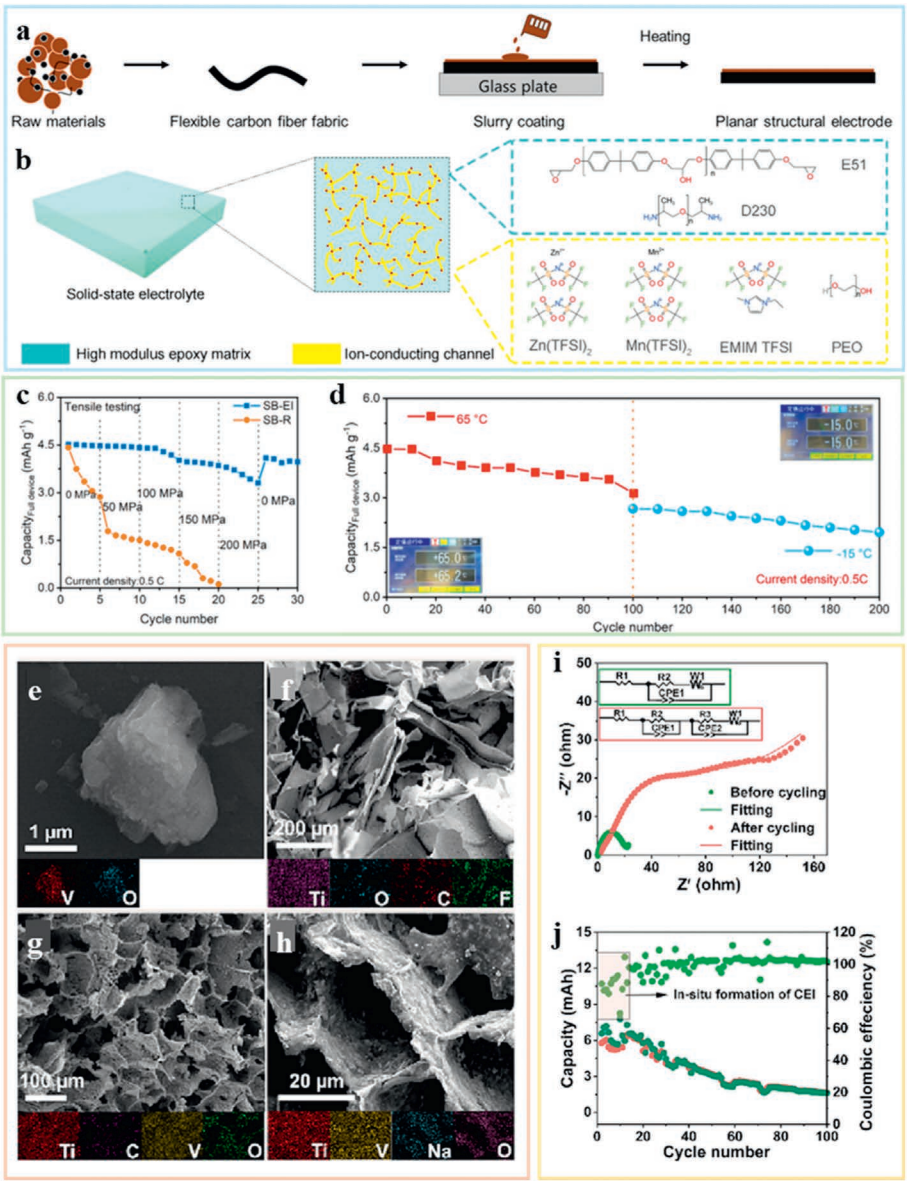


Fig. 22. (a) Schematic illustration of the fabrication process of the structural electrode. (b) Schematic diagram of the solid electrolyte and the chemical structures of the high modulus matrix and ion-conducting channel. (c) The electrochemical performance of SB-EI and SB-R at various tensile stresses. (d) The cycle performance of structural batteries at different temperatures. Copied with permission [293]. Copyright 2025, Elsevier. The SEM and EDX element mapping images of (e) the V_2O_5, (f) the few-layered Ti_3C_2 MXene NSs, (g) the VTi aerogels, and (h) the VTiS. (i) EIS spectra of the VTiS before and after 100 cycles. (j) Long-duration stability performance of cells at the current density of 0.1 mA/cm^2. Copied with permission [298]. Copyright 2024, Elsevier.

side reactions of SZIBs can be effectively suppressed, and the performance and safety can be improved. However, the maintenance of long-term dynamic stability of the interfacial layer, multi-parameter synergistic optimization, tolerance under complex working conditions, and scale-up of the precise preparation process are still the core challenges, which need to be overcome to realize the practical application of high performance by overcoming the mechanism of interfacial degradation and the difficulties of cross-scale design.

Given the continuous development of SZIB technology, the performance of the interface layer between SE and electrode was continuously optimized. In the future, innovations in the field of material engineering, such as the development of functionalized interface layers or hybrid SEs, are expected to solve the current interface challenges faced by SZIBs. Concurrently, with the continuous improvement of the production process and the realization of large-scale production, the cost of SZIBs gradually decreased, laying a solid foundation for the commercial application of SZIBs. Extensive research on properties, issues, and modification strategies of the interface layer between SE and electrode, as well as continuous exploration of new materials and process methods, is expected to facilitate the advancement and commercial application of SZIBs technology.

4. Conclusion and outlook

This paper examines a comprehensive overview of the structure and working principle of SZABs and SZIBs, detailing the various modification strategies aimed at enhancing their performance, specifically focusing on the cathode, SE, and interfacial interactions. Catalytic activity is crucial for efficient electrochemical processes, and this paper further discusses the advancements in catalyst design for SZABs. The choice of solid electrolyte material significantly determines the electrochemical properties, particularly

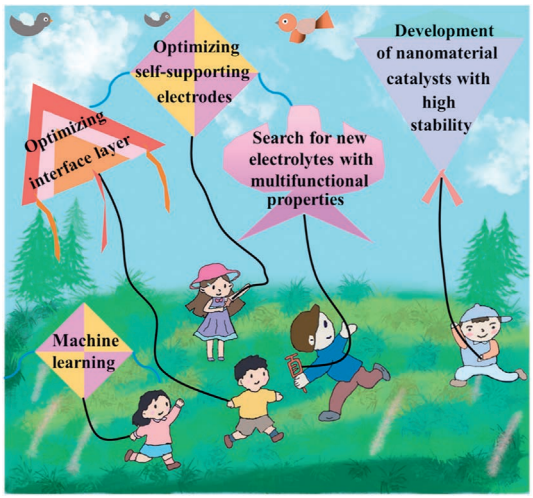


Fig. 23. Outlook for the future development of solid-state Zn-air batteries and Zn-ion batteries.

ionic conductivity in electrochemical reactions. The optimization of PEs, ion exchange membranes, and neutral/acidic electrolytes was discussed, alongside the integration of various additives, including SiO_2, LDHs, cellulose, and organic solvents. These methods demonstrated excellent performance in optimizing the mechanical properties, temperature tolerance, ionic conductivity, and electrode interface stability. Additionally, the interface layer played a vital role in determining the cycle stability, rate performance, and SZIBs safety. This paper emphasized the selection of appropriate interface layer materials and construction methods to effectively minimize direct contact between the electrolyte and the electrode, thereby decreasing the occurrence of interfacial side reactions.

Despite the progress achieved in SZABs and SZIBs, several challenges remain that require significant innovation in key areas to pave the way for a new era of these batteries, particularly in enhancing temperature resistance. Therefore, given current research advancements and existing bottlenecks in SZABs and SZIBs, the following recommendations were proposed to further enhance the performance of SZBs (Fig. 23):

(1) In SZABs, the density and intrinsic activity of active sites within bifunctional catalyst materials are critical determinants of the ORR/OER performance of the electrocatalyst. Despite nanomaterials exhibiting a huge specific surface area, which is conducive for increasing active sites during electrochemical exchange, issues such as particle agglomeration and surface oxidation often arise during bending and deformation operations, thereby compromising the mechanical properties of SZABs. MXenes are emerging two-dimensional materials with excellent thermal/chemical stability, good adsorption capacity, electrical conductivity and unique topological characteristics that can be used as a catalytic active site in energy storage devices [299]. Future studies may focus on developing Mxenes bifunctional nanomaterial catalysts that exhibit high stability and excellent mechanical properties through surface modification and anti-corrosion doping techniques, thereby enhancing the adaptability of SZABs to extreme environmental conditions such as bending and stretching.

(2) Machine learning offers computational simplicity, cost-effectiveness, and flexibility, which emerges as a transformative force throughout the engineering life cycle of electrochemical cells. The utilization of machine learning to monitor and model cell temperature trends and health can prevent risks of thermal runaway. By optimizing structure-property relationships, doping strategies, defect engineering, reaction conditions, and side reaction mitigation, machine learning quickly identifies potential catalytic candidates from a large number of candidate materials to achieve predictive design of high-performance catalysts. In addition, machine learning can extract descriptors from SEs crystal structures to construct quantitative relationships between crystal structures and their intrinsic ionic conductivities, and can simulate the electronic properties and atomic structure of materials to understand the structure-activity relationship of solid electrolytes at the atomic level, providing rational strategies for high-throughput screening and design of SEs with high ionic conductivities. Machine learning collects dendrite images corresponding to different diffusion coefficients of zinc ions and performs simulation calculations to predict the maximum dendrite growth height and space utilization ratio corresponding to given ion transport parameters.

(3) The compatibility of the electrolyte with the anode and cathode, as well as the IC of the electrolyte and water retention capabilities, were essential factors affecting the stability, capacity, lifespan, and temperature range of the SZABs and SZIBs cycles. Currently, the rapid evaporation of most SEs at high temperatures resulted in battery expansion and absorption of moisture from the surrounding environment, thus negatively affecting OH^- transfer. Conversely, at low temperatures, the electrolyte was prone to freezing, thereby compromising performance. Therefore, the pursuit of new electrolytes with multifunctional properties is crucial to enhance the safety and environmental adaptability of SZABs and SZIBs. Future research can explore the use of two or three deep eutectic solvent substances to create ESEs through hydrogen bonding or coordination among components, which can extend the cycle life of ZBs at extreme temperatures.

(4) The interface contact between electrolyte and electrode material will uncontrollably produce zinc dendrites, hydrogen evolution and other serious side reactions. Upon optimizing the interface layer, the growth of Zn dendrites was inhibited, the migration rate of Zn ions was increased, and the cycle life of the battery was extended. Future research should focus on the formation mechanisms of the interface layer and Zn-ion migration mechanism, thereby offering theoretical guidance for the optimal design of SZIBs. Metalophilic layer is coated on SEs surface to adjust interface wettability and establish stable solid electrolyte layer to improve interface compatibility and mass transfer kinetics in SZABs and in SZIBs, thus inhibiting the formation of Zn dendrites and increasing battery capacity. Additionally, exploring new interface layer materials with 3D zincophilic structure to reduce deposition overpotential and *in-situ* characterization technologies to study the influence of temperature and pressure on interface growth can inhibit the growth of Zn dendrites, enhance battery safety, and decrease costs to achieve the commercial application of SZBs.

(5) The recent development in flexible and portable FSZAB and FZABs holds promising potential for wearable electronic devices such as wearable phones and smart bands. The manufacture of FSZAB and FZABs under deformation conditions requires optimized treatment of packaging materials, electrolyte membranes, and flexible fluid collectors to maintain stable electrochemical performance. Additionally, upon optimizing the preparation conditions to improve the interaction between active materials and the substrate, binder-free self-supporting electrodes can be obtained, which correlate with the strict requirements of flexible electronics. In conclusion,

SZAB and SZIB are expected to play a leading role in the post LIB era.

CRediT authorship contribution statement

Ya Han: Writing – original draft. **Kejun Jin:** Writing – original draft. **Tingyu Zhao:** Writing – original draft. **Yingjian Yu:** Writing – review & editing, Project administration, Funding acquisition.

Declaration of competing interest

The authors declare that they have no known competing financial interests or personal relationships that could have appeared to influence the work reported in this paper.

Acknowledgments

This work was financially supported by the National Natural Science Foundation of China (No. 62464010), Spring City Plan-Special Program for Young Talents (No. K202005007), Yunnan Talents Support Plan for Yong Talents (No. XDYC-QNRC-2022–0482), Yunnan Local Colleges Applied Basic Research Projects (No. 202101BA070001–138), and Frontier Research Team of Kunming University 2023.

References

[1] H.Y. Liu, J.Z. Zhang, P. Xiang, et al., Energy Storage Mater. 66 (2024) 103234.
[2] K. Jin, Y. Yu, J. Energy Chem. 104 (2025) 382–396.
[3] X. Li, M. Yin, J. Zhang, et al., J. Power Sources 631 (2025) 236236.
[4] M. Wu, N. Huang, M. Lv, et al., Front. Chem. Sci. Eng. 19 (2025) 15.
[5] Y. Han, Y. Zhao, Y. Yu, Energy Storage Mater. 69 (2024) 103429.
[6] Z. Liu, J. Liu, X. Xiao, et al., Adv. Mater. 36 (2024) 2404140.
[7] Y. Han, Y. Yu, Chin. Chem. Lett. 36 (2025) 110144.
[8] K. Feng, Y. Zhao, Z. Liu, et al., J. Colloid Interface Sci. 678 (2025) 76–87.
[9] Y. Zhao, K. Feng, Y. Yu, et al., J. Energy Chem. 102 (2025) 524–533.
[10] X. Zhang, F. Deng, Z. Liu, et al., J. Colloid Interface Sci. 674 (2024) 722–734.
[11] J. Chen, Z. Liu, K. Feng, et al., Compos. Pt. B: Eng. 289 (2025) 111936.
[12] M.B. Poudel, M.P. Balanay, P.C. Lohani, et al., Adv. Energy Mater. 14 (2024) 2400347.
[13] Y. Zhao, Y. Han, Y. Yu, Chem. Eng. J. 497 (2024) 154997.
[14] Z. Lui, B. Fu, M. Li, et al., Angew. Chem. Int. Ed. 64 (2024) e202417049.
[15] X. Yin, W. Sun, K. Chen, et al., Adv. Sci. 11 (2024) 2402343.
[16] Z. Zheng, X. Zhong, Q. Zhang, et al., Nat. Commun. 15 (2024) 753.
[17] J.N. Liu, C.X. Zhao, J. Wang, et al., Energy Environ. Sci. 15 (2022) 4542–4553.
[18] M. Aizudin, W. Fu, R. Pottammel, et al., Small 20 (2023) 2305217.
[19] J. Park, M. Park, G. Nam, et al., Adv. Mater. 27 (2015) 1396–1401.
[20] Y. Zeng, X. Zhang, Y. Meng, et al., Adv. Mater. 29 (2017) 1700274.
[21] J. Chen, J. Luo, Y. Xiang, et al., J. Energy Chem. 91 (2024) 178–193.
[22] H. Li, Y. Liu, Z. Chen, et al., J. Colloid Interface Sci. 639 (2023) 408–415.
[23] S. Lei, Z. Liu, C. Liu, et al., Energy Environ. Sci. 15 (2022) 4911–4927.
[24] C. Li, L. Li, B. He, et al., Mater. Sci. Eng. R 148 (2022) 100671.
[25] Y. Wang, Q. Li, M. Wang, et al., Nano Lett. 24 (2024) 13653–13661.
[26] Y. Pan, Z. Liu, S. Liu, et al., Adv. Energy Mater. 13 (2023) 2203766.
[27] X. Zhong, Y. Shao, B. Chen, et al., Adv. Mater. 35 (2023) 202301952.
[28] M. Du, B. Chu, Q. Wang, et al., Adv. Mater. 3 (2024) 2412978.
[29] L. Zong, M. Li, P. Li, et al., Angew. Chem. Int. Ed. 64 (2024) e202413933.
[30] H. Wang, L. Kang, K. Wang, et al., Adv. Funct. Mater. 34 (2024) 2407347.
[31] R. Li, L. Li, R. Jia, et al., Small Methods 4 (2020) 2000363.
[32] H. Liu, Q. Liu, Y. Wang, et al., Chin. Chem. Lett. 33 (2022) 683–692.
[33] K. Zahra, T. Noor, N. Iqbal, et al., J. Energy Storage 88 (2024) 111565.
[34] L. Bai, D. Wang, W. Wang, et al., ChemSusChem 17 (2024) e202400080.
[35] Y. Li, M. Gong, Y. Liang, et al., Nat. Commun. 4 (2013) 1805.
[36] J. Mei, T. Liao, J. Liang, et al., Adv. Energy Mater. 10 (2020) 1901997.
[37] J. Choi, H. Jang, J. Park, et al., Chem. Eng. J. 497 (2024) 154561.
[38] Y. Gao, L. Liu, Y. Jiang, et al., Nano-Micro Lett. 16 (2024) 162.
[39] X. Yi, Y. Song, D. He, et al., J. Mater. Chem. A 43 (2024) 5182.
[40] Y. Fan, W. Wang, Y. Chen, et al., Mater. Chem. Front. 8 (2024) 2394–2419.
[41] J. Wang, X. Chen, H.B. Yuan, et al., Appl. Surf. Sci. 679 (2025) 161264.
[42] Z. Xiong, Z. Zhang, X. Jiang, et al., J. Energy Storage 98 (2024) 112976.
[43] X. Yan, Y. Ha, R. Wu, et al., Small Methods 5 (2021) 2000827.
[44] C. Hu, Q. Liang, Y. Yang, et al., J. Colloid Interface Sci. 633 (2023) 500–510.
[45] B.Q. Li, S.Y. Zhang, B. Wang, et al., Energy Environ. Sci. 11 (2018) 1723–1729.
[46] Y. Wang, R. Gan, S. Zhao, et al., Appl. Surf. Sci. 598 (2022) 153891.
[47] K. Ao, X. Yue, X. Zhang, et al., J. Colloid Interface Sci. 672 (2024) 107–116.
[48] J. Deng, L. Wang, F. Jin, et al., J. Mater. Chem. A 9 (2021) 11145–11150.
[49] T. Lu, X. Hu, J. He, et al., Nano Energy 85 (2021) 106024.
[50] Q. Xie, W. Si, Y. Shen, et al., Nanoscale 13 (2021) 16296–16306.
[51] A. Yu, Z. Peng, Y. Li, et al., ACS Appl. Mater. Interfaces 14 (2022) 42337–42346.
[52] Y. Liu, K. Zou, T. Zhang, et al., Chem. Eng. J. 433 (2022) 133560.
[53] D. Yan, C. Xia, C. He, et al., Small 18 (2022) 2106606.
[54] Q. Zhang, Z. Zheng, R. Gao, et al., Adv. Mater. 36 (2024) 2401018.
[55] Y. Meng, J.C. Li, S.Y. Zhao, et al., Appl. Catal. B 249 (2021) 120239.
[56] D. Zhang, P. Sun, Q. Zhou, et al., Appl. Surf. Sci. 542 (2021) 148700.
[57] N. Shang, S. Li, X. Zhou, S. Gao, et al., Appl. Surf. Sci. 537 (2021) 147818.
[58] D. Wang, H. Xu, P. Yang, et al., J. Mater. Chem. A 9 (2021) 9761–9770.
[59] J. Hu, X. Cai, J. Wu, et al., Chem. Eng. J. 430 (2022) 133105.
[60] D. Zhou, H. Fu, J. Long, et al., J. Energy Chem. 64 (2022) 385–394.
[61] Y. Hao, Y. Kang, H. Kang, et al., J. Power Sources 524 (2022) 231076.
[62] Q. Zhou, Z. Yao, X. Zeng, et al., Mater. Today Chem. 24 (2022) 100844.
[63] Y. Zhu, X. Wang, J. Shi, et al., Sci. China Chem. 65 (2022) 1445–1452.
[64] Y. Yang, Y. Xiao, L. Zhang, et al., Appl. Catal. B: Environ. 3479 (2024) 123792.
[65] Y. Han, Q. Wei, Y. Fu, et al., Small 19 (2023) 2300683.
[66] G. Liu, X. Xia, C. Zhao, et al., J. Colloid Interface Sci. 588 (2021) 627–636.
[67] Q. Liu, P. Qiao, D. Shen, et al., Energy Environ. Sci. 18 (2025) 2839–2851.
[68] M. Shen, Q. Liu, J. Sun, et al., J. Colloid Interface Sci. 673 (2024) 453–462.
[69] L. Zhang, L. Zong, F. Lu, et al., Appl. Catal. B: Environ. 307 (2025) 125189.
[70] G. Zhang, K. Fan, L. Zong, et al., J. Colloid Interface Sci. 686 (2025) 1157–1167.
[71] F. Chen, H. Hu, M. Jing, et al., J. Alloys Compd. 1016 (2025) 178835.
[72] L. Lan, Y. Wu, Y. Pei, et al., Adv. Mater. 37 (2025) 2417711.
[73] H. Liu, P. Li, K. Fan, et al., Angew. Chem. Int. Ed. 64 (2025) e202501307.
[74] B. Zhang, J. Dang, H. Li, et al., Adv. Funct. Mater. 35 (2025) 2502834.
[75] Y. Liu, T. Zhang, Y.E. Duan, et al., J. Colloid Interface Sci. 604 (2021) 746–756.
[76] K. Tang, C. Yuan, Y. Xiong, et al., Appl. Catal. B 206 (2020) 118209.
[77] X. Shu, S. Chen, S. Chen, et al., Carbon 157 (2020) 234–243.
[78] C. Xu, J. Zhang, H. Dou, et al., Rare Met. 44 (2025) 3156–3169.
[79] L. Huo, M. Lv, M. Li, et al., Adv. Mater. 36 (2024) 202312868.
[80] Q. Chang, F. He, Z. Zhang, et al., Angew. Chem. Int. Ed. 64 (2025) e202416664.
[81] J. Balamurugan, P.M. Austeria, J.B. Kim, et al., Adv. Mater. 35 (2023) 202302625.
[82] Q. Sun, Z. Chen, K. Dong, et al., J. Colloid Interface Sci. 692 (2025) 137537.
[83] Y. Rao, S. Chen, Q. Yue, et al., ACS Catal. 11 (2021) 8097–8103.
[84] M. Cao, Y. Liu, K. Sun, et al., Small 18 (2022) 2202014.
[85] C.Y. Song, C.J. Huang, H.M. Xu, et al., Small 20 (2024) 2402761.
[86] Y. Niu, X. Teng, S. Gong, et al., Energy Storage Mater. 43 (2021) 42–52.
[87] Z. Zhang, Y.P. Deng, Z. Xing, et al., ACS Nano 13 (2019) 7062–7072.
[88] Y. Wang, X. Wu, X. Jiang, et al., Chem. Eng. J. 434 (2022) 134744.
[89] Y. Tian, L. Xu, M. Li, et al., Nano-Micro Lett. 13 (2021) 3.
[90] Y. Guo, P. Yuan, J. Zhang, et al., Adv. Funct. Mater. 28 (2018) 1805641.
[91] K. Wu, L. Zhang, Y. Yuan, et al., Adv. Mater. 32 (2020) 2002292.
[92] W. Zhai, S. Huang, C. Lu, et al., Small 18 (2022) 2107225.
[93] Y. Wei, H. Xia, H. Lan, et al., Adv. Energy Mater. 14 (2023) 2303011.
[94] J.T. Ren, Y.S. Wang, L. Chen, et al., Chem. Eng. J. 389 (2020) 124408.
[95] K. Wang, X. Zhang, J. Lyu, et al., Nano Mater. Sci. 8 (2026) 585–611.
[96] S. Wang, H. Wang, C. Huang, et al., Appl. Catal. B 298 (2021) 120512.
[97] L. Gao, S. Chang, Z. Zhang, et al., ACS Appl. Mater. Interfaces 13 (2021) 22282–22291.
[98] N.K. Wagh, D.-H. Kim, S.-H. Kim, et al., ACS Nano 15 (2021) 14683–14696.
[99] Z. Zhu, Q. Xu, Z. Ni, et al., ACS Sustainable Chem. Eng. 9 (2021) 13491–13500.
[100] S. Ren, X. Duan, M. Lei, et al., Chem. Eng. J. 427 (2022) 131614.
[101] T. Qin, Z. Pei, J. Qiu, et al., Small 21 (2024) 2402762.
[102] J. Li, Y. Kang, W. Wei, et al., Chem. Eng. J. 407 (2021) 127961.
[103] Z. Li, H. Li, M. Li, et al., Energy Storage Mater. 42 (2021) 118–128.
[104] S. Chang, H. Zhang, Z. Zhang, J. Energy Chem. 56 (2021) 64–71.
[105] D. Wang, H. Xu, P. Yang, et al., J. Mater. Chem. A 9 (2021) 13678–13687.
[106] K. Chen, L. Wang, J. Long, et al., Chem. Eng. J. 496 (2024) 153820.
[107] H. Zhang, M. Zhao, H. Liu, et al., Nano Lett. 21 (2021) 2255–2264.
[108] Z. Chen, L. Han, Inorg. Chem. Front. 11 (2024) 29–49.
[109] L. Lin, P. Xue, X. Cui, et al., J. Alloys Compd. 909 (2022) 164625.
[110] L. Liu, Z. Hu, M. Wang, et al., J. Alloys Compd. 925 (2022) 166665.
[111] W. Xie, Y. Liu, H. Chen, et al., J. Colloid Interface Sci. 625 (2022) 278–288.
[112] J. Long, C. Chen, X. Gou, J. Colloid Interface Sci. 625 (2022) 555–564.
[113] J.T. Ren, Y.D. Ying, Y.P. Liu, et al., J. Energy Chem. 71 (2022) 619–630.
[114] L. Wang, J. Long, C. Chen, et al., J. Electrochem. Soc. 169 (2022) 093507.
[115] D. Chen, J. Yuan, J. Zhang, et al., Energy Storage Mater. 101 (2024) 113772.
[116] J. Long, J. Chen, C. Chen, et al., J. Colloid Interface Sci. 629 (2023) 73–82.
[117] D. Sun, H. Cui, J. Sha, et al., ACS Appl. Nano Mater. 7 (2024) 14760–14768.
[118] S. Wang, M. Zhang, X. Mu, et al., Energy Environ. Sci. 17 (2024) 4847–4870.
[119] X. Li, J. Qin, Q. Lin, et al., Adv. Sci. 18 (2024) 2401187.
[120] R. Tang, X. Yuan, W. Yang, et al., Small 21 (2025) 2410264.
[121] X. Meng, Y. Yuan, J. Feng, et al., Chem. Eng. J. 479 (2024) 147648.
[122] X. Liu, X. Yang, Z. Zhao, et al., ACS Appl. Mater. Interfaces 16 (2024) 18703–18712.
[123] Y. Liu, Z. Li, Y. Zeng, et al., Carbon Energy 7 (2025) e682.
[124] W. Wang, J. Wang, S. Pan, et al., Adv. Funct. Mater. 35 (2025) 2425430.
[125] J.X. An, Y. Meng, L. Fang, et al., Energy Storage Mater. 70 (2024) 103520.
[126] S. Das, A. Pathak, U. Phadikar, et al., Adv. Funct. Mater. 34 (2024) 2407078.
[127] X. Zhang, Y. Liu, Y. Liu, et al., Adv. Fiber Mater. 7 (2025) 950–961.
[128] J. Zhong, Z. Liang, N. Liu, et al., ACS Nano 18 (2024) 5258–5269.
[129] K. Chen, C. Chen, J. Long, G. Zhou, et al., Appl. Surf. Sci. 657 (2024) 159803.
[130] J.S. Sanchez, Z. Xia, K. Mirehbar, et al., J. Mater. Chem. A 12 (2024) 11945–11959.
[131] X. Li, D.C. Nguyen, K. Dong, et al., Chem. Eng. J. 489 (2024) 151210.
[132] L. Wang, J. Huang, X. Hu, et al., J. Colloid Interface Sci. 660 (2024) 989–996.

[133] L. Yan, Z. Xu, W. Hu, et al., Nano Energy 82 (2021) 105710.
[134] Q.D. Ruan, Y.C. Zhao, R. Feng, et al., Small 303 (2024) 122515.
[135] X. Sun, T. Xu, W. Sun, et al., J. Alloys Compd. 898 (2022) 162778.
[136] T. Hu, Z. Jiang, Z. Fu, et al., J. Mater. Chem. A 10 (2022) 8739–8750.
[137] X. Duan, S. Ren, F. Ge, et al., Nanoscale 13 (2021) 17655–17662.
[138] M. Yu, F. Guo, L. Xu, et al., Adv. Funct. Mater. 35 (2024) 2411935.
[139] M. Gopalakrishnan, W. Kao-ian, M. Rittiruam, et al., ACS Appl. Mater. Interfaces 16 (2024) 11537–11551.
[140] H. Li, J. Wang, T. Tjardts, et al., Small 20 (2024) 2310660.
[141] S. Lun, H. Wang, K. Wang, et al., ChemCatChem 17 (2025) e202402019.
[142] R. Kumar, S. Vijayapradeep, V. Sakthivel, et al., ACS Appl. Mater. Interfaces 17 (2025) 10556–10569.
[143] L. Hu, X. Gao, H. Wang, et al., Small 20 (2024) 2312251.
[144] C.X. Zhao, L. Yu, J.N. Liu, et al., Angew. Chem. Int. Ed. 61 (2022) e202208042.
[145] Y. Zhu, D. Zheng, X. Xing, et al., J. Phys. Chem. C 128 (2024) 7007–7025.
[146] X.W. Lv, Z. Wang, Z. Lai, et al., Small 20 (2024) 2306396.
[147] L. Zhao, J. Fei, W. Wei, et al., Small 21 (2025) 2410207.
[148] W. Yao, Z. Zheng, J. Zhou, et al., Polymers 15 (2023) 4047.
[149] P. Zhang, Z. Chen, N. Shang, et al., Mater. Chem. Front. 7 (2023) 3994.
[150] J. Miyake, ACS Mater. Au 5 (2025) 960–964.
[151] M. Wang, N. Xu, J. Fu, et al., J. Mater. Chem. A 7 (2019) 11257–11264.
[152] X.W. Lv, Z. Wang, Z. Lai, et al., Small 20 (2023) 2306396.
[153] S. Qu, B. Liu, X. Fan, et al., ChemistrySelect 5 (2020) 8305–8310.
[154] X. Liu, X. Fan, B. Liu, et al., Adv. Mater. 33 (2021) 2006461.
[155] C. Wang, J. Li, Z. Zhou, et al., EnergyChem 3 (2021) 100055.
[156] M. Yee, K. An, D.T. Nguyen, et al., Mater. Today Energy 24 (2022) 100950.
[157] K. Yan, Y. Fan, F. Hu, et al., Adv. Funct. Mater. 34 (2024) 2307740.
[158] Q. Liu, H. Shi, T. Han, et al., Energy Storage Mater. 67 (2024) 103255.
[159] Y. Wang, Z. Wang, F. Zheng, et al., Adv. Sci. 9 (2022) e2105849.
[160] Y. Lu, L. Li, Q. Zhang, et al., Chem. Sci. 13 (2022) 3416–3423.
[161] Z. Song, J. Ding, B. Liu, et al., Adv. Mater. 32 (2020) e1908127.
[162] Y. Feng, L. Zhou, H. Ma, et al., Energy Environ. Sci. 15 (2022) 1711–1759.
[163] Z.W. Li, Y.L. Liang, J. Wang, et al., Adv. Energy Mater. 14 (2024) 2304463.
[164] J. Pan, N. Wang, H.J. Fan, et al., Small Methods 6 (2022) e2201032.
[165] P. Zhang, R. Li, J. Huang, et al., RSC Adv. 11 (2021) 11943–11951.
[166] M. Wu, G. Zhang, L. Du, et al., Small Methods 5 (2021) e2000868.
[167] M. Bhushan, M. Mani, A.K. Singh, et al., J. Mater. Chem. A 8 (2020) 17089–17097.
[168] J. Wu, W.Y. Wu, S. Wang, et al., Nano Res. 17 (2024) 6058–6079.
[169] X. Zhao, C. Wang, H. Liu, et al., Batteries Supercaps 6 (2023) e202200502.
[170] M. Kurian, V. Vijayakumar, N. Manna, et al., J. Mater. Chem. A 11 (2023) 14776–14787.
[171] X. Hui, P. Zhang, J. Li, et al., Adv. Energy Mater. 12 (2022) 2201397.
[172] Y. Zuo, K. Wang, S. Zhao, et al., Chem. Eng. J. 430 (2022) 132996.
[173] M. Jiao, L. Dai, H.R. Ren, et al., Angew. Chem. Int. Ed. 62 (2023) e202301114.
[174] H. Wang, K. Wang, R. Zhang, et al., Chem. Eng. J. 498 (2024) 155539.
[175] X. Zhong, Z. Zheng, J. Xu, et al., Adv. Mater. 35 (2023) e2209980.
[176] Q. Wang, S. Kaushik, X. Xiao, et al., Chem. Soc. Rev. 52 (2023) 6139–6190.
[177] J. Wu, Y. Wang, D. Deng, et al., J. Mater. Chem. A 10 (2022) 19304–19319.
[178] Y. Ye, Y. Zhang, Y. Chen, et al., Adv. Funct. Mater. 30 (2020) 2003430.
[179] J. Niu, Y. Liu, X. Wang, et al., Small 19 (2023) 2302727.
[180] T. Gu, Y. Jia, L. Zhang, et al., J. Am. Chem. Soc. 147 (2025) 15029–15040.
[181] D. Deng, J. Wu, Q. Feng, et al., Adv. Funct. Mater. 34 (2023) 2308762.
[182] Y. Bai, D. Deng, J. Wang, et al., Adv. Mater. 36 (2024) 202411404.
[183] J. Chen, C. Qiu, L. Zhang, et al., Energy Environ. Sci. 17 (2024) 4746–4757.
[184] Y. Zuo, W. Zhang, M. Wei, Energy Storage Mater. 53 (2022) 136–147.
[185] W. Zheng, Y. Zhao, H. Zhang, et al., ACS Appl. Mater. Interfaces 16 (2024) 8885–8894.
[186] D. Rase, N. Manna, R. Kushwaha, et al., Chem. Sci. 15 (2024) 6949–6957.
[187] T.Y. Lin, F.Y. Yen, Y.C. Ting, et al., Chem. Eng. J. 488 (2024) 151093.
[188] D. Zhong, K. Wang, M. Wei, et al., Chem. Eng. J. 510 (2025) 161596.
[189] G. Singh, M. Kumar, T.S. Thomas, et al., ACS Appl. Energy Mater. 4 (2021) 14689–14699.
[190] M. Xu, R. Cao, B. Hao, et al., Angew. Chem. Int. Ed. 63 (2024) e202407380.
[191] R. Xinang, B. Yang, Q.N. Yu, Chem. Eng. J. 499 (2024) 155855.
[192] M. Lv, C. Luo, J. Li, et al., ACS Mater. Lett. 5 (2023) 744–752.
[193] H. Dou, M. Xu, Z. Zhang, et al., Adv. Mater. 36 (2024) 2401858.
[194] S. Vijayapradeep, R. Gokulapriyan, R. Thangasami, et al., ACS Appl. Mater. Interfaces 17 (2025) 24402–24411.
[195] Y. Zuo, K. Wang, M. Wei, et al., Chem. Eng. J. 452 (2023) 139301.
[196] R.B. Huang, M.Y. Wang, J.F. Xiong, et al., eScience 5 (2024) 100309.
[197] M.F. Labata, G. Li, J. Ocon, et al., J. Power Sources 487 (2021) 229356.
[198] W.F. Wu, X. Yan, Y. Zhan, et al., Chem. Eng. J. 451 (2023) 138608.
[199] T.K. Tang, J. Fu, M. Wu, et al., Small Methods 6 (2022) e2101276.
[200] Y. Zuo, W. Zhang, M. Wei, et al., Energy Stor. Mater. 53 (2022) 136–147.
[201] L. Lyu, X. Hu, S. Lee, et al., J. Am. Chem. Soc. 146 (2024) 4803–4813.
[202] Y. Yuan, H. Chen, L. Peng, et al., Nanotechnology 35 (2024) 135601.
[203] A. Singh, R. Sharma, A. Halder, Nanoscale 16 (2024) 4157–4169.
[204] Y. Zheng, D. Wu, T. Wang, et al., Angew. Chem. Int. Ed. 64 (2024) e202418223.
[205] X. Dong, X. Luo, X. Yang, et al., J. Colloid Interface Sci. 672 (2024) 32–42.
[206] X. Zhou, Y. Zhou, L. Yu, et al., Chem. Soc. Rev. 53 (2024) 5291–5337.
[207] N. Zhang, X. Zhao, G. Liu, et al., eTransportation 20 (2024) 100319.
[208] Q. Wang, T. Carroll, F. Shi, et al., Electrochem. Energy Rev. 7 (2024) 15.
[209] Z. Yang, Q. Zhang, T. Wu, et al., Angew. Chem. Int. Ed. 63 (2024) e202317457.
[210] X. Li, J. Mao, F. Cheng, ACS Appl. Energy Mater. 7 (2024) 7808–7817.
[211] M. Ahuis, S. Doose, D. Vogt, et al., Nat. Energy 4 (2024) 373–385.
[212] W. Lyu, X. Yu, Y. Lv, et al., Adv. Mater. 36 (2024) e2305795.
[213] W. Gu, X. Yang, H. Xiang, et al., Curr. Opin. Electrochem. 46 (2024) 101537.
[214] K. Feng, D. Wang, Y. Yu, Molecules 6 (2023) 2721.
[215] Y. Zhao, C. Yang, Y. Yu, Chin. Chem. Lett. 35 (2024) 108865.
[216] Y. Kim, C. Li, J. Huang, et al., Adv. Mater. 36 (2024) 2407761.
[217] Z. Chen, T. Shen, M. Zhang, et al., Adv. Funct. Mater. 34 (2024) 2314864.
[218] X. Zhou, S. Huang, L. Gao, et al., Angew. Chem. Int. Ed. 63 (2024) e202410434.
[219] M. Smdani, M. Hasan, A. Razzaq, et al., Energies 17 (2024) 4295.
[220] K. Nivetha, K. Kumar, N. Jyothi, et al., J. Mater. Sci. Mater. EL 35 (2024) 277.
[221] Y. He, X. Shan, Y. Li, et al., Energy Storage Mater. 68 (2024) 103281.
[222] Z. Yuan, C. Li, Y. Zhang, et al., Ind. Eng. Chem. Res. 63 (2024) 7519–7529.
[223] N. Utomo, S. Hong, R. Sinha, et al., Sci. Adv. 10 (2024) eado4719.
[224] L. Zhong, J. Li, Z. Chen, et al., Appl. Phys. A 130 (2024) 662.
[225] H. Jiang, Y. Du, L. Zhao, et al., Chem. Eng. J. 487 (2024) 150455.
[226] X. Zhang, X. Cui, Y. Li, et al., Small Methods 8 (2024) 2400356.
[227] S. Gao, M. Ma, Y. Zhang, et al., J. Mater. Chem. A 12 (2024) 9469–9477.
[228] Z. Wei, J. Huang, Z. Liao, et al., Energy Storage Mater. 72 (2024) 103714.
[229] W. Wang, J. Lu, Y. Wu, et al., Adv. Mater. 36 (2024) e2311256.
[230] Y. Fu, Z. Gu, Q. Gan, et al., Mater. Sci. Eng. R Rep. 160 (2024) 100815.
[231] J. Liu, Y. Zhou, G. Xing, et al., Adv. Funct. Mater. 34 (2024) 2312636.
[232] H. Xu, J. Mi, J. Ma, et al., Energy Environ. Sci. 180 (2025) 4231–4240.
[233] N. Soontornnon, K. Kimura, Y. Tominaga, ACS Appl. Polym. Mater. 7 (2025) 5598–5607.
[234] T. Zhang, Y. Wang, X. Wang, Nano Energy 139 (2025) 110915.
[235] Z. Zhao, J. Wang, Z. Lv, et al., Chem. Eng. J. 417 (2021) 128096.
[236] B. Nie, T. Wang, S. Lee, et al., Mater. Today Energy 49 (2025) 101829.
[237] Y. He, S. Yang, C. Liu, et al., Small Methods 9 (2025) 2402220.
[238] T. Wang, Q. Yu, Z. Li, et al., Carbon Energy 7 (2025) e670.
[239] Y. Li, X. Yang, Y. He, et al., Adv. Funct. Mater. 34 (2024) 2307736.
[240] L. Chen, X. Liu, G. Zang, et al., J. Energy Chem. 105 (2025) 814–822.
[241] L. Zou, D. Li, H. Liu, et al., Adv. Funct. Mater. 35 (2025) 2505154.
[242] Z. Li, Y. Wang, Y. Li, et al., J. Mater. Chem. A 13 (2025) 10637–10646.
[243] W. Sha, Q. Han, D. Cheng, et al., J. Energy Storage 118 (2025) 116293.
[244] Y. Ren, S. Chen, M. Odziomek, et al., Angew. Chem. Int. Ed. 64 (2025) e202422169.
[245] I. Rani, S. Arwish, K.H. Khan, et al., J. Appl. Polym. Sci. 142 (2025) e56331.
[246] L. Zhang, J. Luo, X. Bai, et al., Electrochim. Acta 470 (2023) 143336.
[247] M. Lucas, R. Gonçalves, T. Kallio, et al., ACS Appl. Energy Mater. 8 (2025) 3904–3915.
[248] J. Sun, L. Guo, D. Ji, et al., Adv. Sci. 12 (2025) 2414931.
[249] A. Salmankhani, A.M. Lopez, P. Scovazzo, ACS Appl. Mater. Interfaces 17 (2025) 11348–11361.
[250] M. Zhang, U. Pal, F. Makhlooghiazad, et al., ACS Appl. Mater. Interfaces 16 (2024) 56095–56105.
[251] W. Huang, G. Zhao, B. Zhang, et al., Small Methods 9 (2025) 2401998.
[252] R. Puttaswamy, Z. Tian, H. Lee, et al., J. Mater. Chem. A 11 (2023) 14075–14085.
[253] L. Ma, S. Chen, N. Li, et al., Adv. Mater. 32 (2020) e1908121.
[254] W. Qiu, Y. Tian, S. Lin, et al., J. Energy Chem. 85 (2023) 581–591.
[255] S. Bandyopadhyay, B. Nandan, Energy Storage Mater. 78 (2025) 104233.
[256] T. Chen, Z. Shuang, J. Hu, et al., Small 18 (2022) e2201628.
[257] X. He, Y. Xiang, W. Yao, et al., Adv. Funct. Mater. 35 (2025) 2416040.
[258] Z. Chen, X. Li, D. Wang, et al., Energy Environ. Sci. 14 (2021) 3492–3501.
[259] J. Feng, D. Ma, K. Ouyang, et al., Adv. Funct. Mater. 32 (2022) 2207909.
[260] Y. Xiang, N. Yu, J. Li, et al., Angew. Chem. Int. Ed. 64 (2025) e202424288.
[261] X. Liu, L. Sun, F. Zhai, et al., Adv. Energy Mater. 15 (2025) 2405433.
[262] Y. Zhang, Y. Li, K. Chen, et al., Chem. Eng. J. 511 (2025) 162164.
[263] G. Sun, Z. Cui, D. Zhao, et al., Nano Lett. 25 (2025) 10742–10750.
[264] B. Ullah, T. Wang, R. Cai, et al., Small 21 (2025) 2501671.
[265] Y. Han, Y. Liu, Y. Liu, et al., Adv. Compos. Hybrid Mater. 8 (2025) 154.
[266] Y. Tan, M. Xi, Y. Zhang, et al., J. Power Sources 624 (2024) 235554.
[267] L. Li, L. Zhang, W. Guo, et al., J. Mater. Chem. A 10 (2022) 10244–10245.
[268] C. Liu, Y. Tian, Y. An, et al., Chem. Eng. J. 430 (2022) 132748.
[269] X. Xiao, X. Xiao, Y. Zhou, et al., Sci. Adv. 7 (2021) eabl3742.
[270] G. Wang, G. Li, Y. Tang, et al., J. Phys. Chem. Lett. 14 (2023) 3512–3520.
[271] J. Li, J. Ren, C. Li, et al., Nano Res. 15 (2022) 7190–7198.
[272] J. Yuan, Y. Li, P. Xu, et al., Mater. Sci. Technol. 230 (2025) 311–318.
[273] P. Kimilita, Y. Yoshimi, N. Sonoyama, J. Electrochem. Soc. 169 (2022) 080527.
[274] T. Zhang, Y. Li, T. Zhang, et al., Langmuir 41 (2025) 3455–3463.
[275] Z. Li, G. Zhou, L. Ye, et al., Chem. Eng. J. 472 (2023) 144992.
[276] W. Tu, S. Liang, L. Song, et al., Adv. Funct. Mater. 34 (2024) 2316137.
[277] C. Zhang, L. Zhang, G. Yu, Acc. Chem. Res. 18 (2022) 1648–1659.
[278] H. Hong, Y. Wang, Y. Zhang, et al., Adv. Mater. 36 (2024) 2407150.
[279] X. Meng, M. Du, Y. Li, et al., Nano Lett. 24 (2024) 8818–8825.
[280] C. Miao, X. Wang, D. Guan, et al., Angew. Chem. Int. Ed. 63 (2024) e202410208.
[281] X. Li, Z. Li, Z. Guo, et al., ACS Appl. Mater. Interfaces 16 (2024) 36901–36910.
[282] F. Li, Z. Kang, L. Shan, et al., Adv. Funct. Mater. 35 (2025) 2503301.
[283] Q. Meng, T. Yan, Y. Wang, et al., Chem. Eng. J. 497 (2024) 154541.
[284] Yee. Yen, A. Laksono, Y. Liou, et al., Chem. Eng. J. 155 (2024) 105278.
[285] D. Chatterjee, K.G. Naik, B.S. Vishnugopi, et al., Adv. Sci. 11 (2024) 2307455.
[286] Y. Yang, G. Chang, Z. Liu, et al., ACS Mater. Lett. 6 (2024) 3564–3571.
[287] J. Zhang, J. Zheng, X. Chen, et al., J. Mater. Res. Technol. 30 (2024) 7998–8005.
[288] L. Ma, S. Chen, X. Li, et al., Angew. Chem. Int. Ed. 59 (2020) 23836.
[289] B. Zhang, J. Chen, C. Wu, et al., Nat. Commun. 16 (2025) 71.
[290] L. Zhao, Y. Peng, P. Dou, et al., InfoMat 6 (2024) e12597.

[291] M.G. Nam, S.W. Jeong, P.J. Yoo, Adv. Energy Mater. 15 (2025) 2400035.
[292] C. Wang, Z. Song, Q. Zhou, et al., J. Energy Storage 115 (2025) 116044.
[293] X. Liu, Y. Peng, L. Zhou, Chem. Eng. J. 505 (2025) 159327.
[294] Z. Liu, X. Zhang, J. Luo, et al., Chin. Chem. Lett. 35 (2024) 109500.
[295] G. Li, F. Hu, J. Chen, et al., J. Mater. Chem. A 12 (2024) 11535–11543.
[296] M. Zhu, H. Wang, H. Wang, et al., Angew. Chem. Int. Ed. 63 (2024) e202316904.
[297] B. Qiu, K. Liang, W. Huang, et al., Adv. Energy Mater. 13 (2023) 230119.
[298] M. Du, X. Liu, J. Zhang, et al., J. Colloid Interface Sci. 667 (2024) 503–509.
[299] S. Shan, H. Zafar, M. Javed, et al., Coord. Chem. Rev. 501 (2024) 215565.